University of Alberta

SELF-ASSEMBLED NANOSTRUCTURES FOR BIOMOLECULAR ANALYSIS

By

Yong Zeng ©

A thesis submitted to the Faculty of Graduate Studies in partial fulfillment of the requirements for the degree of Doctor of Philosophy

Department of Chemistry

Edmonton, Alberta

Fall 2007

Your file Votre référence
ISBN: 978-0-494-33098-2
Our file Notre référence
ISBN: 978-0-494-33098-2

Abstract

This thesis reports the use of colloidal self-assembly approaches to define nanometer-scale porous structures for applications in biomolecular analysis. First, a facile microfluidic colloidal self-assembly strategy has been developed to create ordered, robust, three dimensional nanofluidic sieves within single-channel microfluidic devices, with which fast separation of DNA and proteins of a wide size range was achieved. Compared to conventional colloidal deposition procedures, this approach features faster manufacturing speed, prevention of drying-caused cracks that jeopardize separation performance, and better compatibility with current microfabrication procedures. Next, this single-channel based approach has been successfully extended to large-scale patterning of crack-free crystalline nanosieves in complex microfluidic networks. Using this technique, we devised a 2D DNA microfractionator which can operate in a continuous separation manner. This type of device offers better separation resolution than an array of nanomachined posts reported in the literature. Finally, we studied the electrophoresis of single long DNA molecules confined in a well-ordered micro-cavity array fabricated by colloidal templating. Such unique confinement led to an unusual size-dependency of DNA mobility, which implies the potential of this novel structure for long DNA separation. The results presented in this thesis have demonstrated that colloidal self assembly is a simple and inexpensive alternative to the conventional nanofabrication techniques for making artificial molecular sieves.

Acknowledgements

When writing this section, I realized it is difficult to fully express my sincere gratitude to all those people for supporting me and sharing friendship with me over the past five years, because their offering is priceless. Without any one of them, my studying in a new environment and culture would not have been such an amazing and unforgettable journey in my life.

Foremost, I would like to say my heartfelt thanks to my supervisor, Dr. Jed Harrison. Without his unreserved support, enthusiastic encourage, and insightful guidance, my graduate studies would not have been such fruitful and enjoyable. Such experiences are the most valuable assets to my future career growth. I also thank him for affording my attendance at various international conferences, which offered me an excellent opportunity to expand the knowledge horizon.

The strong support from all my supervisory committee members, Professors Jillian Buriak, Charles Lucy, Mark McDermott, and Brenda Leskiw, are sincerely appreciated. I also thank Prof. Mary Wirth for her willingness to serve in my final oral defense. I am grateful to Prof. Jillian Buriak and Charles Lucy for their valuable advice on my seeking of postdoctoral positions and writing supporting letters for me. Without the help that I received from the staff in the general office, electronic and machine shop, and nanofab, my doctoral research would not have been completed such smoothly.

I owe a debt of gratitude to all the members of the Harrison group, who make my studying at Alberta easier and interesting. I greatly thank Arlene Figley for her excellent job to streamline many trivial and tedious administrative processes and group

businesses so that we could concentrate on our studies. I should thank Mei He, Eric Flaim, and Zhen Wang for their helpful assistance in microfabrication, Prof. Hyuk Jeong, Dr. Dolores Martinez, and Kowlasar Misir for their patient listening and interesting conversations, Dr. Svetlana Sapelnikova, Dr. Abebaw Jemere, Dr. James Bao, and Josh Wasylycia for their helpful discussions in group meetings and hilarious Power Plant/Ratt jokes, and finally, my Chinese fellow labmates, Jin Wen, Yang Ni, Ming Zhong, Qingye Lu, and Yujuan Hua for their help and friendship. I also wish to acknowledge all other friends I met here. You have all made my life in Edmonton fun and colorful.

No words can fully express my appreciation to my parents for their love and sacrifice. They have done all they can do for me and ask nothing in return. Finally, I would like to say special thanks to my beloved wife, Mei, for her understanding, support, trust, and love.

List of Contents

List of Tables

List of Figures

List of Abbreviations

BRF	Biased Reptation model with Fluctuations
BSA	Bovine Serum Albumin
CCD	Charge-Coupled Device
CE	Capillary Electrophoresis
CSA	Colloidal Self Assembly
DNA	Deoxyribonucleic Acid
EOF	Electro-osmotic Flow
HPLC	High Performance Liquid Chromatography
IEF	Isoelectric Focusing
kbp	kilo-base pair
kDa	kilodalton
PA	Polyacrylamide
PCR	Polymerase Chain Reaction
PDMS	Poly(dimethylsiloxane)
PFGE	Pulsed-Field Gel Electrophoresis
PS	Polystyrene
PVP	Poly(vinylpyrrolidone)
RNA	Ribonucleic Acid
SDS	Sodium Dodecyl Sulphate
SEC	Size Exclusion Chromatography
SEEC	Size Exclusion Electrochromatography
SEM	Scan Electron Microscopy
TBE	Tris-Borate-EDTA
μTAS	Miniaturized Total Chemical Analysis System

Chapter 1

Introduction

1.1 BACKGROUND AND MOTIVATION

1.1.1 Micro- and Nanofluidics for Bioanalysis

Miniaturized total chemical analysis system (μTAS), also called "Lab-on-chip" technology, has undergone explosive growth since the concept was introduced in the early 1990s [1, 2]. Similar to the success of semiconductor microelectronics, the realization of μTAS is envisioned as a revolution in the advance of Science and Technology and our daily life. μTAS devices involve manipulating and processing small amount of fluids (10^{-9} to 10^{-18} litres), carried out within small spatial confinements, such as channels and droplets, with dimensions of several to hundreds of micrometres. Thus, microfluidic technologies, as well as their extension to the nanometer scale (nanofluidics), are a keystone idea for the miniaturization of analytical systems. Advances in micro- and nanofabrication techniques and the designs of functional components have allowed profound progress in understanding the fundamental behavior of confined fluids and fluid manipulation [3], as well as in applying microfluidic systems to the resolution of practical problems [4]. Their applications span numerous fields in physical and biological sciences and engineering, including genomics and proteomics [5, 6], high-throughput screening in drug discovery [7], cell biology [8], biomedical diagnostics and public health [9], chemical reactions and synthesis [10, 11], single-

molecule level studies [12], and optics [13]. Microfluidic systems have also seen growth in commercial applications over the last decade [14].

Separation sciences and technologies provide indispensable tools for modern scientific research and industrial practices. Separation-based analytical microsystems have occupied a dominant position in the development of microfluidics [15, 16]. One excellent example is the explosive development of highly integrated and automated microfluidic systems for DNA [17-20] and protein analysis [21-24] and their applications in genomics and proteomics, forensic and biomedical diagnostics [17, 21, 25-29].

Figure 1-1 demonstrates several separation-based integrated bioanalytical microsystems that have been realized recently. Burns *et al.* developed a miniaturized system integrated with microfuidic channels, heaters, temperature sensors, and fluorescence detectors, as shown in Figure 1-1A, which is capable of performing all steps of on-chip analysis DNA samples at nanolitre level, including measuring aqueous solutions, solution mixing, DNA amplifying or digesting, and DNA sample separation and detection [30]. More recently, the Mathies group has invented several separation-based microsystems for DNA analysis, including a microfabricated bioprocessor composed of 96 capillaries for high throughput DNA sequencing (Figure 1-1B) [31] and a fully integrated microdevice capable of performing the complete cycle of Sanger DNA sequencing (PCR, sample purification by affinity-capture, and capillary electrophoresis separation) from only 1 fmol of DNA template (Figure 1-1C) [32]. Herr *et al.* devised a microfluidic immunoassay device using multistep-photopatterned polyacrylamide hydrogels, which enables hands-free immunoassay analysis of human saliva samples by integrating sample pretreatment (filtering, concentration, mixing) with protein separation

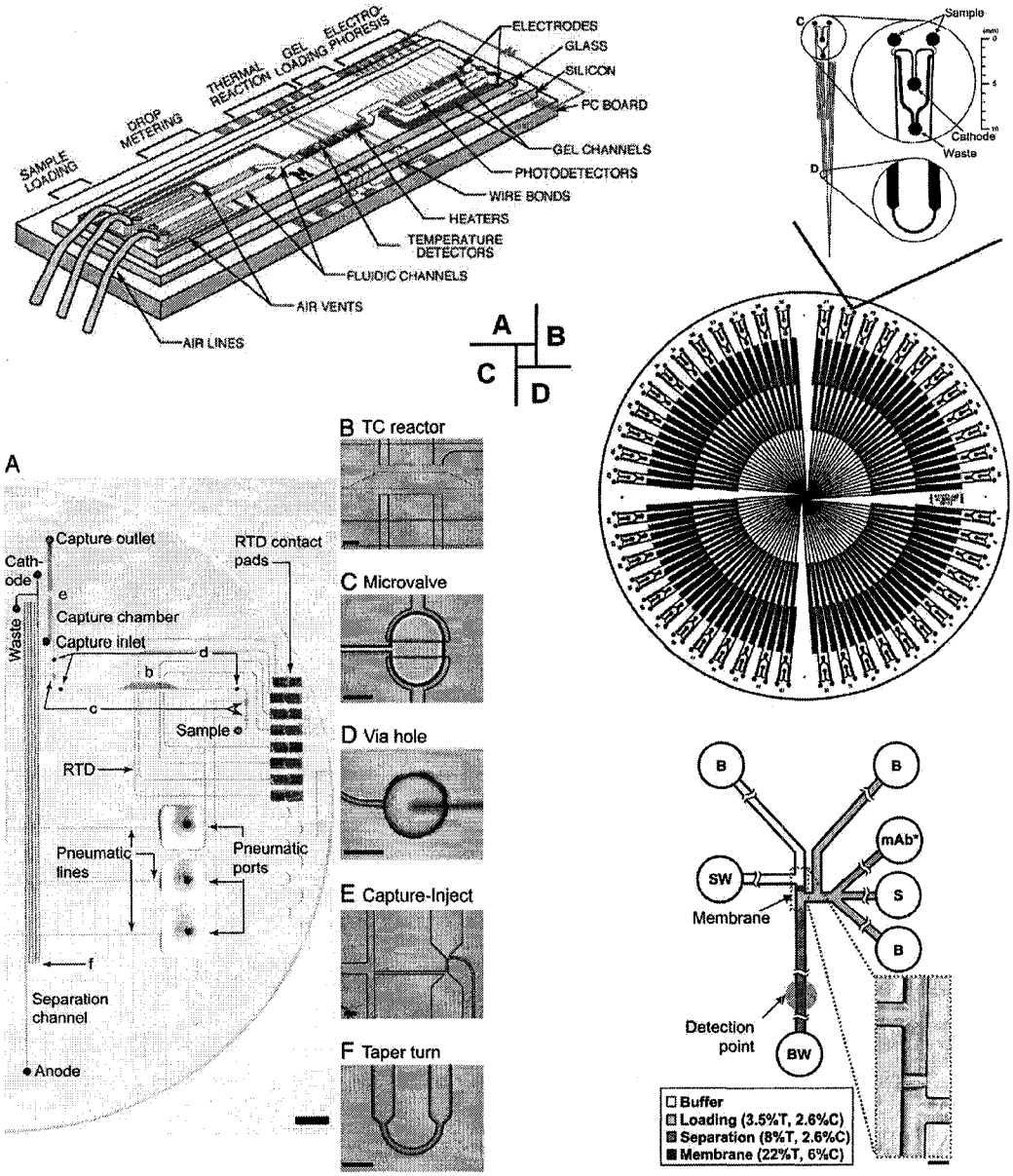

Figure 1-1. Integrated separation-based bioanalytical microsystems. (A) A device for nanoliter-scale DNA analysis [30][1]. (B) A microfabricated 96-lane capillary array electrophoresis bioprocessor for highly parallel DNA sequencing [31][2]. (C) An integrated microdevice with multiple components designed for performing complete Sanger DNA sequencing [32][2]. (D) A microfluidic immunoassay system based on multistep photopatterned polyacrylamide hydrogel for saliva sample processing and protein electrophoretic separation [29][2].

1. Copyright by the American Association for the Advancement of Science
2. Copyright by the National Academy of Sciences of the United States of America

by gel electrophoresis (Figure 1-1D) [29]. This microchip-based clinical point-of-care (POC) diagnostic demonstrated the ability of rapid and reliable detection of proteinaceous disease biomarkers in biofluids. The above-mentioned examples clearly illuminate the advantages of system miniaturization: enhanced separation speed and efficiency, high throughput analysis, reduced costs of instruments and chemicals, and functional integration and multiplexing.

Not only does micro- and nanotechnology bring the benefits of miniaturization, but it also opens new opportunities for the development of separation science, offering us unprecedented tools to clearly understand and improve established methods, and to discover new materials and mechanisms [16, 33, 34]. In the last decade, the advance of micro- and nanofabrication techniques has made it possible to design and fabricate structures approaching molecular size scales [12, 35-37]. Such capability enables us to control and modify the interactions between single biomolecules and nanofabricated structures, allowing an understanding their hydrodynamic properties [38-45] and biological functions [46-49]. A variety of micro-/nanomachined structures have been explored in the applications of the separation and manipulation of particles [50], microtubule [51], biomolecules [42, 50, 52-58], and blood cells [59].

Compared with conventional gels and polymer matrixes widely used for bioseparations (even in microchip format as exemplified in Figure 1-1), artificial gel structures possess advantages such as regular and precisely engineered geometry, mechanical robustness, and easy integration. More attractively, the well-characterized topologies of micro-/nanofabricated structures make deliberate modifications of molecular transport possible, catalyzing the studies of the molecular dynamics underlying

size-based bioseparations [39, 60-62] as well as the exploration of new separation mechanisms [50, 53-56]. Han *et al.* invented a microfabricated DNA separation device composed of an array of trenches interconnected by nano-gaps [39, 55], as sketched in Figure 1-2A. DNA chains can coil randomly in the relatively deep trenches, but have to deform themselves to enter and travel through nano-gaps smaller than their random coil dimensions at the cost of molecular conformational entropy. Thus, the deep trenches serve as entropic traps to retain DNA coils, and the rate of escape from the traps depends on the DNA size. Fu and Han also achieved rapid separation of short DNA and SDS-denatured proteins using the same geometric design, but based on a completely different mechanism, Ogston sieving [60, 63]. The Austin group investigated Brownian ratcheting-based DNA separation using an asymmetric two-dimensional array of obstacles (Figure 1-2B) [53]. The array rectifies the lateral Brownian motion of the DNA molecules moving in the vertical direction under an electric field, and thereby deflects them based on their size-dependent diffusion coefficients. Recently, the same group discovered two approaches to size-based separation using micropillar arrays fabricated on silicon chips. In the so-called "DNA prism" device (Figure 1-2C, top), asymmetric pulsed electric fields are applied to stretch long DNA coils around the micropillars and sort them into flow streams of different angles by the molecular length [56], as schematically represented in the bottom portion of Figure 1-2C. The other method, as seen in Figure 1-2D, utilizes the differential distribution of variously-sized particles in the branching laminar flow around the micropillars [50, 59]. Each row of pillars is shifted laterally with respect to the previous one, such that, when traveling vertically down the array, larger particles experience certain lateral displacement while smaller ones tend to

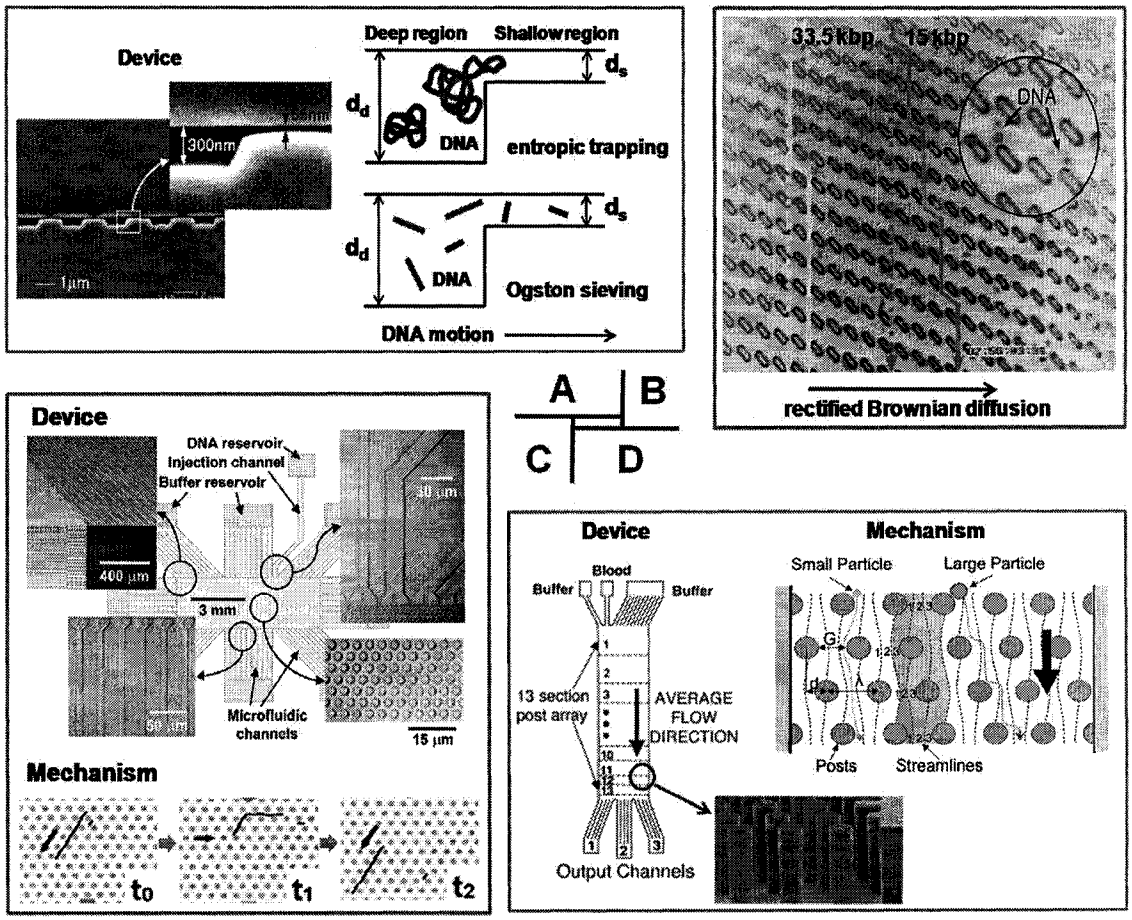

Figure 1-2. Micro- and nanofabricated structures for on-chip bioseparations in size. (A) A nanofilter microdevice for separating both DNA and protein molecules based on distinct mechanisms: entropic trapping for long DNA and Ogston sieving for short, rigid DNA fragments and SDS-denatured proteins (modified from Ref. 60)[3]. (B) A Brownian-ratchet device composed of an asymmetric two-dimensional array of microfabricated obstacles for continuous separation of large DNA molecules based on their diffusivities [53][4]. (C) A "DNA prism" device using asymmetric pulsed electric fields to stretch long DNA around the microposts and thereby sort them into streams of different angles based on their length (reprinted from Ref. 56 with permission). (D) An array of microposts for the separation by deterministic displacement of particles following the branching streams around the microposts [59][4].

---

3. Copyright by the copyright by the American Physical Society
4. Copyright by the National Academy of Sciences of the United States of America

remain in the streamlines. Such structure has been scaled up for the fractionation of blood components [59].

1.1.2 Nanofabrications: Lithography and Self-Assembly

Nanofluidics relies on the rapid advance of nanofabrication techniques [36]. Conventional photolithography microfabrication techniques using ultraviolet light and photomask are diffraction limited, improved to higher resolution by using extreme ultraviolet light (EUV) or X-rays [64]. Using EUV light imposes difficulties such as mask damage due to the high energy of the beam and the incompatibility with conventional optics. Lithography technologies based on focused beams, such as electron beam lithography (EBL) [65] and focused ion beam (FIB) lithography [66], are more widely used, offering the capability to work on a 10-nm scale. These techniques are operated in the scanning mode, however, which is extremely slow and expensive for writing large areas of nanoscale features. Interferometric lithography (IL) provides a means of patterning wafer-scale uniform nanoscale features like lines and pillars using the interference of two and more coherent beams [67].

Conventional nanolithography techniques, however, suffer from some common disadvantages, such as requiring sophisticated facilities and time-consuming procedures, and normally producing 2D architectures. These characteristics impede their application to fluidic systems on a routine base. So far, most micro-/nanomachined structures were designed for large DNA molecules, due in part to technical challenges in lithographically accessing structures on the dimensions of smaller molecules, such as proteins (<~10 nm).

Self assembly or self-organization provides promising alternatives to the

lithographic techniques. Starting from nanoscale building blocks, e.g. atoms and macromolecules, self assembly enables spontaneous formation of complex, three-dimensional ensembles with nanoscale features that are beyond the ability of current nanolithography techniques. Self-organized structures can find many applications. For instance, the microscopic phase separation of the two blocks in a diblock copolymer can lead to a self-assembled pattern of ordered domains, with dimensions below photolithographic resolution limits over wafer scale areas. One of the polymer components can be selectively etched away, and the pattern left behind can be used as the mask for lithographic processing [68]. Spontaneous formation of a regular pattern of nanometer-sized pores in anodic alumina during electrochemical etching has been reported for constructing microfluidic chips for size exclusion-based separation of DNA [69]. Self-assembly of a liquid crystalline lipid bilayer has been employed to create complex two- and three-dimensional nanotube networks suitable to transport and interrogate single molecules [70, 71]. Striemer *et al.* discovered the spontaneous formation of nanopores by nanocrystal nucleation during rapid annealing of an amorphous silicon film, which allows them to fabricate nanoporous membranes with a thickness approaching the sizes of molecules to be separated [72]. Such ultrathin membranes, which are extremely challenging and expensive for conventional nanopatterning techniques to make, are able to filter molecules by size or charge, at rates an order of magnitude faster than other existing membrane materials.

Spontaneous organization of particles of uniform size, referred to as colloidal self assembly (CSA), has been extensively used in a variety of areas, such as the design of nanomaterials [73-76], photonics [77-80], colloidal lithography [81], and chemical and

biological sensors [82, 83]. Recently, self-assembled colloidal structures have attracted increasing interest in molecular manipulation and separation because of their inexpensive fabrication and unique, three-dimensional, well ordered nanostructures. A non-close-packed crystalline lattice, assembled by repelling electrostatic interactions, has been used as a template to fabricate an array of voids in a hydrogel [84]. The regularity of such void arrays made it possible to experimentally verify the entropic trapping effect, which is an important molecular sieving mechanism. Doyle *et al.* used micropost arrays self assembled from superparamagnetic colloids under a uniform magnetic field for microfluidic separation of long DNA molecules [85].

In colloidal deposition by solvent evaporation, monodispersed colloids will be organized into close-packed crystalline arrays, driven by the capillary force between the particles during solvent evaporation [86]. Such a structure features much higher mechanical strength compared to the non-close-packed systems mentioned above. Two groups have used self-assembled silica crystalline arrays for probing electrophoretic behavior of DNA [87, 88]. However, no separation of biomolecules has been reported using this type of nanoporous matrix, presumably due to the technical difficulty of avoiding crack formation during the colloidal assembly process. Although the Wirth group reported using a strip of silica colloidal film for electrochromatographic separation of fluorescent dyes and peptides [89], their deposition method requires careful pretreatment of colloids prior to the deposition process to largely reduce the cracks formed, as well as very long period for colloidal growth. Therefore, it is highly desirable to establish approaches that satisfy the criteria required for the preparation of colloidal matrices for on-chip biomolecular separation: (a) compatibility with microfabrication and

microfluidic operation; (b) simplicity, reasonably fast manufacturing speed, and low consumption of colloidal solution; and most importantly, (c) prevention of macroscopic cracks that will destroy the separation.

1.1.3 Thesis Motivation and Outline

In the work described in this thesis, we are interested in the exploration of new methodologies for self-assembly-based nanofabrication within microfluidic environments and their application to nanofluidic-based biomolecule analysis. Specifically, we seek to employ colloidal self-assembly approaches, as an inexpensive and effective alternative to conventional bottom-up nanofabrication techniques, to obtain molecular-size nanopore structures. The incorporation of such structures into microfluidic systems has been investigated for the purpose of manipulation and size separation of biomolecules, including both nucleic acids and proteins. This is an essential stage in developing a practical bioanalytical microsystem integrated with multifunctional elements, such as sample pretreatment, separation, identification, and analyte collection and concentration. These self-organized materials might also offer a desirable matrix for experimental and theoretical studies of fundamental mechanisms underlying the transport and separation of biomacromolecules.

This thesis is organized as described below:

Chapter 2 discusses a microfluidic colloidal self-assembly approach for facile fabrication of crack-free three dimensional nanoarrays of closed-packed beads within a single-channel microfluidic separation system. The characterization of the nanoporous structure and EOF within the self-assembled colloidal arrays is also discussed. Fast and

reproducible size separation of DNA of 100–2000 bp was achieved to demonstrate the feasibility of using this type of nanostructure as the biomolecular sieving matrix.

In Chapter 3 we are focused on the separation performance of a wide scope of biomolecules, ranging from protein molecules of 20–200 kDa to dsDNA fragments of 0.05–50 kbp, using colloidal nanosieves assembled from monodisperse particles of different sizes and materials. The underlying separation mechanisms are discussed, involving Ogston sieving, reptation, and long DNA hooking. The results presented here demonstrate the flexibility of this self-assembly methodology of nanofabrication in terms of the ability to precisely vary pore sizes to adjust the separation performance for a given type of biomolecule.

Constant-field electrophoretic separation of large DNA molecules shows limited resolution in colloidal nanoarrays because of unfavourable stretching of long DNA chains confined inside relatively smaller pores. Chapter 4 reports employing such confinement-induced stretching in colloidal nanoarrays for high-resolution continuous separation of long DNA, based on asymmetric pulsed-field electrophoresis. A facile microfluidic, large-scale, self-patterning strategy has been established to create large-area, crack-free colloidal nanoarrays within complex microfluidic devices. We studied the deflection behaviour and separation performance of DNA molecules in response to molecular size, pulsing conditions and lattice dimensions. This effort yielded guidelines to achieve the optimum separation for given targets.

Chapter 5 investigates the possibility of using a novel macroporous structure as entropic traps for long DNA separation under constant-field electrophoresis. A colloidal templating approach was used to replicate the inverse structure of a self-assembled

colloidal lattice, forming a regularly organized array of interconnected micrometer-size cavities within dense hydrogels. Electrophoresis of single DNA molecules confined in such micro-cavity arrays exhibits an unusual size-dependency of mobility, which indicates the potential application of this novel material for size separation of long DNA.

Chapter 6 concludes the present progress of this work and discusses some future perspectives.

Before we move on, a brief review on the knowledge of important size separation principles would be helpful to facilitate our discussions. For this purpose, Section 1.2 will mainly introduce some fundamental aspects of size exclusion chromatography and gel electrophoresis, two size separation techniques closely relevant to this thesis work.

1.2 SIZE-BASED BIOSEPARATIONS

1.2.1 Introduction

Because of the complex nature of biological fluids and materials, preparative and analytical separations have played a key role in the development and growth of the modern biology and biotechnology industries. Bioseparation offers the ability to extensively purify the samples of interest before they can be used for their respective applications, as well as to extract biological information out of biomolecules, as with DNA sequencing. A number of bioseparation techniques have been established to target diverse biological samples, such as filtration, capillary electrophoresis (CE), and high performance liquid chromatography (HPLC). Those separation techniques are based on the different chemical or physical properties of biomolecules, including size, molecular weight, density, osmotic pressure, electrical charge, hydrophobic interaction, specific

receptor-ligand binding. Because of the inherent complexity of biological samples, it is very often the case that satisfactory separation cannot be achieved by one technique alone. Therefore, multi-dimensional separations using different techniques (often based on different properties of the analytes) are frequently applied in the purification and separation of biological samples. For instance, two-dimensional gel electrophoresis, widely used in molecular biology and proteomics, separates a complex sample of proteins first by their isoelectric points using isoelectric focusing (IEF), then further resolves proteins with close pI values in an orthogonal size separation using sodium dodecyl sulfate-polyacrylamide gel electrophoresis (SDS-PAGE, the second dimension).

Among the many properties of biomolecules, size plays an important role in a separation process, especially for relatively large molecules of biological importance, such as proteins and nucleic acids. For these macromolecules, the molecular size cannot be expressed in terms of a uniform dimensional parameter such as diameter, as protein molecules possess complex structures in their natural states and nucleic acids are flexible molecules. The Stokes-Einstein relation is a common way to characterize the size of non-spherical particles, which correlates the molecular dimension with their diffusion coefficients. For instance, an irregular-shaped protein molecule is considered to have the diameter of a globular protein with the same diffusivity. Thus, this Stokes-Einstein diameter is a hydrodynamic parameter, which can be experimentally estimated. But the Stokes-Einstein diameter is unsuitable in the case of flexible linear polymer chains such as DNA, RNA, and denatured proteins, whose sizes are usually expressed in terms of the molecular length instead. For many biomacromolecules, the molecular size is related to molecular weight because they are composed of repetitive units. Therefore, size

separation often provides a measure of molecular weight.

Common techniques of size separation include filtration, membrane separations, centrifugation, hydrodynamic chromatography, size exclusion chromatography (SEC), and gel electrophoresis. These approaches use various driving forces and are based on completely different mechanisms, as we will see in the following sections discussing size exclusion chromatography and gel electrophoresis in more details.

1.2.2 Size Exclusion Chromatography

1.2.2.1 Principle and Applications

Size exclusion chromatography (SEC), also known as gel permeation chromatography (GPC) and gel filtration chromatography (GFC), is a column based technique that uses inert porous particles as a stationary phase to separate molecules solely according to their sizes. The separation process and mechanism of SEC is schematically shown in Figure 1-3. A plug of sample containing molecules of different sizes is injected into a column packed with porous beads having an appropriate range of pore sizes, and is propelled by the mobile phase through the full length of the column (Figure 1-3A). The molecules elute in a sequence reverse to their sizes; larger molecules elute earlier than the smaller ones [90]. The mechanism is illustrated in Figure 1-3B. Molecules smaller than the pores penetrate into the beads, while those larger than the pores only occupy the interstitial space between beads, thus moving more rapidly down the column because they do not spend time inside the beads. As a result, components can be separated into distinct bands, which will be detected and transduced into a chromatogram (the bottom of Figure 1-3A) by a detector placed at the end of the column.

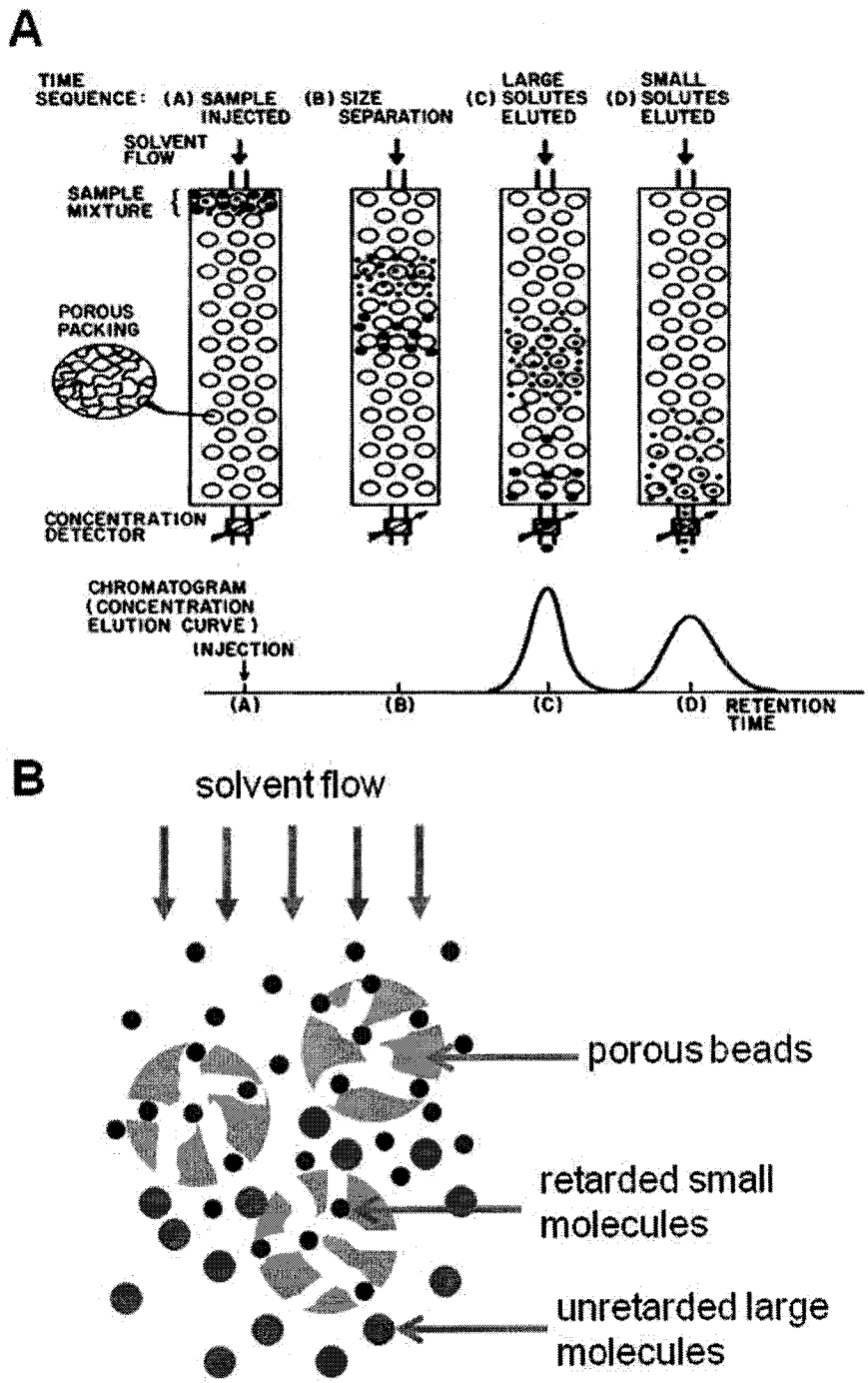

Figure 1-3. Schematic of the mechanism of size exclusion chromatography (SEC). (A) SEC is a chromatographic separation technique using columns packed with porous beads (adapted from Ref. 90). Larger molecules elute faster with the solvent than smaller ones because smaller molecules are more retarded by the pores in the beads as drawn in (B).

The earliest packing materials used for SEC were soft gels, which only work with aqueous mobile phase for the analysis of natural water-soluble polymers under low pressure conditions [91]. Nowadays, semi-rigid polymeric materials such as macroporous cross-linked polystyrene/divinylbenzene (PS/DVB) particles and rigid, chemically derivatized silica particles are widely utilized for both organic and aqueous SEC. The use of materials of high mechanical strength allows size-exclusion separation under high pressure, i.e. high flow rate, which tremendously improves the separation speed and performance. Therefore, the application of SEC technique has been greatly expanded to the separation and the determination of molecular weight distribution of a wide range of polymers and biomacromolecules, including various synthetic homopolymers and copolymers, polysaccharides, proteins, and nucleic acids [92].

In addition to conventional SEC driven by hydrodynamic pressure, a new microscale mode of SEC, which uses electroosmotic flow (EOF) as the driving force [93, 94], has been invented. This technique, called size exclusion electrochromatography (SEEC), offers a faster elution speed, higher separation efficiency, and low consumption of mobile phase and sample, compared to conventional SEC [95]. However, SEEC is not as successful as SEC in the analysis of proteins, mainly because other interactions associated with electrokinetic pumping coexist with the size exclusion effect [96], which still remain poorly understood. The combination of pressure and electrokinetic pumping has been applied for SEC separation of proteins [97].

1.2.2.2 Partition Equilibrium in SEC

All separations demand some form of displacement or transport of solute between

phases. In the processes of chromatography, the transport of solute is considered to be close to its equilibrium. Therefore the equilibrium defines to a good extent the actual distribution of solute components between the stationary and mobile phases in chromatographic separations [98]. Understanding the equilibrium is indispensable to the study of separation behavior and efficiency.

Under dilute solution conditions, the ratio of the concentration of one component in the stationary phase to that in the mobile phase, defined as the equilibrium constant K, is related to the standard Gibbs free energy, enthalpy, and entropy difference between the phases at constant temperature and pressure:

$$\Delta G^\circ = \Delta H^\circ - T\Delta S^\circ = -RT \ln K \tag{1.1}$$

where R and T are the gas constant and absolute temperature, respectively. In SEC, size exclusion is considered as the major effect and other interactions between molecules and porous media are negligible. Thus the phase distribution is governed predominantly by entropy [99] and the distribution coefficient can be expressed as

$$K = e^{\Delta S^\circ / R} \tag{1.2}$$

Statistically, the entropy S is related to the number of distinct microscopic states accessible to a macromolecule (Ω) as

$$S = k_B \ln \Omega \tag{1.3}$$

where k_B is the Boltzmann constant. When a macromolecule or a particle enters a porous structure as shown in Figure 1-1B, it is limited largely in terms of the configurational states it can take (e.g. position, orientation, and molecular conformation) because of the steric constraint imposed by the pore walls. A loss of entropy is correspondent to the loss of configurational freedom, which thermodynamically disfavors the partitioning of the

macromolecule into the pores [100]. Compared to larger species, smaller ones feel less spatial constraints and hence have less loss of entropy when going into the pores from the bulk solvent. Thus they experience less exclusion from the porous structure and have a greater possibility to partition into the pores.

Giddings *et al.* established a general theoretical treatment for the partitioning process in porous media based on the principles of statistical mechanics [98, 100]. The equilibrium partition coefficient K can be generally formulated as a ratio of integrals of all microscopic configurational states (e.g. position, orientation, molecular conformation) for molecules within the pores and within the bulk phase. For the simplest case, spherical rigid species partitioning into a hard cylindrical pore as illustrated in Figure 1-4, the expression of K can be simplified as the volume ratio [98]

$$K = \frac{accessible\ volume}{true\ volume} \tag{1.4}$$

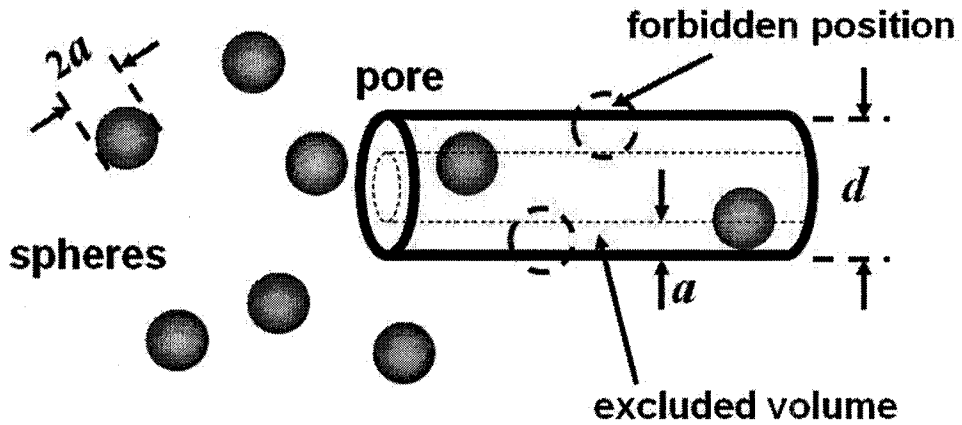

Figure 1-4. Schematic of the partitioning of solid spheres between an ideal cylindrical pore and a bulk liquid. The pore boundary prohibits the overlap with spheres (shown as open circles), resulting in an excluded volume inaccessible to spheres (modified from Ref. 98).

It is clearly seen that the centres of the spheres cannot approach closer than the particle's radius a from the pore surface. The volume accessible to the spheres is actually reduced to a smaller cylindrical pore and the space defined between these two concentric pores becomes the excluded volume (Figure 1-4). The reduction in the effective volume leads to a loss of entropy of spheres in the pore. By geometric calculations, Equation 1.4 can be derived as

$$K = \left(1 - \frac{sa}{2}\right)^2 \tag{1.5}$$

with s defined as the ratio of the surface area to the volume of the capillary pore. Equation 1.5 can be used as an approximation for cases of variously shaped pores, where the diameter is no longer a meaningful parameter of the pore size [100].

This simple case demonstrates the idea of the exclusion effect exerted by the pore walls, which is more complicated for species with shapes other than a sphere, such as

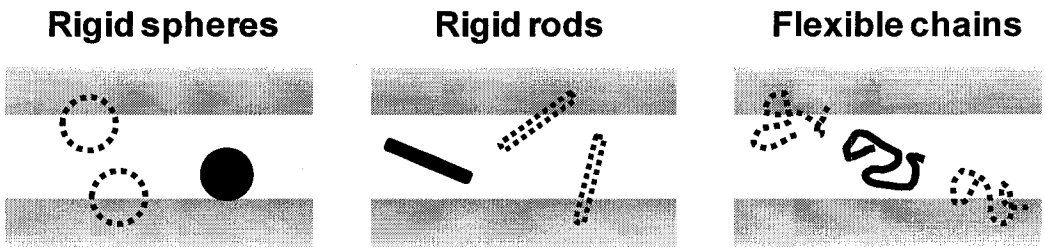

Figure 1-5. Illustration of allowed and forbidden configurations of species of different shapes in ideal slit-shaped pores. Certain molecular configurations (rotations, positions, and conformations) are forbidden because of the steric repulsion from the pore wall to avoid overlapping (modified from Ref. 100).

rods or flexible chains. As shown in Figure 1-5, the exclusion of these species from the pore surface region becomes dependent on orientations and molecular conformations. Giddings *et al.* also derived a surprisingly simple expression applicable for the partitioning of rigid molecules of any complex shape into an isotropic network of random planes [100]

$$K = e^{-s\bar{L}/2} \tag{1.6}$$

where $\bar{L}$ is the mean projection length of the molecule along the various axes. The increase of pore size (hence smaller s) relative to the dimensions of molecules or particles causes K to approach unity (i.e. no exclusion effect). Therefore pore size selection is a primary consideration in choosing stationary materials for efficient separation by SEC.

1.2.3 Gel Electrophoresis

1.2.3.1 Introduction

Many biologically relevant species carry charges in solution. Therefore, electrophoresis has become an important technology in bioanalytical separation, complementary to chromatography techniques. Considering an ionic particle in a solution containing mobile ions, the charges on the particle surface attract counterions, forming an electric double layer around the particle. The thickness of the double layer can be characterized by the Debye screening length, κ^{-1}, given by

$$\kappa^{-1} = \left(\frac{\varepsilon_0 \varepsilon_r k_B T}{N_A e^2 I} \right)^{1/2} \tag{1.7}$$

where ε_0 is the permittivity of free space, ε_r the dielectric constant of the solution, I the ionic strength, k_B the Boltzmann's constant, T the absolute temperature, N_A Avogadro's

number, and e the elementary charge. When an external electric field, E, is applied to the particle, it will move with a mobility μ defined by

$$\mu = \upsilon / E = Q / 6\pi\eta r \tag{1.8}$$

where υ is the electrophoretic velocity, η the viscosity of the solution, Q the total charge, and the Stokes radius of the particle, r, is smaller than the Debye length κ^{-1}. Therefore, charged species can be separated by differential electromigration, which is dependent on their charge and size.

Polyelectrolytes such as DNA and SDS-denatured proteins, however, normally cannot be separated by electrophoresis in free solution. This is due to the free-draining phenomenon, i.e. both charge and hydrodynamic drag along the linear molecule scale linearly with the molecular size (see the discussion in Sec 1.2.3.2). As a result, all molecules migrate at the same speed, regardless of their sizes. Thus, porous media are required for the electrophoretic separation, in which migrating macromolecules interact with the porous structures, resulting in size dependent electrophoretic mobilities. Agarose and polyacrylamide hydrogels are two widely used media that are randomly porous. Agarose gel possesses a wide distribution of pore sizes from ~100 nm to ~1 μm at the commonly used concentrations of 0.5–4% [101, 102], while polyacrylamide (PA) gel has smaller pores typically ranging from several nanometers to ~100 nm [103]. Therefore, agarose gel is mainly used for sizing or separating relatively large molecules of nucleic acids, and PA gel is for protein separation or short DNA sequencing. Gel electrophoresis has become probably one of the most important tools in molecular biology laboratories because of its low cost, simplicity, and ease of operation.

1.2.3.2 Polymer Statics and Dynamics

In this section, we are focused on the basic introduction of the statics and dynamics of a single polymer chain dispersed in a dilute solution. Much more complete and sophisticated theoretical treatments regarding polymer dynamics are available elsewhere [104-106].

The simplest possible model of a flexible polymer chain is the freely jointed chain (FJC) model, which pictures a polymer as N rigid rods (monomers) of equal length b connected freely together, as seen in Figure 1-6A. The end-to-end vector **R** of the chain can be modeled as a sum of random walks of step **r**, so the mean square end-to-end distance $\langle R^2 \rangle$ can be given as [106]

$$\left\langle R^2 \right\rangle = \left\langle \mathrm{R} \cdot \mathrm{R} \right\rangle = \sum_{i=1}^{N} \sum_{j=1}^{N} \left\langle \mathrm{r}_i \cdot \mathrm{r}_j \right\rangle = Nb^2 = Lb \tag{1.9}$$

where $\left\langle \mathrm{r}_i \cdot \mathrm{r}_j \right\rangle = 0$ when $i \neq j$ and $L = Nb$ is the contour length. The ensemble average sign $\langle\ \rangle$ denotes an average over all possible states of a system (such as all different conformations and positions a single chain can possess). The probability distribution function of the end-to-end vector **R** is known to be Gaussian for long chains:

$$p(\mathrm{R}) = \left(\frac{3}{2\pi \left\langle R^2 \right\rangle} \right)^{3/2} \exp\left(-\frac{3R^2}{2\left\langle R^2 \right\rangle} \right) \qquad N >> 1;\ R << Nb. \tag{1.10}$$

Thus the entropy of this chain S can be obtained from Equation 1.3

$$S = k \ln(p(\mathrm{R})) = S(0) - \frac{3k_B R^2}{2Nb^2} \tag{1.11}$$

This implies that with no external forces (no stretching), the equilibrium length of the free chain is zero ($S = S(0)$). This result of course does not describe a real polymer chain,

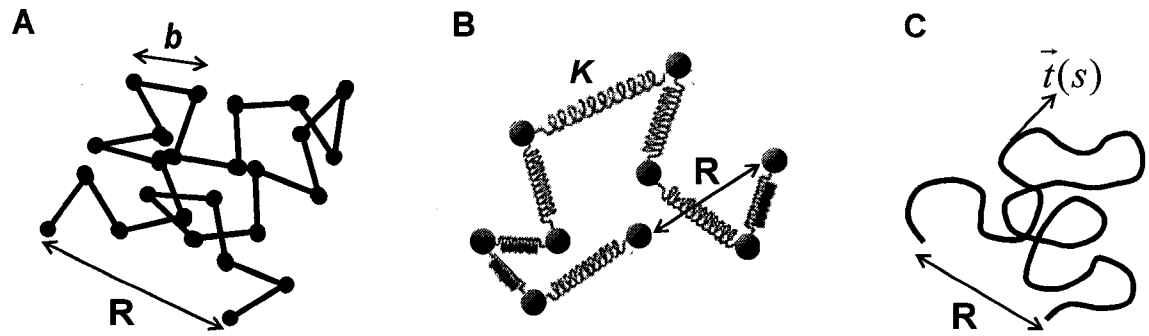

Figure 1-6. Schematics of models of polymer chains (modified from Ref. 107). (A) Freely jointed chain model. (B) Bead-spring model. (C) Worm-like chain model.

because the FJC model represents an ideal chain system which ignores the interactions between monomers and between the chain and surrounding solvent molecules, such as excluded volume and hydrodynamic interactions. From Equation 1.11, the free energy of an ideal chain U can be written as

$$U(\mathrm{R}) = E - TS = U(0) + \frac{3k_B TR^2}{2Nb^2} = U(0) + \frac{1}{2}KR^2 \qquad (1.12)$$

where $U(0)$ indicates the free energy of a chain at the equilibrium state, E is the internal energy independent of chain conformation and T is the absolute temperature. This formula resembles that of a harmonic spring with a spring constant $K = 3k_bT/Nb^2$, which is called an "entropic spring". Thus a freely jointed chain can also be represented as a chain composed of beads connected by entropic springs [107], as sketched in Figure 1-6B. Such a bead-spring chain, also called a Rouse chain, has the same statistical properties as the FJC and is useful for calculation of dynamic properties.

In stiffer polymer chains, such as dsDNA, chemical bonds restrict the motion of monomers, exerting orientation correlation between monomers. The worm-like chain

(WLC) model provides a model suitable for such chains for which the chain flexibility is due to thermal agitation. The WLC model envisions an isotropic rod that is continuously and smoothly curved (Figure 1-6C). For a polymer of contour length L, the end-to-end distance is given by

$$R = \int_0^L \vec{t}(s)ds \tag{1.13}$$

where $\vec{t}(s)$ is the unit vector tangent to the chain at a position s along the chain. The orientation correlation exists for two close points but will decay exponentially along the chain:

$$\left\langle \vec{t}(s)\cdot\vec{t}(0)\right\rangle = e^{-s/P} \tag{1.14}$$

where P is by definition the characteristic persistence length, which represents the stiffness of the chain backbone. The mean square end-to-end distance of the WLC is given by

$$\left\langle R^2\right\rangle = \left\langle R\cdot R\right\rangle = \left\langle \int_0^L \vec{t}(s)ds \cdot \int_0^L \vec{t}(s')ds' \right\rangle$$

$$\left\langle R^2\right\rangle = 2PL\left[1-\frac{P}{L}\left(1-e^{-L/P}\right)\right] \tag{1.15}$$

In the limit of long chain $L >> P$, then

$$\left\langle R^2\right\rangle = 2PL \tag{1.16}$$

Compare (1.16) with (1.9), we see that a WLC can be expressed as a FJC composed of a number N_k of uncorrelated segments (Kuhn segments), $L = N_k l_k$, l_k is the length of the segments, named Kuhn length. It is clear that the Kuhn length is equal to twice the persistence length of a WLC, i.e. $l_k = 2P$.

When floating freely in a good solvent, flexible chains appear as random coils

because of the thermal agitation. The size of an ideal chain in free solution can be characterized by either its mean-square end-to-end distance $\langle R^2 \rangle$ or square radius of gyration $\langle R_g^2 \rangle$ [104]:

$$\langle R_g^2 \rangle = \frac{N_k l_k^2}{6} = \frac{\langle R^2 \rangle}{6} \tag{1.17}$$

Because N_k is directly proportional to the molecular mass, Equation 1.17 indicates the relation between the random-coil size and the molecular mass of an ideal chain. To stress the power law involved in the relation between the radius of gyration and polymer molecular mass, Equation 1.17 can be generalized as a scaling formula using a symbol ~,

$$R_g \sim N^{\upsilon} \tag{1.18}$$

where the exponent $\upsilon = 1/2$ for ideal chains. The models for ideal chains ignore that a position in space cannot be occupied by two monomers at the same time. Such excluded volume interactions, applicable for the chain $L >> l_k$, introduce additional repulsive forces between the monomers and thereby swell the radius of gyration of a real polymer. Flory corrected the scaling equation as

$$R_g \sim N^{3/5} \tag{1.19}$$

where a larger exponent $\upsilon = 3/5$ accounts for the consequence of self-avoiding behavior.

Consider now a uniformly charged DNA chain subjected to an external electric field in a solution. In the common conditions for DNA electrophoresis, the Debye screening length κ^{-1} is much smaller than the DNA Kuhn length and as a result, the long-distance hydrodynamic interactions within the DNA chain are screened by the counterions. When the polymer and surrounding counterions are dragged by electric

forces in opposite directions, the hydrodynamic shearing are localized within the very thin Debye layer around the backbone. Therefore, solvent flow is able to penetrate freely through the molecular coil as it migrates, which is called the "free-draining" phenomenon.

The Rouse model has been developed to describe polymer dynamics under the circumstance of local hydrodynamic interactions, using a bead-spring chain (Figure 1-6B). The beads in a Rouse chain only interact with each other through the connecting springs of mean length b. The friction between each bead with surrounding solvent molecules is characterized by a friction coefficient ζ. The diffusion constant D and the relaxation time τ_R (Rouse time) for a Rouse chain to diffuse a distance on the order of its size can be related by [104]

$$\tau_R = \frac{\zeta N^2 b^2}{3\pi^2 k_B T} \sim \frac{Nb^2}{D} \tag{1.20}$$

$$D = \frac{k_B T}{N\zeta} \tag{1.21}$$

From the Einstein relation $D = k_b T/\zeta_{tot}$, the total friction coefficient ζ_{tot} of a Rouse chain can be written as the sum of the contribution of N beads:

$$\zeta_{tot} = N\zeta \tag{1.22}$$

For a polymer chain electromigrating in free solution at a velocity υ, the total driving force F_{tot} balances with the total frictional force along the chain, so we can define the free-solution mobility μ_0 by

$$\mu_0 = \frac{\upsilon}{E} = \frac{F_{tot}}{\zeta_{tot} E} \tag{1.23}$$

Because F_{tot} and ζ_{tot} are both proportional to N, which represents the molecular size, it is clear that μ_0 is independent on the molecular size. This result explains the well known experimental observation of no separation of DNA in free-solution electrophoresis [108].

1.2.3.3 Fundamental Mechanisms of Gel Electrophoresis

The size-independent electrophoretic mobility of uniformly charged polyelectrolytes (e.g. DNA and SDS-denatured proteins) prevents size separation in free solution. Therefore, size separation by electrophoresis must rely on the introduction of new mechanisms through the use of porous structures, such as gels. Molecular transport in gels is strongly affected by the dimensions of molecules and pores, in light of the general discussion of the size exclusion process (Section 1.2.2.2). The difference here is that we are dealing with deformable molecules instead, which will have significant consequences in terms of size separation. Three general regimes in gel electrophoresis, Ogston sieving, entropic trapping, and reptation (Figure 1-7), will be discussed here.

The Ogston regime

The Ogston regime applies for gel electrophoresis of macromolecules smaller than the pores in a gel. In this region, the macromolecule is assumed to be a rigid globular particle with no conformation changes during electromigration (Figure 1-7A), and thus the separation can be treated as a process of electric field-driven filtration using a gel as the molecular sieve [108-110]. The Ogston model, also known as the free-

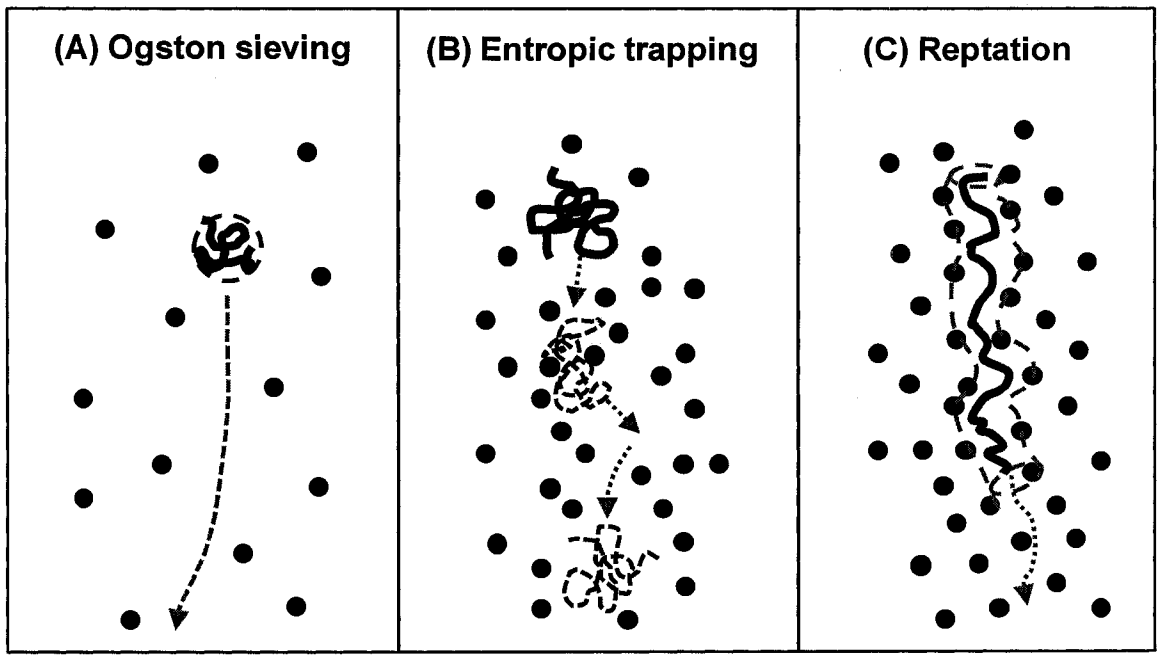

Figure 1-7. Schematics of three regimes of DNA electrophoresis in gels. *Black* dots represent the gel fibres and *Red* dashed arrows indicate the migration trajectories of DNA molecules. (**A**) Ogston sieving. In a sparse gel network, the size of a DNA coil is smaller than the pores defined by the gel fibres so that the molecules remain compact and migrate with collisions with the gel fibres. (**B**) Entropic trapping. The heterogeneously porous gels create relatively open pores surrounded by dense regions. A flexible DNA chain resides in a pore as a random coil and must deform itself to pass through the highly restrictive regions to move into next open pore, losing its configurational entropy. Therefore, the confinement in the dense regions creates an entropic barrier to retain the molecule preferentially in larger pores. (**C**) Reptation (with orientation). In a dense gel of smaller pores, a long DNA molecule has to stretch itself to accommodate in the gel. With the lateral movement impeded by the dense gel fibres, the long chain reptates through the gel mesh in the direction of the electric field, as it is moving inside a virtual tube defined by the gel fibres along its backbone (*Green* dashed tube).

volume model, assumes that the ratio of the electrophoretic mobility μ in a gel of concentration C to the free-solution mobility μ_0 is equal to the fractional gel volume $\phi(C)$ accessible to the molecule. Then the modelling can be performed by calculating $\phi(C)$ based on the geometric models that relate ϕ, C, the effective radius of the globular particle R_g, and the average pore size a. For random gels, Ogston's prediction is given as ($r < a$) [107, 110]

$$\frac{\mu}{\mu_0} = \phi(C) = e^{-K_r C} = e^{-\frac{\pi R_g^2}{4a^2}} \tag{1.24}$$

where $K_r \sim R_g^2$ is the retardation coefficient and the average pore size a is related to the gel concentration C by $a \sim C^{-0.5}$. This equation can be written as

$$\log \mu = \log \mu_0 - K_r C \tag{1.25}$$

which is the Ferguson plot of mobility against gel concentration widely used for molecular weight determination. Since the size of a polymer random coil is directly scaled with its molecular mass (see Equation 1.17), Equation 1.24 can be readily rewritten to show the relation between the mobility and the molecular mass M

$$\log \mu = \log \mu_0 - kM \tag{1.26}$$

where k is a constant. This suggests a common way to identify the Ogston mechanism by examining the semi-log plot of mobility as a function of molecular weight.

The entropic trapping regime

The heterogeneous gel structure creates a wide distribution of pores sizes. When a flexible DNA chain is located in a gel with an average pore size comparable to the size

of a DNA coil, there is a competition for the chain to reside inside a larger pore as a random coil or otherwise deform itself to penetrate into the relatively smaller pores surrounding the larger pores, as depicted in Figure 1-7B. A loss of configurational entropy corresponds to the conformational change of the chain moving from an open space into the highly restrictive regions. Therefore, confinement of the smaller pores creates an entropic barrier to molecular transport under electric fields.

The regime of entropic trapping was originally predicted by computer simulations of polymer diffusion in random environments [111, 112]. Hoagland *et al.* first experimentally verified the "entropic-barrier mediated transport" as an intermediate regime between the Ogston sieving and reptation regimes [113]. Slater *et al.* demonstrated that, in the entropic trapping regime, the mobility exhibits a strong dependence on DNA molecular weight, M [114]

$$\mu \sim 1/M^{1+\gamma} \tag{1.27}$$

where the exponent $\gamma > 0$ provides a measure of the "strength" of the entropic effects. Compared to the other two regimes in DNA gel electrophoresis, however, entropic trapping has been less recognized, probably due to the conditions required to favour its appearance, in particular the requirement of low electric fields. It was found that γ decreases as the electric field increases, and $\gamma = 0$ as DNA reaches the reptation regime [114]. Such conditions have been less interesting in the context of common separation practices.

Random porous gels provide only ill-defined spatial variation, which is also unfavourable for the dominance of entropic trapping. Nanofabricated molecular sieving systems possessing precisely controlled geometries have been developed recently to

greatly facilitate the experimental investigations of the effects of entropic trapping [39, 60, 84, 115]. Han *et al.* designed a nanofluidic array system for the separation of long DNA molecules based on the entropic trapping effects, and they found the separation could be sustained even at fields much higher than those used in gel electrophoresis [55]. Such devices also enabled the explicit experimental observation of the transition from Ogston sieving to the entropic trapping regime in response to the increasing size ratio of DNA to the restricting nanogaps [60].

The reptation regime

The reptation concept was first introduced by de Gennes to describe the diffusion of a long polymer chain within a strongly constrained space, such as a dense gel, where the chain is forced to significantly deform its random-coil conformation [116]. This model envisions a linearized chain that undergoes curvilinear diffusion along the axis of a fictitious tube enveloping the chain, because the lateral movement of the chain is largely impeded by the surrounding obstacles. The application of external electric fields profoundly influences the reptation behaviour, leading to a variety of phenomena that have attracted numerous experimental and theoretical efforts. In gel electrophoresis, the charged polymer, hence the tube, is oriented with the direction of the applied field, and the motion is biased by the field gradient such that one end leads the chain to thread through the gel network, which is called biased reptation (Figure 1-7C).

Among the theoretical treatments developed, the biased reptation model with fluctuations (BRF) yields the best recovery of the experimental results of DNA gel electrophoresis. Taking into account the length fluctuation of a reptation tube during the

electromigration, this model proposed a useful formula of DNA mobility

$$\frac{\mu}{\mu_0} \approx \left[(3N)^{-2} + \left(\frac{2\varepsilon}{5+2\alpha\varepsilon} \right)^2 \right]^{1/2} \tag{1.28}$$

where ε is the dimensionless reduced electric field as defined in [108] and α represents the limiting ratio of μ_0/μ for large DNA chains and very strong fields. This equation predicts good separation for small DNA or low fields, as well as a loss of resolution for long DNA or strong fields. At relatively low field strength, DNA chains are less oriented and stretched and possess rather random conformations, leading to a mobility inversely dependent on size but independent on the field ($\mu \sim \varepsilon^0 N^{-1}$); on the contrary, the extent of orientation and stretching increase with DNA molecular size and field strength, giving a field-dependent behaviour of $\mu \sim \varepsilon^1 N^0$ instead. This is consistent with experimental observations of DC electrophoresis of long DNA molecules in agarose gel [117].

The biased reptation model has also been applied to study the dynamics of pulsed-field separation of long DNA [118-120]. Many features found in pulsed-field experiments, such as the issue of band inversion in field inversion gel electrophoresis, have been successfully explained based on the tube model. A brief summary of this aspect of the reptation model can be found in a comprehensive review contributed by Viovy [108].

To summarize, the theories of partition equilibrium and gel electrophoresis clearly unravel the factors that play critical roles in the size separation processes in porous matrices. Regular colloidal structures reported in this thesis work define unique nanopore confinements. To validate their feasibility for biomolecular separation, it is necessary to understand the possible separation mechanisms involved and to evaluate

their performance as molecular sieves. In the following chapters, we will focus on the effects of the important parameters suggested in the theories introduced above, such as the dimension and geometry of pore confinement, molecular weight, electric field, etc. The knowledge gained through these efforts will help us to optimize size-based separation of biomolecules of interest using this novel class of materials.

1.3 REFERENCES

1 Manz, A.; Graber, N.; Widmer, H. M. *Sensor. Actuat. B-Chem.* **1990**, *1*, 244-248.

2 Dittrich, P. S.; Tachikawa, K.; Manz, A. *Anal. Chem.* **2006**, *78*, 3887-3907.

3 Squires, T. M.; Quake, S. R. *Rev. Mod. Phys.* **2005**, *77*, 977-1026.

4 Whitesides, G. M. *Nature* **2006**, *442*, 368-373.

5 Sanders, G. H. W.; Manz, A. *Trac-Trend Anal. Chem.* **2000**, *19*, 364-378.

6 Oleschuk, R. D.; Harrison, D. J. *Trac-Trend Anal. Chem.* **2000**, *19*, 379-388.

7 Dittrich, P. S.; Manz, A. *Nat. Rev. Drug. Discov.* **2006**, *5*, 210-218.

8 El-Ali, J.; Sorger, P. K.; Jensen, K. F. *Nature* **2006**, *442*, 403-411.

9 Yager, P.; Edwards, T.; Fu, E.; Helton, K.; Nelson, K.; Tam, M. R.; Weigl, B. H. *Nature* **2006**, *442*, 412-418.

10 Song, H.; Chen, D. L.; Ismagilov, R. F. *Angew. Chem. Int. Edit.* **2006**, *45*, 7336-7356.

11 Janasek, D.; Franzke, J.; Manz, A. *Nature* **2006**, *442*, 374-380.

12 Craighead, H. *Nature* **2006**, *442*, 387-393.

13 Psaltis, D.; Quake, S. R.; Yang, C. H. *Nature* **2006**, *442*, 381-386.

14 Haber, C. *Lab Chip* **2006**, *6*, 1118-1121.

15 Harrison, D. J.; Fluri, K.; Seiler, K.; Fan, Z. H.; Effenhauser, C. S.; Manz, A. *Science* **1993**, *261*, 895-897.

16 Khandurina, J.; Guttman, A. *Curr. Opin. Chem. Biol.* **2003**, *7*, 595-602.

17 Lagally, E. T. *et al. Anal. Chem.* **2004**, *76*, 3162-3170.

18 Ashton, R.; Padala, C.; Kane, R. S. *Curr. Opin. Biotech.* **2003**, *14*, 497-504.

19 Lin, Y. W.; Huang, M. F.; Chang, H. T. *Electrophoresis* **2005**, *26*, 320-330.

20 Kan, C. W.; Fredlake, C. P.; Doherty, E. A. S.; Barron, A. E. *Electrophoresis* **2004**, *25*, 3564-3588.

21 Lion, N. *et al. Electrophoresis* **2003**, *24*, 3533-3562.

22 Devoe, D. L.; Lee, C. S. *Electrophoresis* **2006**, *27*, 3559-3568.

23 Sung, W. C.; Makamba, H.; Chen, S. H. *Electrophoresis* **2005**, *26*, 1783-1791.

24 Xu, B.; Du, W.; Liu, B. F.; Luo, Q. M. *Curr. Anal. Chem.* **2006**, *2*, 67-76.

25 Liu, P.; Seo, T. S.; Beyor, N.; Shin, K. J.; Scherer, J. R.; Mathies, R. A. *Anal. Chem.* **2007**, *79*, 1881-1889.

26 Tian, H. J.; Emrich, C. A.; Scherer, J. R.; Mathies, R. A.; Andersen, P. S.; Larsen, L. A.; Christiansen, M. *Electrophoresis* **2005**, *26*, 1834-1842.

27 Horsman, K. M.; Bienvenue, J. M.; Blasier, K. R.; Landers, J. P. *J. Forensic Sci.* **2007**, *52*, 784-799.

28 Easley, C. J. *et al. Proc. Natl. Acad. Sci. U.S.A.* **2006**, *103*, 19272-19277.

29 Herr, A. E.; Hatch, A. V.; Throckmorton, D. J.; Tran, H. M.; Brennan, J. S.; Giannobile, W. V.; Singh, A. K. *Proc. Natl. Acad. Sci. U.S.A.* **2007**, *104*, 5268-5273.

30 Burns, M. A. *et al. Science* **1998**, *282*, 484-487.

31 Paegel, B. M.; Emrich, C. A.; Weyemayer, G. J.; Scherer, J. R.; Mathies, R. A. *Proc. Natl. Acad. Sci. U.S.A.* **2002**, *99*, 574-579.

32 Blazej, R. G.; Kumaresan, P.; Mathies, R. A. *Proc. Natl. Acad. Sci. U.S.A.* **2006**, *103*, 7240-7245.

33 Kutter, J. P.; Fintschenko, Y. *Separation methods in microanalytical systems*; Taylor & Francis: Boca Raton, 2006.

34 Mohamadi, M. R.; Mahmoudian, L.; Kaji, N.; Tokeshi, M.; Chuman, H.; Baba, Y. *Nano Today* **2006**, *1*, 38-45.

35 Tegenfeldt, J. O.; Prinz, C.; Cao, H.; Huang, R. L.; Austin, R. H.; Chou, S. Y.; Cox, E. C.; Sturm, J. C. *Anal. Bioanal. Chem.* **2004**, *378*, 1678-1692.

36 Mijatovic, D.; Eijkel, J. C. T.; van den Berg, A. *Lab Chip* **2005**, *5*, 492-500.

37 Eijkel, J. C. T.; van den Berg, A. *Lab Chip* **2006**, *6*, 19-23.

38 Bakajin, O. B.; Duke, T. A. J.; Chou, C. F.; Chan, S. S.; Austin, R. H.; Cox, E. C. *Phys. Rev. Lett.* **1998**, *80*, 2737-2740.

39 Han, J.; Turner, S. W.; Craighead, H. G. *Phys. Rev. Lett.* **1999**, *83*, 1688-1691.

40 Reisner, W.; Morton, K. J.; Riehn, R.; Wang, Y. M.; Yu, Z. N.; Rosen, M.; Sturm, J. C.; Chou, S. Y.; Frey, E.; Austin, R. H. *Phys. Rev. Lett.* **2005**, *94*, 196101.

41 Tegenfeldt, J. O. *et al. Proc. Natl. Acad. Sci. U.S.A.* **2004**, *101*, 10979-10983.

42 Volkmuth, W. D.; Austin, R. H. *Nature* **1992**, *358*, 600-602.

43 Balducci, A.; Mao, P.; Han, J. Y.; Doyle, P. S. *Macromolecules* **2006**, *39*, 6273-6281.

44 Stein, D.; van der Heyden, F. H. J.; Koopmans, W. J. A.; Dekker, C. *Proc. Natl. Acad. Sci. U.S.A.* **2006**, *103*, 15853-15858.

45 Turner, S. W. P.; Cabodi, M.; Craighead, H. G. *Phys. Rev. Lett.* **2002**, *88*, -.

46 Riehn, R.; Lu, M. C.; Wang, Y. M.; Lim, S. F.; Cox, E. C.; Austin, R. H. *Proc. Natl. Acad. Sci. U.S.A.* **2005**, *102*, 10012-10016.

47 Wang, Y. M. *et al. Proc. Natl. Acad. Sci. U.S.A.* **2005**, *102*, 9796-9801.

48 Jo, K.; Dhingra, D. M.; Odijk, T.; de Pablo, J. J.; Graham, M. D.; Runnheim, R.; Forrest, D.; Schwartz, D. C. *Proc. Natl. Acad. Sci. U.S.A.* **2007**, *104*, 2673-2678.

49 Levene, M. J.; Korlach, J.; Turner, S. W.; Foquet, M.; Craighead, H. G.; Webb, W. W. *Science* **2003**, *299*, 682-686.

50 Huang, L. R.; Cox, E. C.; Austin, R. H.; Sturm, J. C. *Science* **2004**, *304*, 987-990.

51 van den Heuvel, M. G. L.; De Graaff, M. P.; Dekker, C. *Science* **2006**, *312*, 910-914.

52 Baba, M.; Sano, T.; Iguchi, N.; Iida, K.; Sakamoto, T.; Kawaura, H. *Appl. Phys. Lett.* **2003**, *83*, 1468-1470.

53 Chou, C. F.; Bakajin, O.; Turner, S. W. P.; Duke, T. A. J.; Chan, S. S.; Cox, E. C.; Craighead, H. G.; Austin, R. H. *Proc. Natl. Acad. Sci. U.S.A.* **1999**, *96*, 13762-13765.

54 Fu, J. P.; Schoch, R. B.; Stevens, A. L.; Tannenbaum, S. R.; Han, J. Y. *Nat. Nanotechnol.* **2007**, *2*, 121-128.

55 Han, J.; Craighead, H. G. *Science* **2000**, *288*, 1026-1029.

56 Huang, L. R.; Tegenfeldt, J. O.; Kraeft, J. J.; Sturm, J. C.; Austin, R. H.; Cox, E. C. *Nat. Biotechnol.* **2002**, *20*, 1048-1051.

57 Kaji, N.; Tezuka, Y.; Takamura, Y.; Ueda, M.; Nishimoto, T.; Nakanishi, H.; Horiike, Y.; Baba, Y. *Anal. Chem.* **2004**, *76*, 15-22.

58 Bakajin, O.; Duke, T. A. J.; Tegenfeldt, J.; Chou, C. F.; Chan, S. S.; Austin, R. H.; Cox, E. C. *Anal. Chem.* **2001**, *73*, 6053-6056.

59 Davis, J. A.; Inglis, D. W.; Morton, K. J.; Lawrence, D. A.; Huang, L. R.; Chou, S. Y.; Sturm, J. C.; Austin, R. H. *Proc. Natl. Acad. Sci. U.S.A.* **2006**, *103*, 14779-14784.

60 Fu, J. P.; Yoo, J.; Han, J. Y. *Phys. Rev. Lett.* **2006**, *97*, 018103.

61 Randall, G. C.; Doyle, P. S. *Macromolecules* **2006**, *39*, 7734-7745.

62 Huang, L. R.; Silberzan, P.; Tegenfeldt, J. O.; Cox, E. C.; Sturm, J. C.; Austin, R. H.; Craighead, H. *Phys. Rev. Lett.* **2002**, *89*, 178301.

63 Fu, J. P.; Mao, P.; Han, J. Y. *Appl. Phys. Lett.* **2005**, *87*, 263902.

64 Naulleau, P. *et al. J. Vac. Sci. & Tech. B* **2002**, *20*, 2829-2833.

65 Cabodi, M.; Turner, S. W. P.; Craighead, H. G. *Anal. Chem.* **2002**, *74*, 5169-5174.

66 Campbell, L. C.; Wilkinson, M. J.; Manz, A.; Camilleri, P.; Humphreys, C. J. *Lab Chip* **2004**, *4*, 225-229.

67 O'Brien, M. J.; Bisong, P.; Ista, L. K.; Rabinovich, E. M.; Garcia, A. L.; Sibbett, S. S.; Lopez, G. P.; Brueck, S. R. J. *J. Vac. Sci. & Tech. B* **2003**, *21*, 2941-2945.

68 Park, M.; Harrison, C.; Chaikin, P. M.; Register, R. A.; Adamson, D. H. *Science* **1997**, *276*, 1401-1404.

69 Sano, T.; Iguchi, N.; Iida, K.; Sakamoto, T.; Baba, M.; Kawaura, H. *Appl. Phys. Lett.* **2003**, *83*, 4438-4440.

70 Tokarz, M.; Akerman, B.; Olofsson, J.; Joanny, J. F.; Dommersnes, P.; Orwar, O. *Proc. Natl. Acad. Sci. U.S.A.* **2005**, *102*, 9127-9132.

71 Hurtig, J.; Gustafsson, B.; Tokarz, M.; Orwar, O. *Anal. Chem.* **2006**, *78*, 5281-5288.

72 Striemer, C. C.; Gaborski, T. R.; McGrath, J. L.; Fauchet, P. M. *Nature* **2007**, *445*, 749-753.

73 Velev, O. D.; Lenhoff, A. M.; Kaler, E. W. *Science* **2000**, *287*, 2240-2243.

74 Jiang, P.; Bertone, J. F.; Colvin, V. L. *Science* **2001**, *291*, 453-457.

75 Dinsmore, A. D.; Hsu, M. F.; Nikolaides, M. G.; Marquez, M.; Bausch, A. R.; Weitz, D. A. *Science* **2002**, *298*, 1006-1009.

76 Mezzenga, R.; Ruokolainen, J.; Fredrickson, G. H.; Kramer, E. J.; Moses, D.; Heeger, A. J.; Ikkala, O. *Science* **2003**, *299*, 1872-1874.

77 Blanco, A. *et al. Nature* **2000**, *405*, 437-440.

78 Vlasov, Y. A.; Bo, X. Z.; Sturm, J. C.; Norris, D. J. *Nature* **2001**, *414*, 289-293.

79 Arsenault, A. C. *et al. Nat. Mater.* **2006**, *5*, 179-184.

80 Tetreault, N.; Miguez, H.; Ozin, G. A. *Adv. Mater.* **2004**, *16*, 1471-1476.

81 Yang, S. M.; Jang, S. G.; Choi, D. G.; Kim, S.; Yu, H. K. *Small* **2006**, *2*, 458-475.

82 Scott, R. W. J.; Yang, S. M.; Williams, D. E.; Ozin, G. A. *Chem. Comm.* **2003**, 688-689.

83 Ben-Moshe, M.; Alexeev, V. L.; Asher, S. A. *Anal. Chem.* **2006**, *78*, 5149-5157.

84 Liu, L.; Li, P.; Asher, S. A. *Nature* **1999**, *397* 141-144.

85 Doyle, P. S.; Bibette, J.; Bancaud, A.; Viovy, J.-L. *Science* **2002**, *295*, 2237.

86 Denkov, N. D.; Velev, O. D.; Kralchevsky, P. A.; Ivanov, I. B.; Yoshimura, H.; Nagayama, K. *Nature* **1993**, *361*, 26-26.

87 Meistermann, L.; Tinland, B. *Phys. Rev. E* **2000**, *62*, 4014-4017.

88 Zhang, H.; Wirth, M. J. *Anal. Chem.* **2005**, *77*, 1237-1242.

89 Zheng, S. P.; Ross, E.; Legg, M. A.; Wirth, M. J. *J. Am. Chem. Soc.* **2006**, *128*, 9016-9017.

90 Yau, W. W. K., J. J.; Bly, D. D. *Modern size-exclusion liquid chromatography: practice of gel permeation and gel filtration chromatography*; Wiley: New York, 1979.

91 Porath, J.; Flodin, P. *Nature* **1959**, *183*, 1657-1659.

92 Wu, C.-S. *Handbook of size exclusion chromatography and related techniques*, 2nd ed.; Marcel Dekker: New York, 2004.

93 Peters, E. C.; Petro, M.; Svec, F.; Fréchet, J. M. J. *Anal. Chem.* **1998**, *70*, 2296-2302.

94 Venema, E.; Kraak, J. C.; Tijssen, R.; Poppe, H. *Chromatographia* **1998**, *48*, 347-354.

95 Kok, W. T. *J. Chromatogr. A* **2004**, *1044*, 145-151.

96 Tellez, C. M.; Cole, K. D. *Electrophoresis* **2000**, *21*, 1001-1009.

97 Stahl, M.; Jakob, A.; von Brocke, A.; Nicholson, G.; Bayer, R. *Electrophoresis* **2002**, *23*, 2949-2962.

98 Giddings, J. C. *Unified separation science*; Wiley: New York, 1991.

99 Wu, C.-S. *Handbook of size exclusion chromatography and related techniques*, 2nd ed., rev. and expanded. ed.; Marcel Dekker: New York 2004.

100 Giddings, J. C.; Kucera, E.; Russell, C. P.; Myers, M. N. *J. Phys. Chem.* **1968**, *72*, 4397-4408.

101 Maaloum, M.; Pernodet, N.; Tinland, B. *Electrophoresis* **1998**, *19*, 1606-1610.

102 Pernodet, N.; Tinland, B.; Sturm, J.; Weill, G. *Biopolymers* **1999**, *50*, 45-59.

103 Chrambac.A; Rodbard, D. *Science* **1971**, *172*, 440-451.

104 Doi, M.; Edwards, S. F. *The theory of polymer dynamics*; Clarendon Press: Oxford, 1986.

105 Flory, P. J. *Statistical mechanics of chain molecules*; Hanser Publishers: New York, 1989.

106 de Gennes, P.-G. *Scaling concepts in polymer physics*; Cornell University Press: Ithaca, N. Y., 1979.

107 Slater, G. W.; Gratton, Y.; Kenward, M.; McCormick, L.; Tessier, F. *Soft Materials* **2004**, *2*, 155-182.

108 Viovy, J. L. *Rev. Mod. Phys.* **2000**, *72*, 813-872.

109 Rodbard, D.; Chrambac.A *Proc. Natl. Acad. Sci. U.S.A.* **1970**, *65*, 970-977.

110 Ogston, A. G. *Trans. Faraday Soc.* **1958**, *54*, 1754-1757.

111 Baumgartner, A.; Muthukumar, M. *J. Chem. Phys.* **1987**, *87*, 3082-3088.

112 Muthukumar, M.; Baumgartner, A. *Macromolecules* **1989**, *22*, 1937-1941.

113 Smisek, D. L.; Hoagland, D. A. *Science* **1990**, *248*, 1221-1223.

114 Rousseau, J.; Drouin, G.; Slater, G. W. *Phys. Rev. Lett.* **1997**, *79*, 1945-1948.

115 Nykypanchuk, D.; Strey, H. H.; Hoagland, D. A. *Science* **2002**, *297*, 987-990.

116 de Gennes, P. G. *J. Chem. Phys.* **1971**, *55*, 572-579.

117 Slater, G. W.; Kenward, M.; McCormick, L. C.; Gauthier, M. G. *Curr. Opin. Biotech.* **2003**, *14*, 58-64.

118 Viovy, J.-L. *Electrophoresis* **1989**, *10*, 429-441.

119 Slater, G. W.; Noolandi, J. *Electrophoresis* **1989**, *10*, 413-428.

120 Noolandi, J.; Slater, G. W.; Lim, H. A.; Viovy, J. L. *Science* **1989**, *243*, 1456-1458.

Chapter 2

Self-Assembled Colloidal Arrays as Three-Dimensional Nanofluidic Sieves for Separation of Biomolecules on Microchips*

2.1 INTRODUCTION

Size-based separation techniques have been the popular workhorse for sample preparation and analysis in genomics, proteomics, and molecular biology. Compared with conventional slab gel-based electrophoretic techniques, miniaturized systems offer many advantages in terms of higher separation speed, minute consumption of reagents, and integration of multiple functions. Most separation microsystems, however, still rely on gels or polymer solutions for separation of nucleic acids [1] and proteins [2, 3]. Recently, micro-/nanofabricated molecule-sorting structures have received great interest since they provide means to improve the efficiency and speed of biomolecular separation [4]. A variety of micro-/nanomachined sieves have been designed for separating biomolecules [5-14] and particles [14]. Compared with conventional gels and polymer matrixes, artificial gel structures feature regular and precisely engineered geometry, mechanical robustness, and easy integration. The well-characterized topologies of micro-/nanofabricated structures make deliberate modifications of molecular transport possible,

* A version of this chapter has been published. Zeng, Y.; Harrison, D. J. *Anal. Chem.* **2007**, *79*, 2289-2295.

catalyzing the exploration of new mechanisms for size-based fractionation, such as entropic trapping [15], entropic recoil [16], Brownian ratchets [10], and laminar flow bifurcation [14]. However, most micro-/nanomachined structures were designed for large DNA molecules, generally due to technical challenges in lithographically accessing structures on the dimensions of smaller molecules, such as proteins (<~10 nm). Conventional micro-/nanofabrication techniques also suffer from some disadvantages, such as requiring sophisticated facilities and time-consuming procedures, and normally producing 2D architectures, which impedes their applications on a routine base.

Spontaneous organization of monodisperse, micro- and nanometer-sized particles, referred to as colloidal self assembly (CSA), provides a simple and cost-effective alternative to conventional techniques for creating three-dimensional, periodic nanostructures. Applications of CSA include material synthesis [17], photonic bandgap crystals [18], and biological and chemical sensors [19]. Recently, self-assembled colloidal crystals have attracted interest in the fields of separation and polymer dynamics, owing to the relatively simple fabrication and the uniquely ordered porous structure. Reversible colloidal pillar arrays self-organized under a magnetic field have been applied to microfluidic separation of long DNA [20]. Self-assembled colloidal lattices have been employed to probe Brownian diffusion [21] and electrophoretic migration [22, 23] of confined single biopolymer molecules. Recently, Wirth et al. reported high-speed electrochromatographic separation of fluorescent dyes and peptides inside a silica colloidal stripe prepared by the vertical deposition process [24]. However, the use of a colloidal lattice for size separation of biomolecules has not been reported. In addition, there is still a lack of convenient approaches for high-speed fabrication of crack-free

colloidal arrays within microfluidic systems. Conventional techniques, such as gravitational sedimentation [22] and evaporation-based vertical deposition [23, 24], normally demand a period from tens of hours to days to deposit the colloidal array into fluidic devices. They also pose challenges in sealing the deposited colloidal lattices to create enclosed microsystems without disturbing their structures. Vertical deposition suffers from the formation of cracks that prevent good separation performance, mainly due to the inevitable drying stress and the shrinkage of beads [25]. Physical confinements, such as microcapillaries [26, 27] and fluidic cells [28, 29], provide an effective way to pattern colloidal crystals within microstructures, but have not been used to fabricate complete analytical microsystems based on colloidal structures.

In this chapter, we present the first demonstration of gel-free size fractionation of biomolecules within ordered colloidal arrays, which are embedded inside microfluidic channels as a three-dimensional nanofluidic sieving structure. We have established a microfluidic colloidal self-assembly technique that dramatically reduces preparation time and avoids the formation of drying-caused cracks. Using this simple technique, robust colloidal lattices of various pore sizes and materials can be readily incorporated into microfluidic devices for rapid separation of biomolecules with a wide size distribution, such as sodium dodecyl sulfate (SDS)–protein complexes and DNA fragments.

2.2 MATERIALS AND METHODS

2.2.1 Reagents and Samples

All reagents and samples were prepared with deionized water (18.2 MΩ) obtained from an Ultrapure water system (Millipore, Milford, MA). Low DNA mass ladder was

obtained from Invitrogen. Following the manufacturer's instruction, intercalating fluorescent dye YOYO-1 (Molecular Probes, Eugene, OR) was used to stain DNA samples at the dye-to-base pair ratio of ~1:10 in 4× TBE buffer (356 mM Tris-borate, 8 mM EDTA, pH 8.3) containing 4% v/v 2-mercaptoethanol to reduce photobleaching. The final DNA concentration was ~50 ng/μL. YOYO-1 dye is a potential mutagen, and 2-mercaptoethanol is toxic; gloves should be worn when the solutions are handled.

2.2.2 Microchip Fabrication

As drawn in Figure 2-1, poly(dimethylsiloxane) (PDMS) microchips were fabricated using standard soft lithography [30]. A positive photoresist master (AZ-4620, Clariant Corporation, Charlotte, NC) was UV patterned on a 4-in. silicon wafer, and the mold was silanized to facilitate removal of PDMS. Negative PDMS replicas were made by pouring a 10:1 mixture of PDMS base (Sylgard 184, Dow Corning, Midland, MI) with the curing agent over the wafer, followed by curing at 60 °C overnight. PDMS replicas were removed from the master and reservoir holes were punched to access channels. All devices were assembled by sealing PDMS replicas to clean glass slides without oxygen plasma oxidization. PDMS microchips with a cross injector were used, as sketched in Figure 2-2A. Channels were ~100 μm wide and ~20 μm deep. The buffer and injection channels were 4 mm long and the separation channel was 10 mm in length.

2.2.3 Microfluidic Colloidal Self-Assembly

Monodisperse plain polystyrene (PS) microspheres of 770 nm (2.5 % w/v, 3% coefficient of variance) and 1.53 ± 0.039 μm (2.62% w/v) in diameter and silica beads

(A) Prepare positive mold

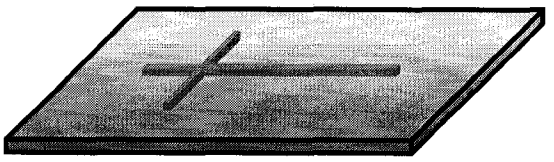

(B) Pour PDMS prepolymer and cure

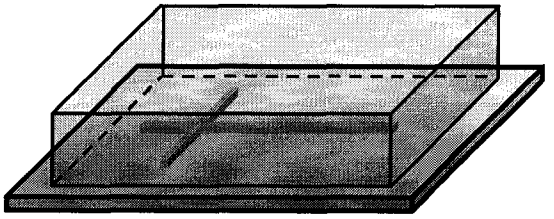

(C) Peel PDMS replica off

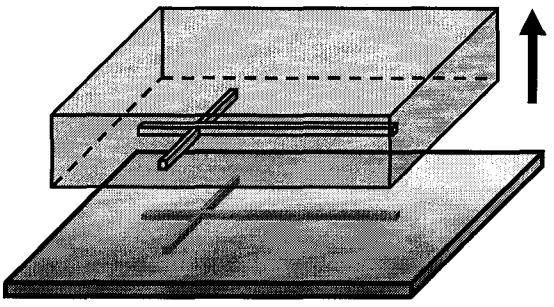

(D) Punch holes and adhere to substrate

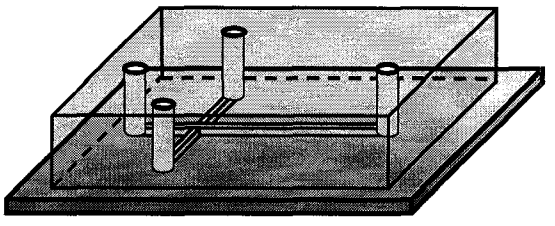

Figure 2-1. Flow chart of PDMS soft lithography processing.

(10% w/v, 0.90 ± 0.04 μm in diameter) were obtained from Polysciences (Warrington, PA). Uniform silica beads of 160 and 330 nm in diameter (10% w/v, <10% deviation) were obtained from Bangs Laboratories. These aqueous suspensions were ultrasonicated for 10 min prior to use.

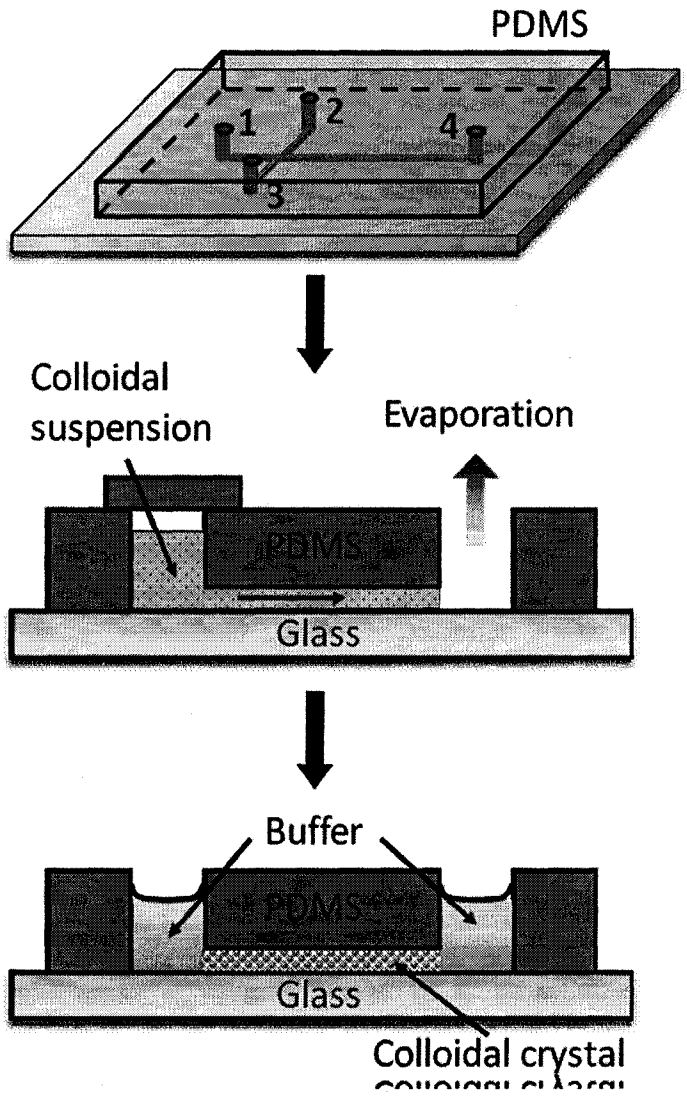

Figure 2-2. Schematic illustration of microfluidic colloidal self-assembly in a one-dimensional separation microchip (PDMS chip layout: 1 buffer, 2 sample, 3 sample waste, 4 buffer waste).

The process of microfluidic colloidal self-assembly is schematically illustrated in Figure 2-2. A 10–15-μL colloidal suspension was injected into reservoirs 1, 2, and 3. The aqueous solution fills the channels spontaneously, forming a liquid meniscus at the outlet of the channel in reservoir 4. Once all channels were filled, reservoirs 1, 2, and 3 were covered with a PDMS piece to prevent solvent evaporation. Reservoir 4 was left open so that evaporation induced colloidal growth within the channels. The growth of the colloidal array can be stopped by replacing the colloidal suspension in the reservoirs with water. Before separations, the water in the reservoirs was substituted with the running buffer and the device was left to equilibrate for ~20 min.

2.2.4 Separation and Fluorescence Detection

4× TBE buffer was used for silica sphere arrays to reduce electroosmotic flow (EOF), with 4% v/v 2-mercaptoethanol added as anti-photobleaching agent. The packed channels were pre-run under ~20 V/cm until the current through the channels became static. Samples were loaded from reservoir 2 by applying a 60–80-V potential to reservoir 3 with other reservoirs grounded to form a "pinched" injection plug. Separation was performed under electric fields between 5 and 60 V/cm with a "pull-back" voltage applied to reservoirs 2 and 3 to prevent sample leakage from the loading arms into the separation channel. It was found that salts in the concentrated buffer are easy to precipitate out due to the permeation of water vapour through the PDMS bulk. This issue can be solved by saturating PDMS replicas in water overnight before assembling with glass substrates.

Separation was monitored using epifluorescence microscopy and digital image collection. Samples were excited with an expanded 488-nm argon ion laser beam, and the emission was collected with a high-sensitivity CCD and a homemade inverted microscope equipped with a 505DRLP dichroic mirror, 515-nm long-pass filter, and a 40× planachromat objective (0.6 N.A., LDN, Carl Zeiss). A 4× objective (0.1 N.A., Olympus) was used for low-magnification imaging of separations. Digitized images were stored in a computer and analyzed using ImageJ (NIH, Bethesda, MD, http://rsb.info.nih.gov/ij/).

2.3 RESULTS AND DISCUSSION

2.3.1 Microfluidic Colloidal Self-Assembly

We performed *in situ* colloidal crystallization within prefabricated microfluidic separation devices, yielding a simple and rapid route to separation bed formation that is compatible with standard microfabrication processes. The channels were spontaneously filled with an aqueous dispersion of colloids by wetting of the hydrophilic glass substrate surface. The flow halted at the edge of the channel outlet in reservoir 4 due to capillary force, forming a convex vapor–liquid interface, as seen in Figure 2-3A. Evaporation triggers the nucleation of microspheres at the interface and creates a one-directional solvent flow to continuously pack the colloidal beads. The microchannel confinement restricts water evaporation to the channel outlet during the assembling process, so that the packed beds remain wet while packing. In Figure 2-3A, the translucence of the compact bed of 0.9-μm silica spheres evidences the presence of interstitial water and no invasion of air into the colloidal array. This can be attributed to strong particle surface wetting,

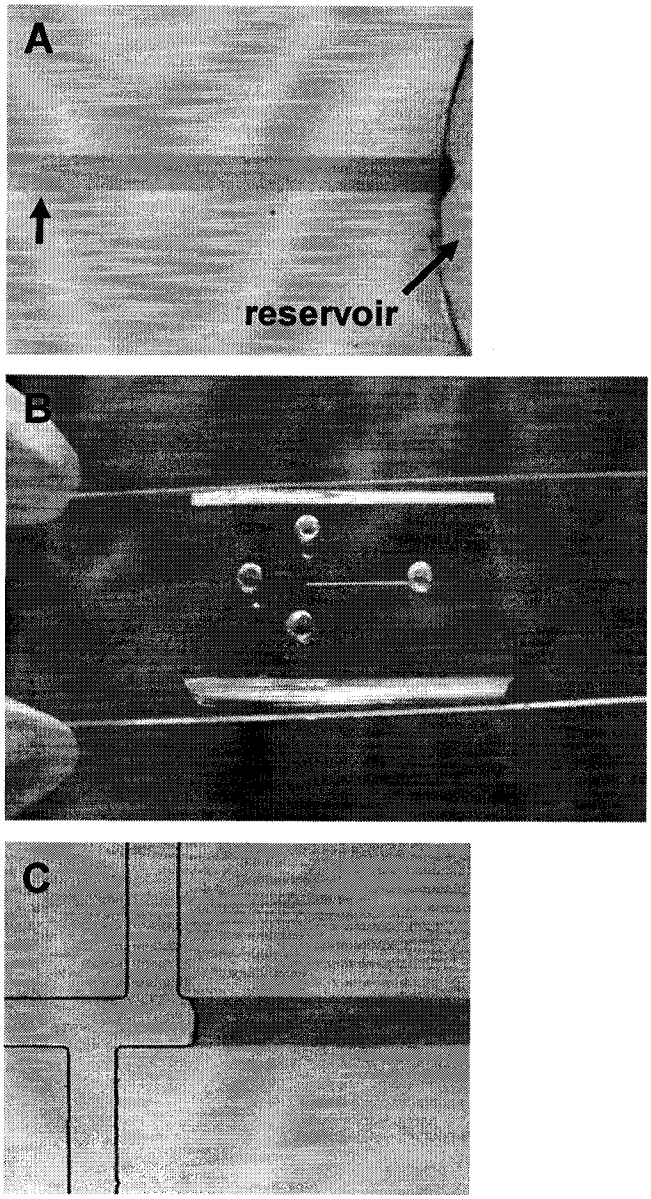

Figure 2-3. Evaporation-induced colloidal self-assembly within microfluidic systems. (A) Optical micrograph of a translucent 0.9-μm silica sphere array growing inside a microchannel (as indicated by the left arrow), showing a convex evaporation interface at the channel opening. (B) Photo of a one-dimensional separation PDMS chip with the separation channel packed with 0.9-μm silica particles. (C) The cross intersection of the partially packed device pictured in (B).

which forms nanomenisci between close-packed spheres at the interface [31]. The capillary tension of the nanomenisci creates the enormous negative capillary pressure, estimated to be as low as −300 psi for 0.9-μm silica spheres, which is required to pull water through the porous packed region. As a result, the evaporating interface is fixed within the vicinity of the channel opening. Therefore, in contrast to the vertical deposition method, this approach prevents drying of the packed bulk during the assembling process, eliminating drying-caused crack formation.

After the packed bed has grown to the desired length, packing can be ceased by replacing all colloidal suspensions in the reservoirs with water. Figure 2-3B is an optical micrograph of a one-dimensional separation PDMS chip with the separation channel packed with 0.9-μm silica particles. Close inspection of the injection region of this partially packed microfluidic chip shows a clear and well-defined bed edge generated by the self-packing process, as seen in Figure 2-3C. The compact portion was uniformly translucent due to the preservation of water in the channel, and no brighter lines, which indicate cracks, are visible.

2.3.2 Characterization of Self-Assembled Colloidal Nanoarrays

Figure 2-4 demonstrates that a bed of 0.9-μm silica beads packed in a straight channel exhibited monochromic transmitted light at various specific angles away from normal. This is due to Bragg diffraction, and it indicates the ordered crystalline structure generated within the microchannel. Figure 2-5A shows a typical SEM image of an array of 330-nm silica particles patterned within a microchannel, which was slowly dried by vapour permeation through the PDMS to minimize the perturbation on the colloidal

structure due to drying. No large cracks were observed over the entire structure, while a very low density of small cracks was still present, due mainly to the SEM sample preparation process. A close-up of this bed, shown in Figure 2-5B, illustrates the close-packed arrangement of the monodisperse colloids and the long-range order over three dimensions. A low density of defects was seen, including point voids, dislocation lines,

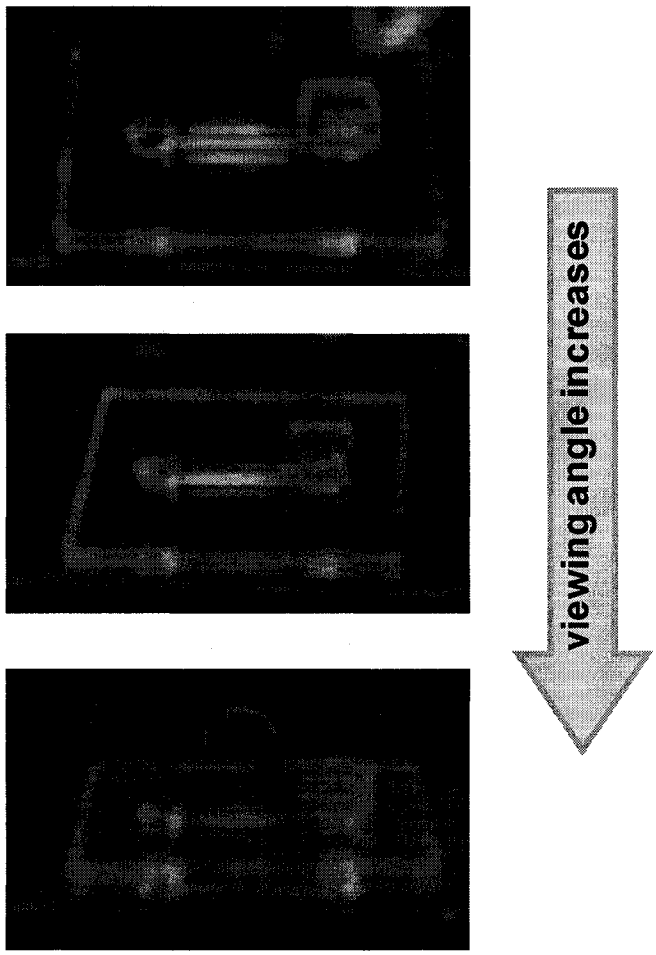

Figure 2-4. Digital images of a water filled colloidal nanoarray composed of 0.9-μm silica beads self-assembled within a single-channel PDMS chip mounted on a microscope stage. When illuminated by white light vertically from the bottom, the array exhibited monochromic transmitted light from blue to red as the viewing angle increases, which is due to Bragg diffraction.

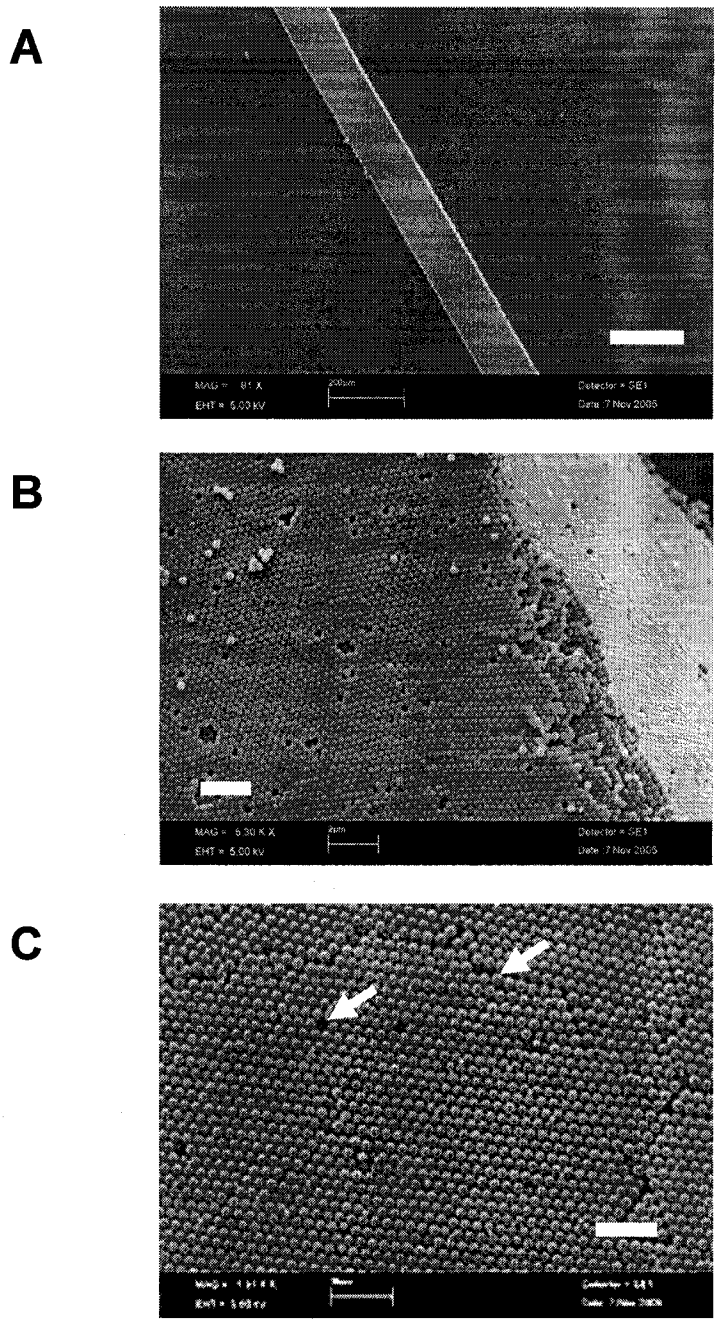

Figure 2-5. Scanning electron microscopy (SEM) characterization of self-assembled colloidal arrays within microfluidic systems. (A, B) SEM images of a matrix of 330-nm silica spheres at different magnifications. (C) SEM image of a hexagonally closed packed 2-μm PS colloidal array fabricated within a microchannel. The arrows indicate lattice defects. The scale bars are 200, 2, and 10 μm in (A–C), respectively.

and stacking faults, as seen in Figure 2-5B and C. These defects may affect the separation performance. However, they are randomly distributed and localized so that no accumulative effects, such as channeling of flow, will arise.

Our approach offers significantly greater assembly speed than conventional colloidal deposition approaches, which usually take tens of hours to days to construct colloidal arrays within microdevices [22, 28, 29]. For example, it takes less than 30 min for 10% w/v 0.9-μm silica colloids (~0.4–0.6 mm/min) and less than 60 min for 10% w/v 0.33-μm silica beads to pack a separation channel 1 cm in length under ambient conditions. The high assembly speed can be attributed to the large surface area of the protruding evaporation interface (Figure 2-3A). Compared to the design of microfabricated barrier structures with a gap size smaller than the particles to be trapped [29], our approach uses the air–liquid interface as a virtual frit to retain the microspheres, which offers advantages in terms of much larger evaporation area as well as simplified device fabrication. The high-speed assembly allows the packing of large particles of various materials, as exemplified by a regularly packed array of 2-μm PS colloids shown in Figure 2-5C. Large particles are problematic for slow vertical deposition due to their relatively rapid sedimentation [18]. The demonstrated ability of our approach to assemble large colloids allows an extended pore size range that can access diverse biomolecules with a wide size range, as shown below.

2.3.3 Characterization of EOF in Silica Colloidal Nanoarrays

Negative surface charges on particles in a colloidal array cause EOF. Here we characterized EOF mobilities of silica colloidal nanoarrays of two particle sizes under

various concentrations of TBE buffer using the modified current monitoring approach [32], as plotted in Figure 2-6A. As expected, the electroosmotic mobility decreases along with increasing buffer concentration, due to the fact that higher concentration confers a lower zeta potential and compresses the electrical double layer. The significant difference between the electroosmotic mobility of 330-nm and 900-nm silica colloidal arrays in 0.5× TBE buffer, as seen in Figure 2-6A, is diminished under highly concentrated buffers, also indicating less significance of the electric double layer in the pores. The thickness of the double layer under 4× TBE is estimated to be less than 1 nm, which is much smaller than the pore sizes of ~135 nm in 900-nm silica bead arrays and ~50 nm in 330-nm silica bead arrays.

EOF under 0.5× and 1× TBE was found to be faster than DNA electrophoretic mobility, masking any separation. With buffer concentrations higher than 2× TBE, separation of a low DNA mass ladder can be achieved, as shown in Figure 2-6B. The separation speed increases along with the buffer concentration, indicating that the electrophoretic mobility of DNA starts to dominate the electroosmotic mobility in the sieves. In subsequential experiments, 4× TBE was used to substantially quench EOF and speed up the separation process.

2.3.4 Size-Based Separation of DNA

Figure 2-7A shows a sequence of fluorescent images of the separation of a low DNA mass ladder at 15 V/cm in a microchip packed with 900-nm silica beads. Six equimolar dsDNA fragments from 100 to 2,000 bp were separated into distinct bands within the first 1 mm of the column in ~1.5 min, as seen in the last frame of Figure 2-7A.

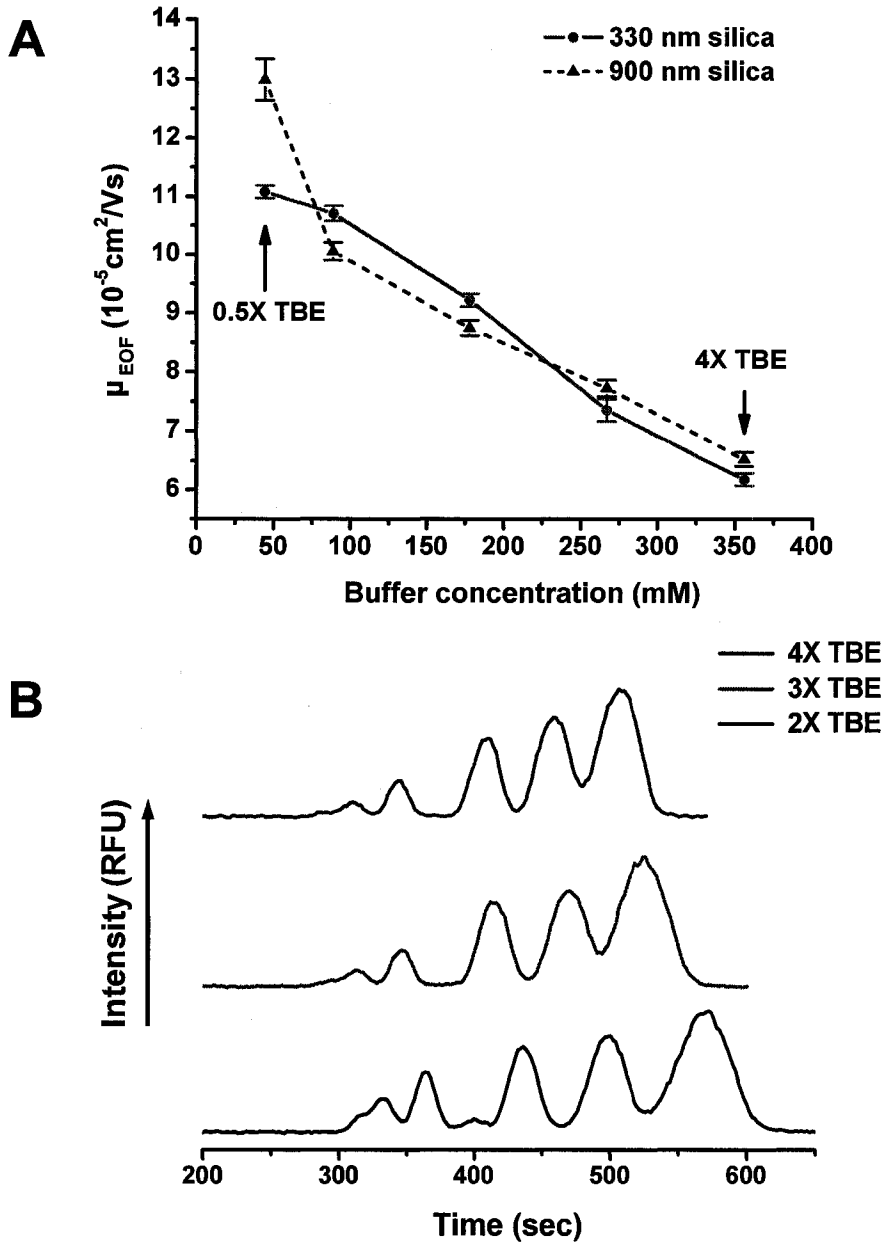

Figure 2-6. Characterization of EOF effects in silica colloidal nanosieves. (A) Electroosmotic mobility in self-assembled colloidal nanoarrays composed of 330- and 900-nm silica beads under various ionic strength buffers. (B) Separation of a low DNA mass ladder in a 0.9-μm silica bead nanoarray using 2–4× TBE buffer (E = 18.9 V/cm, separation length L = 5 mm).

The 100-bp band was hard to visualize in this low-magnification imaging mode (4× objective) because of its very low concentration. Four consecutive runs of the same ladder were performed in a 0.9-μm silica particle array and the electropherograms are superimposed in Figure 2-7B. In this case, the detector was located 5 mm from the injection point. The device was operated for ~5 h before this reproducibility test. The standard deviation of the migration time between these runs is less than 2%, which indicates the stability of the self-assembled colloidal sieves under the applied electric fields.

The bed stability is likely a result of van de Waals' forces between silica particles [23, 33], and the contribution from hydrogen bonds between the surfaces of close-packed silica particles. Matrixes composed of silica microspheres of 160, 330, and 900 nm and polystyrene beads of 770 and 1530 nm were found durable under applied fields as high as 60 V/cm. Redispersion of beads away from the packed bed may occur at the exits of the channels, but this is limited to a distance less than 200 μm into the channels. In this proof-of-concept study, no further steps were performed to strengthen the packed beds, as their stability was satisfactory. Further sintering can greatly enhance the adhesion by using additional modifications, such as thermal treatment [34]. However, this simple, rapid method for the preparation of nanofluidic sieve structures for biomolecular separation may not require greater stability, because of the ease of preparing new columns. Easily replaceable columns may also have benefits.

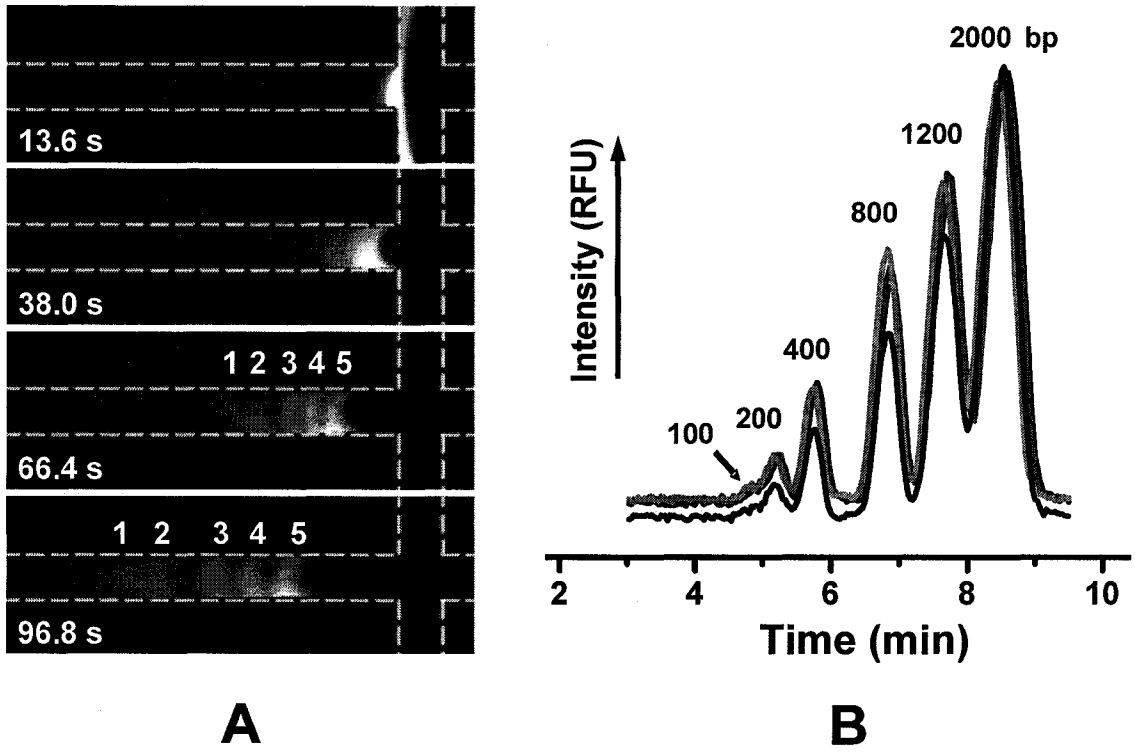

Figure 2-7. Separation of a low DNA mass ladder using 0.9-μm silica beads. (A) Sequence of fluorescent images of the electrophoretic separation at E = 15 V/cm. In this case the microchip has ~100 μm wide and ~20 μm deep microchannels with a cross injection design. Dashed lines were added to aid visualization of the microchannels. Frames are time-stamped in seconds. DNA fragments 1–5 are assigned as 200, 400, 800, 1200, and 2000 bp, respectively. The 100-bp band was not detected due to the very low concentration. (B) Four consecutive runs of the same ladder obtained in a device that had been operated for ~5 hours (E = 19.2 V/cm, separation length L = 5 mm).

2.4 CONCLUSIONS

We have establised a simple microfluidic colloidal self-assembly approach for fast and economic fabrication of ordered three-dimensional molecular sieving structures into microfluidic systems. The results presented here demonstrate the stability of self-packed colloidal nanosieves within microchannels and the flexibility of colloidal arrays in terms of the ability to precisely vary pore sizes. Such ability of our fabrication approach in the control of pore sizes is still challenging for conventional nanofabrication techniques, which demand sophisticated facilities and time-consuming and expensive procedures. Being compatible with inexpensive soft lithography processing, this approach may hold the potential of commercialization for mass production of disposable size-based separation devices.

2.5 REFERENCES

1. Kan, C. W.; Fredlake, C. P.; Doherty, E. A. S.; Barron, A. E. *Electrophoresis* **2004**, *25*, 3564–3588.

2. Yao, S.; Anex, D. S.; Caldwell, W. B.; Arnold, D. W.; Smith, K. B.; Schultz, P. G. *Proc. Natl. Acad. Sci. U.S.A.* **1999**, *96*, 5372–5377.

3. Herr, A. E.; Singh, A. K. *Anal. Chem.* **2004**, *76*, 4727–4733

4. Lin, Y. W.; Huang, M. F.; Chang, H. T. *Electrophoresis* **2005**, *26*, 320–330.

5. Volkmuth, W. D.; Austin, R. H. *Nature* **1992**, *358*, 600–602.

6. Han, J.; Craighead, H. G. *Science* **2000**, *288*, 1026–1029.

7. Han, J.; Craighead, H. G. *Anal. Chem.* **2002**, *74*, 394–401.

8. Cabodi, M.; Turner, S. W.; Craighead, H. G. *Anal. Chem.* **2002**, *74*, 5169–5174.

9. Cabodi, M.; Chen, Y. F.; Turner, S. W. P.; Craighead, H. G.; Austin, R. H. *Electrophoresis* **2002**, *23*, 3496–3503.

10. Chou, C. F.; Bakajin, O.; Turner, S. W. P.; Duke, T. A. J.; Chan, S. S.; Cox, E. C.; Craighead, H. G.; Austin, R. H. *Proc. Natl. Acad. Sci. U.S.A.* **1999**, *96*, 13762–13765.

11. Huang, L. R.; Tegenfeldt, J. O.; Kraeft, J. J.; Sturm, J. C.; Austin, R. H.; Cox, E. C. *Nat. Biotechnol.* **2002**, *20*, 1048–1051.

12. Kaji, N.; Tezuka, Y.; Takamura, Y.; Ueda, M.; Nishimoto, T.; Nakanishi, H.; Horiike, Y.; Baba, Y. *Anal. Chem.* **2004**, *76*, 15–22.

13. Fu, J.; Mao, P.; Han, J. *Appl. Phys. Lett.* **2005**, *87*, 263902.

14. Huang, L. R.; Cox, E. C.; Austin, R. H.; Sturm, J. C. *Science* **2004**, *304*, 987–990.

15. Han, J.; Turner, S. W.; Craighead, H. G. *Phys. Rev. Lett.* **1999**, *83*, 1688–1691.

16. Turner, S. W. P.; Cabod, M.; Craighead, H. G. *Phys. Rev. Lett.* **2002**, *88*, 1–4.

17. Velev, O. D.; Lenhoff, A. M. *Curr. Opin. Colloid Interface Sci.* **2000**, *5*, 56–63.

18. Vlasov, Y. A.; Bo, X.; Sturm, J. C.; Norris, D. J. *Nature* **2001**, *414*, 289–293.

19. Reese, C. E.; Asher, S. A. *Anal. Chem.* **2003**, *75*, 3915–3918.

20. Doyle, P. S.; Bibette, J.; Bancaud, A.; Viovy, J.-L. *Science* **2002**, *295*, 2237.

21. Nykypanchuk, D.; Strey, H. H.; Hoagland, D. A. *Science* **2002**, *297*, 987–990.

22. Meistermann, L.; Tinland, B. *Phys. Rev. E* **2000**, *62*, 4014–4017.

23. Zhang, H.; Wirth, M. J. *Anal. Chem.* **2005**, *77*, 1237–1242.

24. Zheng, S.; Ross, E.; Legg, M. A.; Wirth, M. J. *J. Am. Chem. Soc.* **2006**, *128*, 9016–9017.

25. Jiang, P.; Bertone, J. F.; Hwang, K. S.; Colvin, V. L. *Chem. Mater.* **1999**, *11*, 2132–2140.

26. Moon, J. H.; Kim, S.; Yi, G.; Lee, Y.-H.; Yang, S. M. *Langmuir* **2004**, *20*, 2033–2035.

27. Xia, Y.; Kim, E.; Whitesides, G. M. *J. Am. Chem. Soc.* **1996**, *11*, 9576–9577.

28. Ishii, M.; Nakamura, H.; Nakano, H.; Tsukigase, A.; Harada, M. *Langmuir* **2005**, *21*, 5367–5371.

29. Lu, Y.; Yin, Y.; Gates, B.; Xia, Y. *Langmuir* **2001**, *17*, 6344–6350.

30. Effenhauser, C. S.; Bruin, G. J. M.; Paulus, A.; Ehrat, M. *Anal. Chem.* **1997**, *69*, 3451–3457.

31. Dufresne, E. R.; Corwin, E. I.; Greenblatt, N. A.; Ashmore, J.; Wang, D. Y.; Dinsmore, A. D.; Cheng, J. X.; Xie, X. S.; Hutchinson, J. W.; Weitz, D. A. *Phys. Rev. Lett.* **2003**, *91*, 224501.

32. Huang, X.; Gordon, M.J.; Zare, R. N. *Anal. Chem.* **1988**, *60*, 1837-1838.

33. Norris, D. J.; Arlinghaus, E. G.; Meng, L.; Heiny, R.; Scriven, L. E. *Adv. Mater.* **2004**, *16*, 1393–1399.

34. Ceriotti, L.; de Rooij, N. F.; Verpoorte, E. *Anal. Chem.* **2002**, *74*, 639–647.

Chapter 3

Molecular Sieving within Self-Assembled Three-Dimensional Colloidal Nanosieves*

3.1 INTRODUCTION

Self-assembled colloidal nanoarrays are composed of regularly organized monodispersed particles. Nanometer-sized interstices in the close-packed sphere lattice create a nanofluidic sieve that consists of voids interconnected by narrower pores, as sketched in Figure 3-1, which have an equivalent diameter ~15% of the sphere size. Molecules experience a loss in entropy by steric constriction while traveling through a constraining pore [1]. Thus, the porous structure imposes periodically modulated free-energy barriers to molecular transport, which is presumably responsible for size-dependent separation of molecules with dimensions comparable to the narrower pore sizes.

In this chapter, we focus on the detailed characterization of the performance of gel-free size fractionation of biomolecules within this novel sieving matrix and the discussion of the molecular sieving mechanism underlining the biomolecular size separation using steady electric fields. A variety of self-assembled colloidal sieves were tested to demonstrate the capability of this colloidal nanofabrication technique in terms of

* A version of this chapter has been published. Zeng, Y.; Harrison, D. J. *Anal. Chem.* **2007**, *79*, 2289-2295.

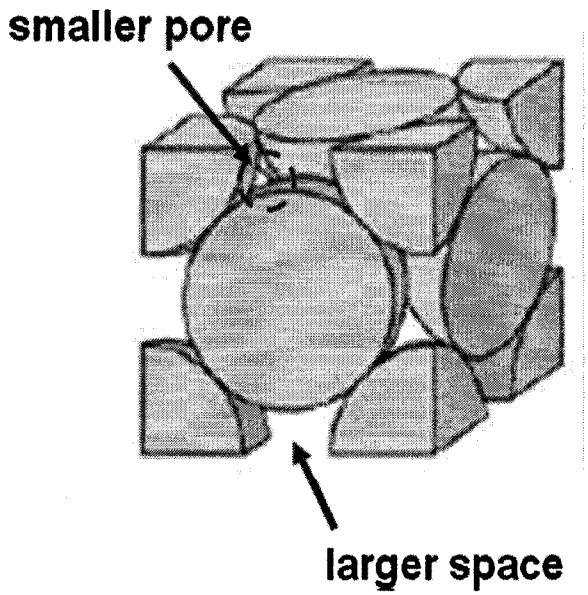

Figure 3-1. Schematic drawing of porous structure created in face-centred-cubic stacking of spherical particles.

precise control of pore sizes to target different biological macromolecules with a wide size distribution, such as sodium dodecyl sulfate (SDS)–protein complexes, short and long DNA fragments.

3.2 MATERIALS AND METHODS

3.2.1 Reagents and Samples

All reagents and samples were prepared using deionized water (18.2 MΩ) obtained from an Ultrapure water system (Millipore, Milford, MA). Monodisperse plain polystyrene (PS) microspheres (2.62% w/v, 1.53 ± 0.039 μm in diameter) and silica beads (10% w/v, 0.90 ± 0.04 μm in diameter) were obtained from Polysciences (Warrington, PA). The pore sizes of the lattices assembled from these particles are listed in Table 3-1. Uniform silica beads of 160 and 330 nm in diameter (10% w/v, <10%

deviation) were obtained from Bangs Laboratories. Various DNA samples were used, including bacteriophage λ-DNA and calf thymus DNA (ultrapure, ~13 kbp, Sigma, St. Louis, MO), 50-bp DNA ladder (Amersham Pharmacia Biotech, Piscataway, NJ), PCR marker (Promega, Madison, WI), and other DNA markers and ladders from Invitrogen. DNA samples were stained as described in Chapter 2. Final DNA concentrations were 10–60 ng/μL. For denatured protein separation, trypsin inhibitor (soybean, 20.1 kDa), ovalbumin (chicken egg, 45 kDa), bovine serum albumin (66 kDa), phosphorylase B (rabbit muscle, 97 kDa), β-galactosidase (*Escherichia coli*, 116 kDa), and myosin (rabbit muscle, 205 kDa) (Sigma, St. Louis, MO) were used as molecular weight standards. Proteins were conjugated with Alexa Fluor 488 (Molecular Probes, Eugene, OR). The concentration of proteins varied from 10^{-6} to 10^{-4} M after labeling. An aliquot of each protein solution was mixed with the same volume sample buffer (4× TBE buffer, 4% w/v SDS, 8% v/v 2-mercaptoethanol) and then incubated at 85 °C for 5 min. After denaturizing, protein samples were diluted with buffer solution (4× TBE buffer, 0.1% w/v SDS), and mixed before separation with the final concentration of each component adjusted to 10^{-8}–10^{-7} M in the mixture.

3.2.2 Separation and Fluorescence Detection

Electrophoretic separation under DC electric fields and fluorescent detection were performed as described in Chapter 2. Plain PS microspheres contain slight anionic surface charges from sulfate ester, so that some EOF is present. EOF in PS nanoarrays was found to be effectively suppressed using 0.11wt % Poly(vinylpyrrolidone) (PVP, M_w = 10^6) dissolved in 1× TBE buffer. Denaturing separation of SDS-protein complexes was

Table 3-1. Summary of Pore Sizes and Effective Size Ranges for the Colloidal Sieves Constructed with Various Particles

particles with nominal size (nm)	pore size[a] (nm)	effective size range[b]		equivalent gels[d]
		DNA (bp)	protein (kDa)	
silica, 900	~ 135	100 – 2000[c]	—	2% agarose gel
silica, 330	~ 50	50 – 1000	100–205	2-3% agarose or 4 T% polyacrylamide gel
silica, 160	~ 24	—	20–205	6 T% polyacrylamide gel

[a] Calculated as ~15% particle sizes. [b] Determined for linear dsDNA and SDS-denatured proteins. [c] Tested to separate long DNA molecules up to ~50 kbp. [d] Compared according to the targeted size range of separation.

conducted using 4× TBE containing 0.1% w/v SDS as the running buffer. To facilitate fluorescence imaging, PDMS microchips with a 100-μm offset double-T injector were used to increase the amount of injection. The dimensions of microchannels were ~120 μm wide and ~20 μm deep. The buffer and injection channels were 4 mm long and the separation channel was 10 mm in length. A plan-fluotar 100× oil-immersion objective (1.3 N.A., Leica, Germany) was used for single-molecule visualization.

3.3 RESULTS AND DISCUSSION

3.3.1 Separation Performance of Small DNA Molecules

The performance of small DNA separation in the 0.9-μm colloidal array was investigated at different electric fields, three of which are presented in Figure 3-2A. The ratio of peak heights roughly corresponds to the mass ratio of DNA fragments in the

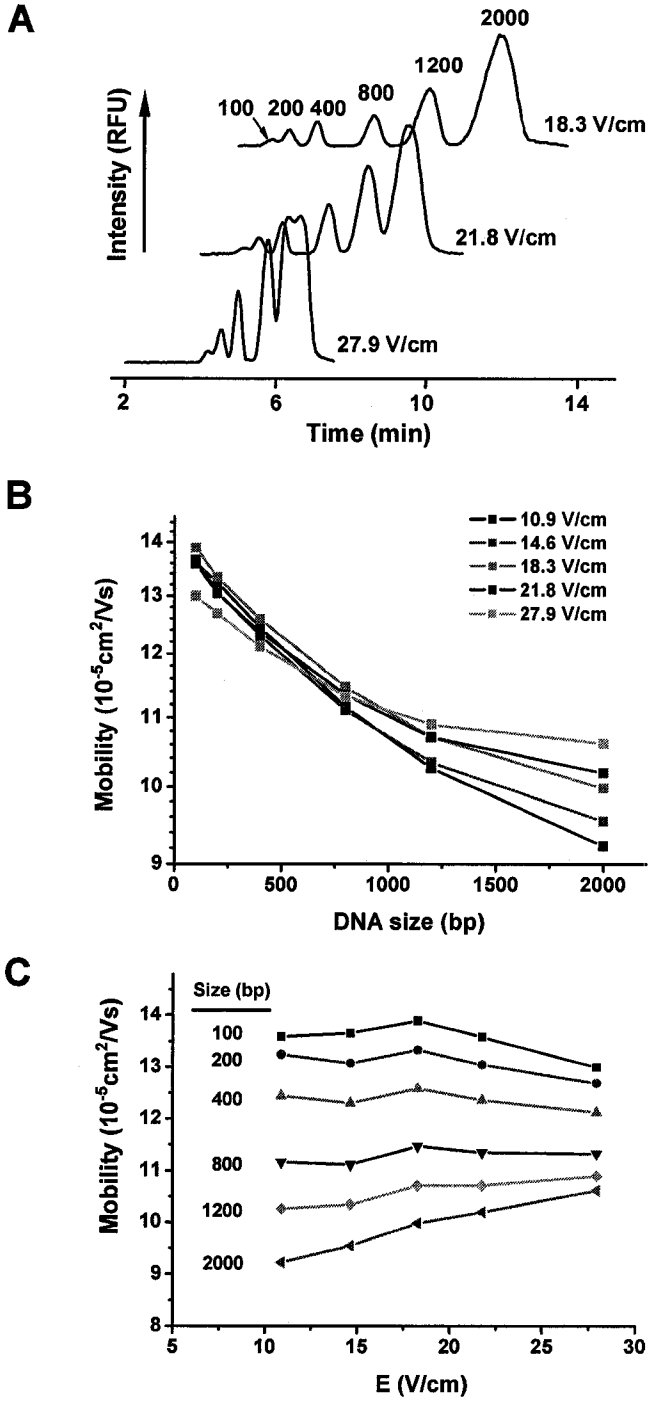

Figure 3-2. Influence of electric field on size separation of DNA fragments. (A) Electropherograms of a low DNA mass ladder under varied electric fields. The traces were offset for clarity. (B) Semi-log plot of mobility vs. DNA size at various electric fields. (C) Plot of mobility of DNA fragments of different sizes as a function of electric field. Conditions: 0.9-μm silica colloids, L = 5 mm.

ladder, allowing direct identification of individual peaks. To characterize the separation efficiency, the theoretical plate numbers were calculated as $N = 5.545(t/W_{1/2})^2$, where t is the elution time and $W_{1/2}$ for the width at half peak height of the Gaussian fitted peaks. The sieving performance under various electric fields was also quantified by the separation resolution, which is defined as the ratio of the peak separation ΔX to the averaged baseline width of two adjacent peaks: $R_s = 2\Delta X/(W_1 + W_2)$. These results are summarized in Table 3-2.

The plate numbers were 3.9–4.9 × 10^3 for the 400-bp peak, which corresponds to plates per meter of 7.8–9.8 × 10^5 m^{-1}. This separation efficiency compares favorably with nanofabricated structures [2, 3] and microsystems filled with gels or liquid polymer matrixes [4-6]. The 0.9-μm microsphere array effectively separates dsDNA between 100 and 2000 bp, and is analogous to a 2% agarose gel, which renders pore sizes of 160–300 nm [7, 8] and targets dsDNA of 0.1–3 kbp, as summarized in Table 3-1.

As evident in Table 3-2, the resolution, R_s, appears to be field dependent, especially for larger DNA fragments. As the electric field decreases from 27.9 to 18.3 V/cm, R_s increases 49% (from 2.1 to 3.1) for 400–800 bp, in contrast to an increase of 146% for 1200–2000 bp (from 0.72 to 1.8). To interpret the field-dependency of DNA separations, the mechanism of size-based separation in the colloidal sieves needs to be discussed. The gyration radius of a Gaussian polymer chain is estimated by $R_g = (lL/6)^{1/2}$, where l is the Kuhn length and L the contour length [9]. R_g of 1- and 2-kbp dsDNA molecules are estimated to be ~75 and ~106 nm, respectively, slightly larger than the restrictive pores (~135 nm) in a 0.9-μm colloidal sieve. Therefore, Ogston sieving is

Table 3-2. Summary of Separation Performance of DNA Fragments of 100–2000 bp Using 0.9-μm Silica Colloids under Various Electric Fields as Shown in Figure 3-2

E	400 bp		1200 bp		2000 bp		Resolution	
(V/cm)	N/m	H(μm)	N/m	H(μm)	N/m	H(μm)	400/800	1200/2000
18.3	9.8E5	1.0	4.7E5	2.1	2.7E5	3.7	3.1	1.8
21.8	8.5E5	1.2	4.1E5	2.5	2.8E5	3.5	2.6	1.2
27.9	7.8E5	1.3	4.2E5	2.4	4.3E5	2.3	2.1	0.72

expected as the dominant process for DNA fragments smaller than the pore size, and the crossover to the reptation regime may occur for the largest two fragments.

3.3.2 Molecular Sieving Mechanism

A semilog plot of DNA mobility as a function of molecular size, as shown in Figure 3-2B, exhibits fairly good linearity for small DNA strands. This linear function is consistent with the Ogston model which predicts $\mu \sim \exp(-M)$ with a given gel concentration [10, 11]. Deviation from the linear relationship was significant for 2000-bp fragment, especially under relatively high fields, which suggests a transition to the reptation regime. Figure 3-2C explicitly illustrates the influence of the electric field on the DNA mobility. The relative independence of the mobility of smaller DNA on the electric field further confirms the Ogston sieving mechanism, while 2000-bp DNA seems to obey the biased reptation model with fluctuations (BRF) that predicts a linear dependence of mobility on field strength [11, 12].

Figure 3-3A demonstrates the separation of a 100-bp dsDNA ladder using a 900-nm colloidal nanoarray, where the 600-bp fragment was spiked by the manufacturer to

ease peak assignment. It is evident that the pore size of 900-nm colloidal nanoarrays generates sufficient separation resolution to resolve less than 100-bp mass differences in this molecular weight range. The detection set up was built for DNA imaging, which

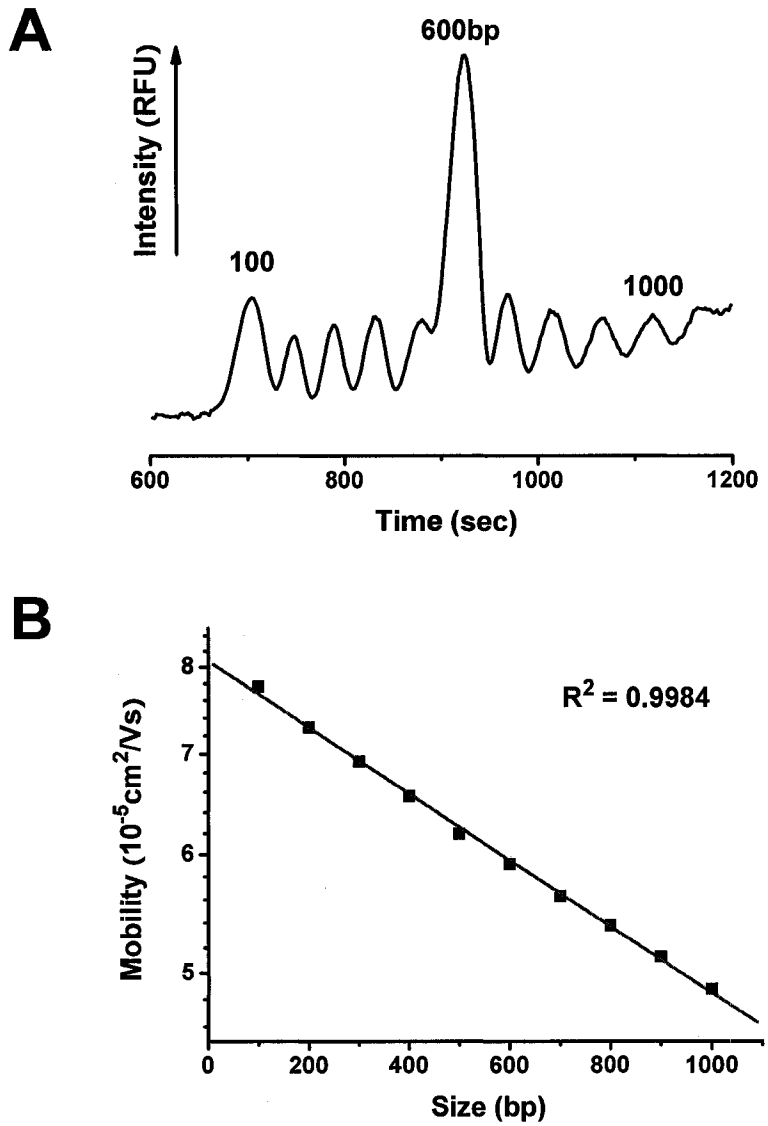

Figure 3-3. Sizing 100-bp DNA ladder. (A) Electropherogram of a 100-bp DNA ladder separated using 900-nm silica beads (E = 16.5 V/cm, L = 9 mm). (B) Semi-log plot of apparent electrophoretic mobility as a function of DNA molecular size and its least-squares linear fit.

gives poorer detection sensitivity than the widely used confocal detection scheme [13]. As a result, a large total amount of sample (~ 100 ng/μl DNA ladder concentration) was loaded to ensure good detection of individual peaks. This sample overloading, indicated by the slight fronting of peaks and the baseline shifting in Figure 3-3A, results in lower separation efficiency and resolution. Further optimization of separation and detection conditions would achieve better separation performance in terms of speed and resolution. The apparent electrophoretic mobilities of individual DNA fragments were calculated and plotted against their molecular weight, as presented in Figure 3-3B. This semi-log function exhibits very good linearity (R^2 = 0.9984) for the DNA size range of 100–1000 bp, in further support of the molecular sieving mechanism.

3.3.3 Effect of Pore Size on Small DNA Separation

Higher resolving power can be achieved using smaller particles to reduce the pore sizes. Figure 3-4A demonstrates the clear fractionation of a 50-bp ladder using 330-nm silica beads under a higher electric field compared to Figure 3-3A. To explore the effective separation range, a mixture of a PCR marker and a low DNA mass ladder was separated in this colloidal nanosieve of 330-nm silica beads. Ten of a total 12 peaks were identified in the separation (Figure 3-4B). The 100-bp peak of low abundance was blurred by the strong 50-bp peak, and the 2-kbp peak was excluded during data collection due to its very slow migration. The plates per meter for each peak were in the range of 0.2–1.4 × 10^6 m^{-1}. The resolving power was sufficient to separate two fragments with a 50-bp difference up to 800 bp (R_s = 0.89 for 750 and 800 bp), but dropped with further increasing DNA size (R_s = 0.86 for 1000 and 1200 bp), indicating the 330-nm colloidal

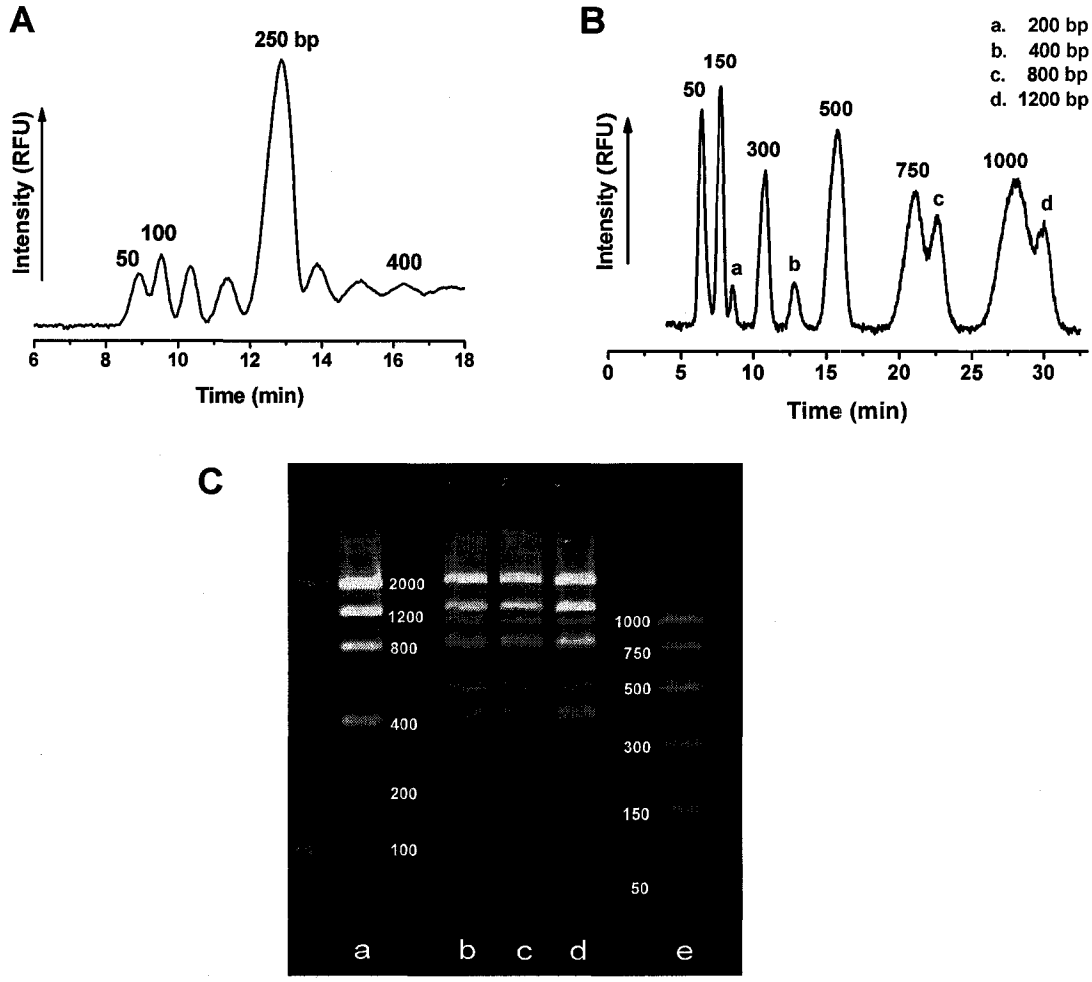

Figure 3-4. Separation of small DNA molecules. (A, B) DNA separation using 330-nm silica beads: (A) 50-bp ladder (E = 17.6 V/cm, L = 8 mm); (B) a mixture of PCR marker (peaks marked by bp) and low DNA mass ladder (peaks labeled a–d, the low abundance 100-bp peak was buried by the strong 50-bp peak and the 2-kbp peak was excluded due to its long migration time) (E = 17.6 V/cm, L = 5 mm). (C) Fluorescent image of a mixture of low DNA mass ladder (42 ng/μL) and PCR marker (27 ng/μL) separated by slab gel electrophoresis. Lane assignment: a) low DNA mass ladder (8 μL application), b-c) low DNA mass ladder (5 μL) and PCR marker(5 μL), d) low DNA mass ladder (8 μL) and PCR marker (4 μL), e) PCR marker (8 μL). Conditions: DNA samples were pre-stained by YOYO-1 as described before; 2% agarose gel; 1× TBE buffer; E = 17 V/cm; 25 min running time. The arrows point out the two components unidentified in (B).

sieve (~50-nm pore) is efficient for linear dsDNA of 50–1000 bp. Figure 3-4C shows a fluorescence image of this mixture, separated by slab gel electrophoresis to help identify all 12 fragments. The 100-bp component was also not readily seen in the gel, while the 2000-bp peaks seen in the gel was not observed in the chip because the runs were terminated too soon.

3.3.4 Size Separation of Long DNA Molecules

Use of this colloidal array to separate long DNA chains under constant electric fields is of great interest. Fractionation of calf thymus DNA (~13 kbp) from λ-DNA (48.5 kbp) can be completed in a 0.9-μm silica sieve (~135-nm pore) within several minutes, as demonstrated in Figure 3-5A. This speed is comparable to that seen for a magnetically assembled colloidal post array [14], but is much faster than that seen in gel with pulsed fields. The 0.9-μm silica array did not resolve a mixture of λ-DNA (48.5 kbp) and T4 GT7 DNA (166 kbp), whereas a 1.53-μm sphere array was able to achieve high-speed separation of these two large molecules within 3 min in a 1.5-mm separation distance (R_s = 0.94), as evident in Figure 3-5B. The results demonstrate the relationship between pore size in the sphere array and the size of the molecules to be separated.

To understand the separation mechanism, the electrophoresis of single DNA molecules of 20 and 48.5 kbp under the steady electric field was visualized using epifluorescence videomicroscopy as in Figure 3-6. Smaller DNA molecules of 20 kbp migrated in a fairly compact conformation and experience insignificant elongation, as seen in Figure 3-6A. In strong contrast, Figure 3-6B depicts that larger λ-DNA chains underwent cyclic migration of contraction and significant extension and more frequent

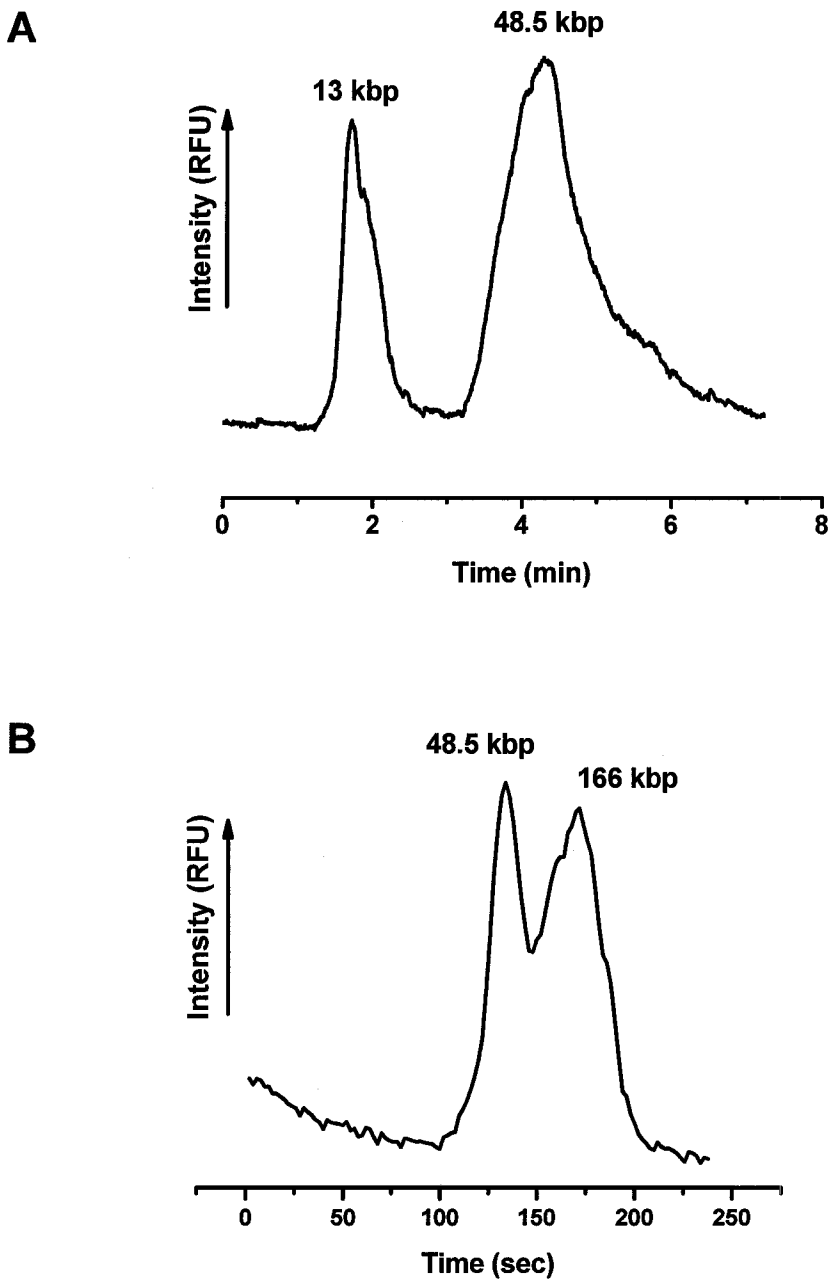

Figure 3-5. Rapid separation of large DNA molecules. (A) Separation of calf thymus DNA (13 kbp) and λ-DNA (48.5 kbp) within a 0.9-μm silica sphere array (E = 30 V/cm, L = 2 mm). (B) Separation of a mixture of λ-DNA and T4 GT7 DNA (166 kbp) using 1.53-μm polystyrene spheres (E = 14 V/cm, L = 1.5 mm). Buffer: 1× TBE containing 4% v/v 2-mercaptoethanol and 0.1% (wt/vol) PVP ($M_w = 10^6$).

hooking entanglement around the neck between two touching spheres (seen as U-shaped elongation) during electromigration. These effects result in more retardation of larger λ-

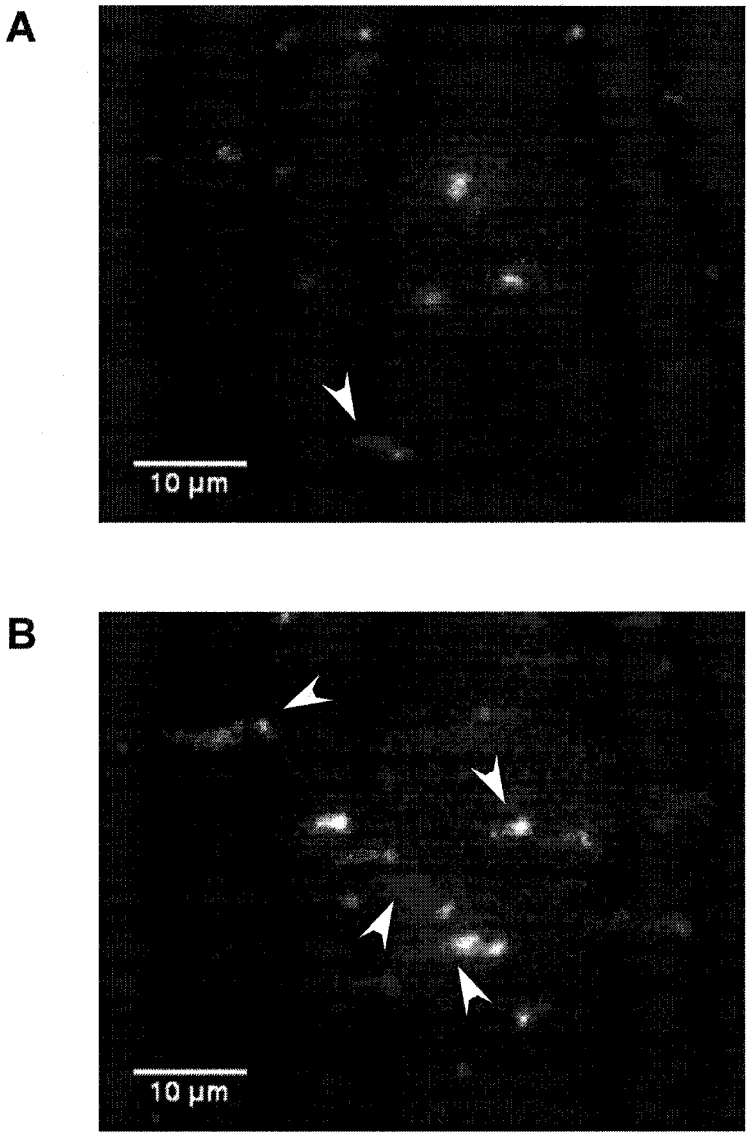

Figure 3-6. Fluorescent images of single DNA molecule electrophoresis. (A) 20-kbp and (B) 48.5-kbp DNA molecules electromigrating in 900-nm nanosieves at 30 V/cm, respectively. The arrowhead in (A) points the partially elongated DNA chain. The arrowheads in (B) point the U-shaped hooked DNA molecules.

DNA molecules. Hooking entanglement is a well-recognized mechanism for long DNA separation in polymer matrix [11, 15], randomly dispersed gold nanoparticle/polymer composites [16], post arrays [14, 17, 18], and colloidal arrays [19].

3.3.5 Separation of SDS-Denatured Proteins

Sieving-based protein separation in these porous beds is an obvious objective, made challenging by the very small pore size required. Figure 3-7 exhibits separation of SDS-denatured protein markers using differently sized silica particles. Four proteins of 20–205 kDa were separated in a matrix of 330-nm silica spheres (~50-nm pore size, E = 19.1 V/cm, L = 8 mm), as shown in Figure 3-7A. The resolution was 2.6 between the 20.1- and 116-kDa proteins and 3.9 between the 116- and 205-kDa proteins, respectively, which indicates a better size selectivity for larger proteins than smaller ones.

Figure 3-7B demonstrates that the separation efficiency was greatly improved for the size range of 20–116 kDa using a 160-nm silica particle array (~24-nm pore). Five proteins were baseline resolved, despite a shorter separation distance of 4 mm (E = 30.9 V/cm). This result is consistent with Ogston theory, which predicts an optimal efficiency for globular species that are close in size to the pores in the sieving matrix [11]. Figure 3-8 shows a plot of logarithmic electrophoretic mobility against protein molecular weight. The averaged mobility for each size standard was determined from the separations (n = 7) performed under the same conditions as in Figure 3-7B. The relative standard deviation in mobility is less than 8% for the five standards. A linear least-squares fit to the data shows good linearity (R^2 = 0.9911), which further confirms Ogston sieving as the essential mechanism in the well-defined pores of 160-nm colloidal arrays.

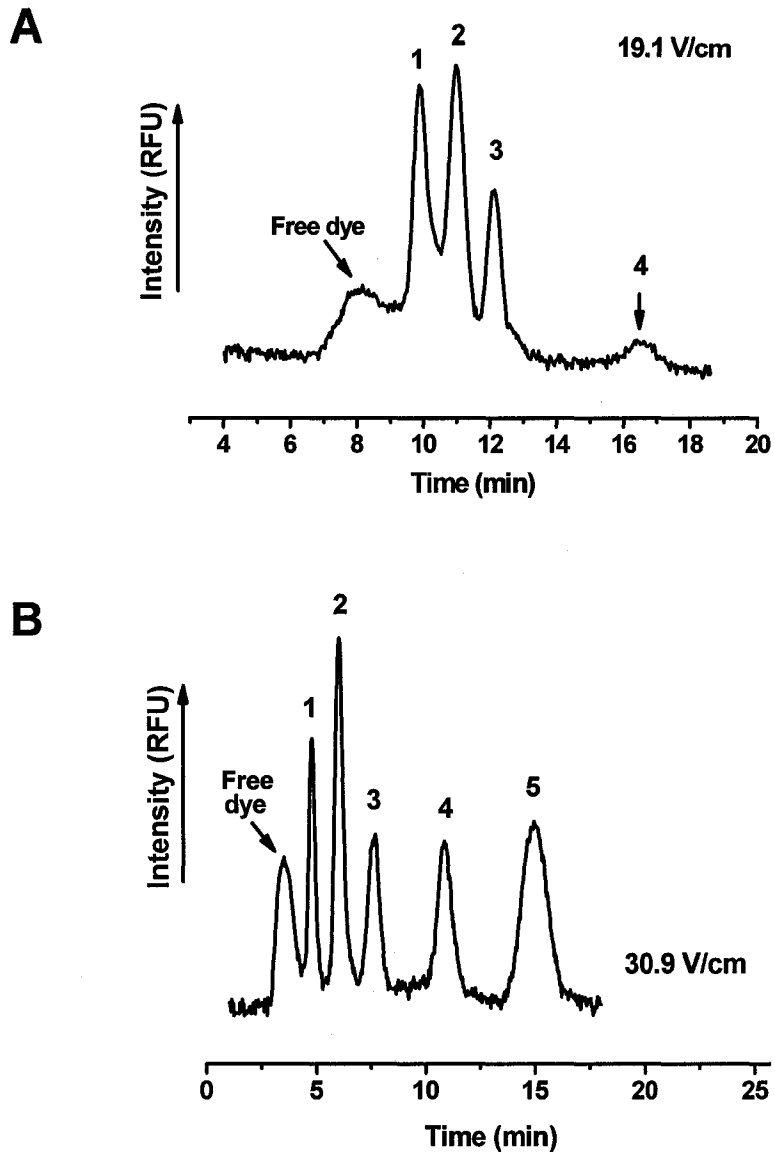

Figure 3-7. Separation of SDS denatured proteins. (A) Separation of four proteins using 330-nm silica particles (E = 19.1 V/cm, L = 8 mm): (1) trypsin inhibitor, 20.1 kDa; (2) BSA, 66 kDa; (3) β-galactosidase, 116 kDa; and (4) myosin, 205 kDa. (B) Separation of five proteins using 160-nm silica particles (E = 30.9 V/cm, L = 4 mm): (1) trypsin inhibitor, 20.1 kDa; (2) ovalbumin, 45 kDa; (3) BSA, 66 kDa; (4) phosphorylase B, 97 kDa; (5) β-galactosidase, 116 kDa. A broad peak appeared before the first peak, due to the residual free dye from the labeling process.

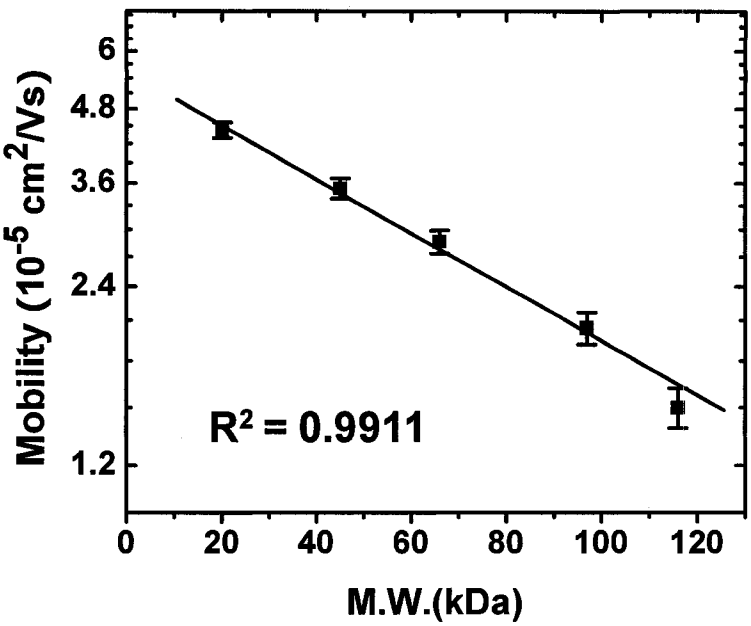

Figure 3-8. Semi-log plot of the apparent mobility of SDS-protein complex vs. protein molecular weight with a least-squares linear fit. The averaged mobility was determined from the electrophoretic separations of five protein standards performed under the same conditions as described in Figure 3-7B. Error bars are standard deviation (n = 7).

The separation performance in the 160-nm colloidal nanosieves was systematically examined at various electric fields. Results are summarized in Figure 3-9 and Table 3-3. The plates per meter ranged from 2.3–5.3 × 10^5 m^{-1}, which correspond to a range of plate heights of 1.9–4.3 μm. These efficiencies are comparable to microfabricated nanofilter arrays [2] and microsystems using conventional gel/polymer matrixes [20-22]. To characterize the resolving power of the 160-nm colloidal nanosieves, the minimum resolvable molecular weight difference was estimated using $R = \Delta M/R_s$, where ΔM and R_s denote the mass difference and the resolution between two peaks, respectively. Table 3-4 lists out the results of the minimum resolvable molecular

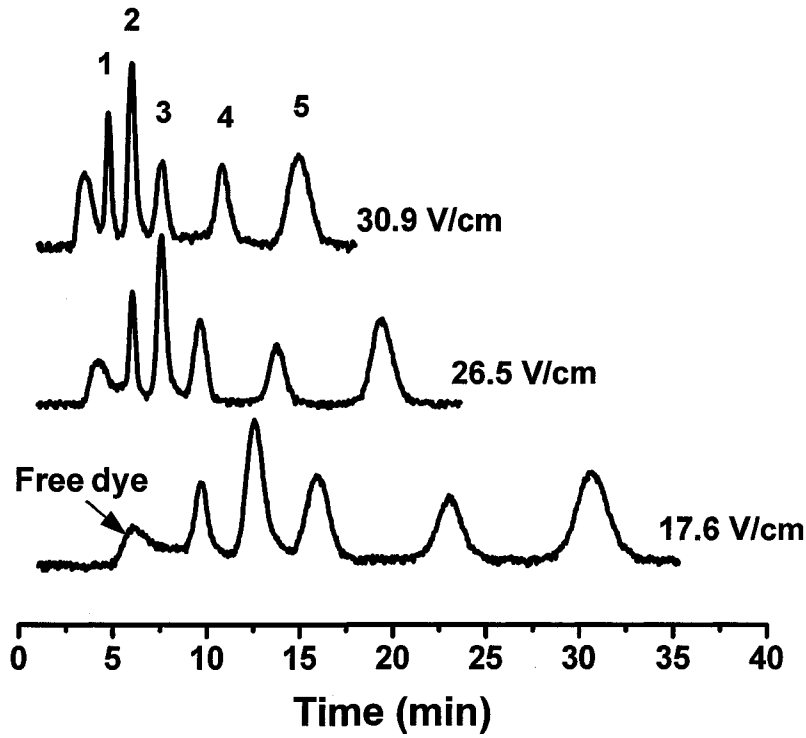

Figure 3-9. Size separation of SDS-denatured proteins using 160-nm silica particles under various electric fields (L = 4 mm). Peak assignment: (1) trypsin inhibitor, 20.1 kDa; (2) ovalbumin, 45 kDa; (3) BSA, 66 kDa; (4) phosphorylase B, 97 kDa; (5) β-galactosidase, 116 kDa. A broad peak appeared before the first peak, due to the residual free dye from the labeling process.

Table 3-3. Separation Efficiency for SDS-denatured Proteins of 20–116 kDa Using 160-nm Silica Colloids under Various Electric Fields as Shown in Figure 3-9

E (V/cm)	Peak 1		Peak 3		Peak 4		Peak 5	
	N/m	H (μm)	N/m	H (μm)	N/m	H (μm)	N/m	H (μm)
17.6	2.3E5	4.3	2.6E5	3.8	4.8E5	2.1	5.1E5	2.0
26.5	4.4E5	2.3	3.4E5	2.9	5.0E5	2.0	5.3E5	1.9
30.9	4.1E5	2.4	3.3E5	3.1	4.5E5	2.2	3.3E5	3.1

Table 3-4. Separation Resolution of SDS-denatured Proteins of 20–116 kDa Using 160-nm Silica Colloids at E = 30.9 V/cm as Shown in Figure 3-9

30.9 V/cm	20.1/45 kDa	45/66 kDa	66/97 kDa	97/116 kDa
R_s	2.3	2.2	3.5	3.1
R (kDa)	10.9	9.6	8.9	6.2

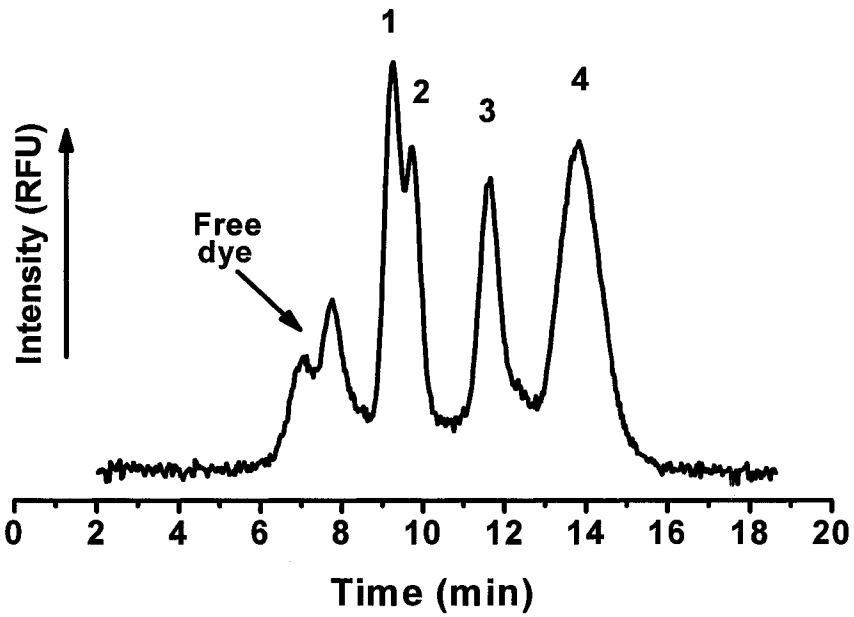

Figure 3-10. Size separation of SDS-denatured proteins using 160-nm silica particles (E = 30.9 V/cm, L = 8 mm). Peak assignment: (1) trypsin inhibitor, 20.1 kDa; (2) carbonic anhydrase, 29 kDa; (3) ovalbumin, 45 kDa; (4) BSA, 66 kDa.

weight difference between each two adjacent peaks obtained using 160-nm beads at E = 30.9 V/cm. R is equal to 8.8 kDa for 66–97 kDa and 6.2 kDa for 97–116 kDa, which are comparable to microsystems using gel/polymer matrixes [21]. Figure 3-10 demonstrates that two proteins of ~9-kDa difference in mass (trypsin inhibitor of 20.1 kDa and

carbonic anhydrase of 29 kDa) can be discriminated from each other, which is consistent with the calculation, R = 10.9 kDa for 20.1–45-kDa mass range, as listed in Table 3-4.

3.4 CONCLUSIONS

We have characterized the performance of biomolecular separation within a variety of self-assembled colloidal sieves and discussed the molecular sieving mechanism underlining the biomolecular size separation. The results presented here demonstrate the flexibility of colloidal arrays in terms of the ability to precisely vary pore sizes to adjust the separation performance for a given type of biomolecule. The ability of our fabrication approach to access a wide molecular scope, ranging from proteins smaller than 10 nm to micrometer-sized long DNA coils, is challenging for conventional nanofabrication techniques, which demand sophisticated facilities and time-consuming and expensive procedures. Compared to lithographically fabricated sieving structures and microsystems using gel/polymer matrixes, the colloidal nanosieves provide comparable separation efficiency. Self-assembled colloidal array may provide an ideal system for experimentally and theoretically understanding mechanisms underlying biomolecular separation in porous media, due to the well-ordered, well-defined structure.

3.5 REFERENCES

1. Giddings, J. C. *Unified Separation Science*; Wiley: New York, 1991.

2. Fu, J.; Mao, P.; Han, J. *Appl. Phys. Lett.* **2005**, *87*, 263902.

3. Fu, J.; Yoo, J.; Han, J. *Phys. Rev. Lett.* **2006**, *97*, 018103.1-3.

4. Hong, J. W.; Hosokawa, K.; Fujii, T.; Seki, M.; Endo, I. *Biotechnol. Prog.* **2001**, *17*, 958–962.

5. Ugaz, V. M.; Lin, R.; Srivastava, N.; Burke, D. T.; Burns, M. A. *Electrophoresis* **2003**, *24*, 151–157.

6. Emrich, C. A.; Tian, H.; Medintz, I. L.; Mathies, R. A. *Anal. Chem.* **2002**, *74*, 5076–5083.

7. Pernodet, N.; Tinland, B.; Sturm, J.; Weill, G. *Biopolymers* **1999**, *50*, 45–59.

8. Maaloum, M.; Tinland, B.; Weill, G. *Electrophoresis* **1998**, *19*, 1606–1610.

9. de Gennes, P.-G. *Scaling Concepts in Polymer Physics*; Cornell University Press: Ithaca, NY, 1979.

10. Ogston, A. G. *Trans. Faraday Soc.* **1958**, *54*, 1754–1757.

11. Viovy, J.-L. *Rev. Mod. Phys.* **2000**, *72*, 813–872.

12. Meistermann, L.; Tinland, B. *Phys. Rev. E* **2000**, *62*, 4014–4017.

13. Ocvirk, G.; Tang, T.; Harrison, D. J. *The Analyst*, **1998**, 123, 1429–1434.

14. Doyle, P. S.; Bibette, J.; Bancaud, A.; Viovy, J.-L. *Science* **2002**, *295*, 2237.

15. Shi, X.; Hammond, R. W.; Morris, M. D. *Anal. Chem.* **1995**, *67*, 1132–1138.

16. Huang, M.-F.; Kuo, Y.-C.; Huang, C.-C.; Chang, H.-T. *Anal. Chem.* **2004**, *76*, 192–196.

17. Volkmuth, W. D.; Austin, R. H. *Nature* **1992**, *358*, 600–602.

18. Kaji, N.; Tezuka, Y.; Takamura, Y.; Ueda, M.; Nishimoto, T.; Nakanishi, H.; Horiike, Y.; Baba, Y. *Anal. Chem.* **2004**, *76*, 15–22.

19. Zhang, H.; Wirth, M. J. *Anal. Chem.* **2005**, *77*, 1237–1242.

20. Yao, S.; Anex, D. S.; Caldwell, W. B.; Arnold, D. W.; Smith, K. B.; Schultz, P. G. *Proc. Natl. Acad. Sci. U.S.A.* **1999**, *96*, 5372–5377.

21. Herr, A. E.; Singh, A. K. *Anal. Chem.* **2004**, *76*, 4727–4733.

22. Nagata, H.; Tabuchi, M.; Hirano, K.; Baba, Y. *Electrophoresis* **2005**, *26*, 2687–2691.

Chapter 4

Large-Scale Microfluidic Self-Patterning of Crystalline Nanoarrays for High-Throughput Continuous DNA Fractionation*

4.1 INTRODUCTION

Self-assembly offers an attractive route to produce macroscopic functional ensembles from microscopic building blocks, such as macromolecules, colloids, nanotubes, and nanowires [1, 2]. Spontaneous organization of monodispersed colloids into crystalline arrays, dubbed colloidal self assembly (CSA), has been extensively explored in a variety of areas, such as the design of materials [3], photonics [4, 5], optical transducers for sensors [6], and molecular separation [7, 8]. High quality planar colloidal films with minimal lattice defects and large domain sizes have been achieved [9, 10]. Success in many applications will also demand the ability to pattern self-assembled colloidal lattices in well-defined architectures or within integrated microsystems [8, 11-13]. A number of patterning methods have been developed, including physical confinement [12-14], microcontact printing [15], electric field-assisted patterning [16], and surface-directed patterning [17]. Large-scale colloidal patterning, however, still suffers from long processing time and major defects, particularly cracks. Herein, we

* A version of this chapter has been submitted for publication. Zeng, Y.; Harrison, D. J. *Proc. Natl. Acad. Sci. U.S.A.* **2007**.

report a microfluidic approach for self patterning large-scale colloidal nanoarrays into microdevices, which controls evaporation-induced colloidal crystallization to avoid the formation of cracks. This approach is simple, fast, and highly compatible with standard soft lithography.

To exemplify the applications of this technique, a large-area colloidal nanoarray patterned within a microsystem was demonstrated for molecular sorting structure for continuous pulsed-field separation of DNA. Its counterparts, namely, conventionally micro-/nanofabricated structures have been widely used for bioseparations [18-27]. Such artificial gel structures feature precise control of topology, which catalyzes the understanding and exploration of new separation mechanisms, such as entropic trapping [20] and laminar flow bifurcation [25]. However, their practical applications are largely impeded by current technical limitations of nanolithography, such as high cost, tedious fabrication, and challenges in fabrication at 10-nm length scales. In this regard, CSA provides a simple and cost-effective alternative, especially for large-area patterning of nanoscale features. For instance, compared to two-dimensional (2D) microdevices with microfabricated post arrays [22, 23], the device presented here demands much less effort and cost for fabrication; it possesses a 3D periodic porous structure, which eases operation and improves sample throughput; and it offers great flexibility in varying pore size to target certain molecular size ranges. Using these self-assembled nanoarrays, we systematically studied the separation of 2–50-kbp DNA into different deflection angles with various pulsing conditions and pore sizes. DNA deflection showed a strong response to frequency and an unexpected peak in deflection angle vs frequency characteristics. The maximum deflection angle depended on molecular size. These

characteristics have not been reported previously. Our studies clearly point out the roadmap to achieve efficient separation for a given DNA size range in this type of matrix. More generally, the frequency response observed will require fundamental theoretical development of continuous-flow biomolecule separation using asymmetric pulsed fields in ordered arrays.

4.2 MATERIALS AND METHODS

4.2.1 Microchip Fabrication

PDMS microchips were fabricated using standard soft lithography as detailed in Chapter 2. Briefly, a high-resolution transparency mask was used to UV pattern AZ-4620 photoresist spun on 4-in. silicon wafers. The patterned photoresist masters were ~12 μm thick. The positive microstructures were replicated in PDMS pieces and six reservoirs were cut through the PDMS to access side microchannels. All devices were assembled by sealing PDMS replicas to clean glass slides without oxygen plasma oxidization and were used immediately for colloidal patterning.

4.2.2 Microfluidic Colloidal Self-Patterning

10% w/v aqueous suspensions of monodisperse silica colloids of 0.90 μm (Polysciences, Warrington, PA) and 330 nm (Bangs Laboratories, Fishers, IN) diameter were used. A 5–10-μL colloidal suspension was ultrasonicated for 10 min and injected into a buffer reservoir. The aqueous solution filled the microdevice spontaneously and stopped at the outlets of multiple evaporation channels. Solvent evaporation from the channel outlets induced colloidal crystallization to pack the device as illustrated in Figure

4-1. Colloidal suspensions in the reservoirs were then replaced with water, followed by the running buffer. Packed devices were allowed to dry out slowly by water evaporation through PDMS prior to optical and SEM characterization. For optical measurement, the whole packed PDMS devices were mounted onto a single cell holder for a 50-μL microcell in a DU800 UV/Vis spectrophotometer (Beckman Coulter, Fullerton, CA), with an empty device used as the blank. Colloidal arrays were exposed by peeling apart PDMS pieces, then coated with a thin gold film for SEM (LEO 1430, Zeiss, Germany).

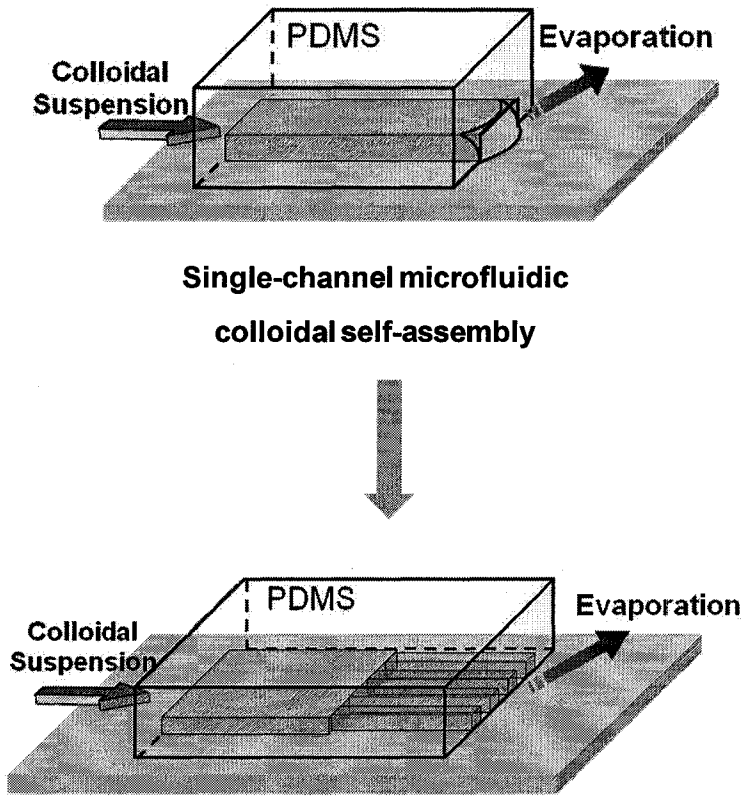

Figure 4-1. Schematic of large-scale microfluidic patterning of crack-free colloidal crystalline arrays within microdevices using multiple evaporation channels for in situ colloidal self-assembly.

4.2.3 Reagents and DNA Samples

All reagents and samples were prepared with deionized water (18.2 MΩ) obtained from an Ultrapure water system (Millipore, Milford, MA). 4× TBE buffer (356 mM Tris-borate, 8 mM EDTA, pH 8.3) was used to suppress electroosmotic flow in silica nanoarrays (10), with 4% v/v 2-mercaptoethanol added to reduce photobleaching. DNA fragments, including bacteriophage λ-DNA (New England Biolabs, Beverly, MA), NoLimits™ individual DNA of 2, 6, 10, 20 kbp (Fermentas Life Sciences, Burlington, ON), and λ-DNA/Hind III digest (Invitrogen, Burlington, ON), were stained by an intercalating fluorescent dye YOYO-1 (Molecular Probes) at the dye-to-base pair ratio of ~1:10. The final DNA concentration was 20–50 ng/μL for separation and 0.1 ng/μL for single-molecule imaging.

4.2.4 Separation and Fluorescence Imaging

Unless otherwise specified, separation was conducted in 330-nm colloidal nanoarrays. Pulsed electric fields were generated using homebuilt high-voltage amplifiers triggered by square wave signals from a synthesized function generator (Wavetek, San Diego, CA), and were applied to buffer reservoirs via platinum electrodes. The packed devices were pre-run at ~40 V/cm for 10 min. DNA molecules were excited with an expanded 488-nm argon ion laser beam, and the fluorescent emission was collected by a high-sensitivity CCD through a 505DRLP dichroic mirror and a 515-nm long-pass filter. A 4× objective (0.1 N.A., Olympus) was used for separation imaging and a plan-fluotar 100× oil-immersion objective (1.3 N.A., Leica, Germany) for single-molecule imaging. Digitized images were analyzed using ImageJ (NIH, Bethesda, MD).

4.3 RESULTS AND DISCUSSION

4.3.1 Large-scale Microfluidic Colloidal Patterning

The principle of self-assembly patterning in microfluidic chips is schematically illustrated in Figure 4-1. In our previous work [8], we established a single-microchannel CSA approach which uses evaporation-driven colloidal crystallization to pack the channel (Figure 4-1, top). In this approach, the drying front can be prevented from entering the packed bed, thus avoiding the cracks caused by bed shrinkage during drying. The capillary tension of the nanomenisci between close-packed spheres at the drying interface creates enormous negative capillary pressure that pulls water through the porous packed region, and maintains the evaporation front at the edge of the bed [28]. This microchannel confined self-assembly process allows us to pattern crack-free colloidal beds for separation applications.

Large crack-free colloidal structures are much more challenging to prepare than narrow 1D colloidal bands, because heterogeneous capillary stress built across large areas can cause severe film fracture during the evaporation-driven assembly. Slab fluidic cells, similar to microchannels but with much larger width (Figure 4-2A), have been commonly used to grow large size colloidal films [28-30]. Colloidal assembly within this type of constraint generates a pattern of cracks shortly after the start of evaporation from one end. As evident in Figure 4-2B, the cracks are spaced periodically along the evaporating edge and propagate parallel from the end into the bulk, while the compact bed remains water filled except in the cracks [28]. Different mechanisms have been proposed to explain the fracture pattern, but they reach the consensus that capillary stress is the driving force for fracturing, and that the period of cracks is set by the characteristic length

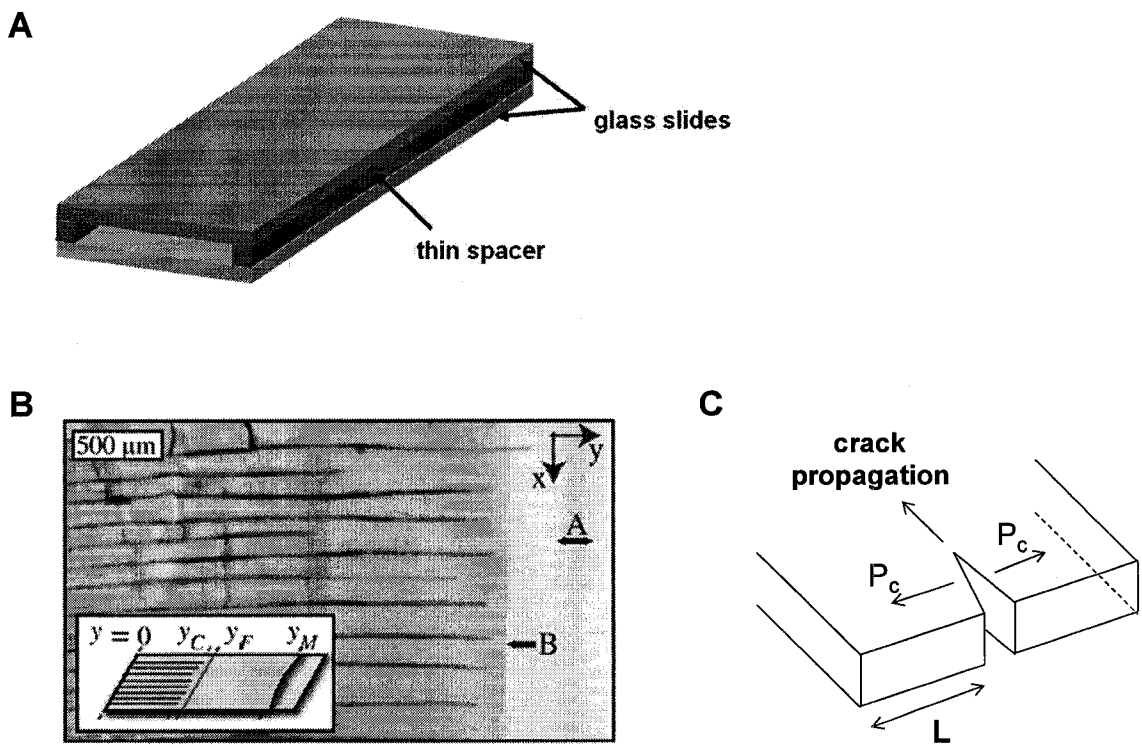

Figure 4-2. Evaporation-driven self-assembly of large-area colloidal crystalline arrays within fluidic cells. (A) Schematic of a typical fluidic cell assembly. (B) Bright-field photograph of the crack pattern in a drying suspension of silica nanoparticles within a fluidic cell (taken from [28], copyright by the American Physical Society). Inset is a schematic of the experimental geometry. The cracks start from the drying edge (y = 0) and the crack tips extend to y_C, just behind the compaction front, at y_F (pointed by label B in the image). (C) Illustration of a fracture mechanism proposed in [29]. Evaporation from the edge induces transverse capillary pressure P_c, which causes film fracturing. The opening of a crack relieves the stress along the drying edge over a characteristic distance L. Further evaporation increases P_c again, so that the crack tip keeps propagating towards the bulk.

of capillary stress variation along the drying edge, which reflects the balance between evaporation-induced capillary pressure and stress relaxation by crack opening [29, 31], as explained in Figure 4-2C. These discussions inspired us to use multiple parallel microchannels with appropriate width to guide the colloidal self-assembly within large-scale microdevices, as sketched in the bottom of Figure 4-1. The microchannels serve two functions: (A) they reduce the stress nonuniformity by separating wide open edges into segments shorter than the characteristic length scale above which cracking will occur; (B) microchannels prevent the drying front from penetrating into the bulk, thus avoiding cracks due to bead and contact volume shrinkage, as discussed in Chapter 2.

4.3.2 Device Fabrication and Characterization

Figure 4-3 presents a 2D microdevice for continuous sorting of DNA realized by this methodology. It consists of a 4×4 mm^2 square chamber connected to buffer and sample reservoirs via 20 parallel microchannels (100 μm×5 mm, 200-μm periodicity) on each side (Figure 4-3A). The channel width was chosen by considering experimental measurements of crack spacing performed with similar particle sizes and evaporation conditions [31, 32]. In addition, the microchannel arrays were designed to create fairly uniform electric fields over the large chamber [23]. Figure 4-3B shows that a PDMS device fully packed with 0.9-μm silica beads exhibits a spectrum of iridescent colors under white light illumination, which is due to Bragg scattering from the 3D periodic lattice. The bright-field micrograph of an as-prepared 330-nm silica nanoarray within a PDMS chip is shown in Figure 4-4A. The bed exhibits a uniformly translucent pattern which evidences the presence of interstitial water with no cracks in the colloidal array. A

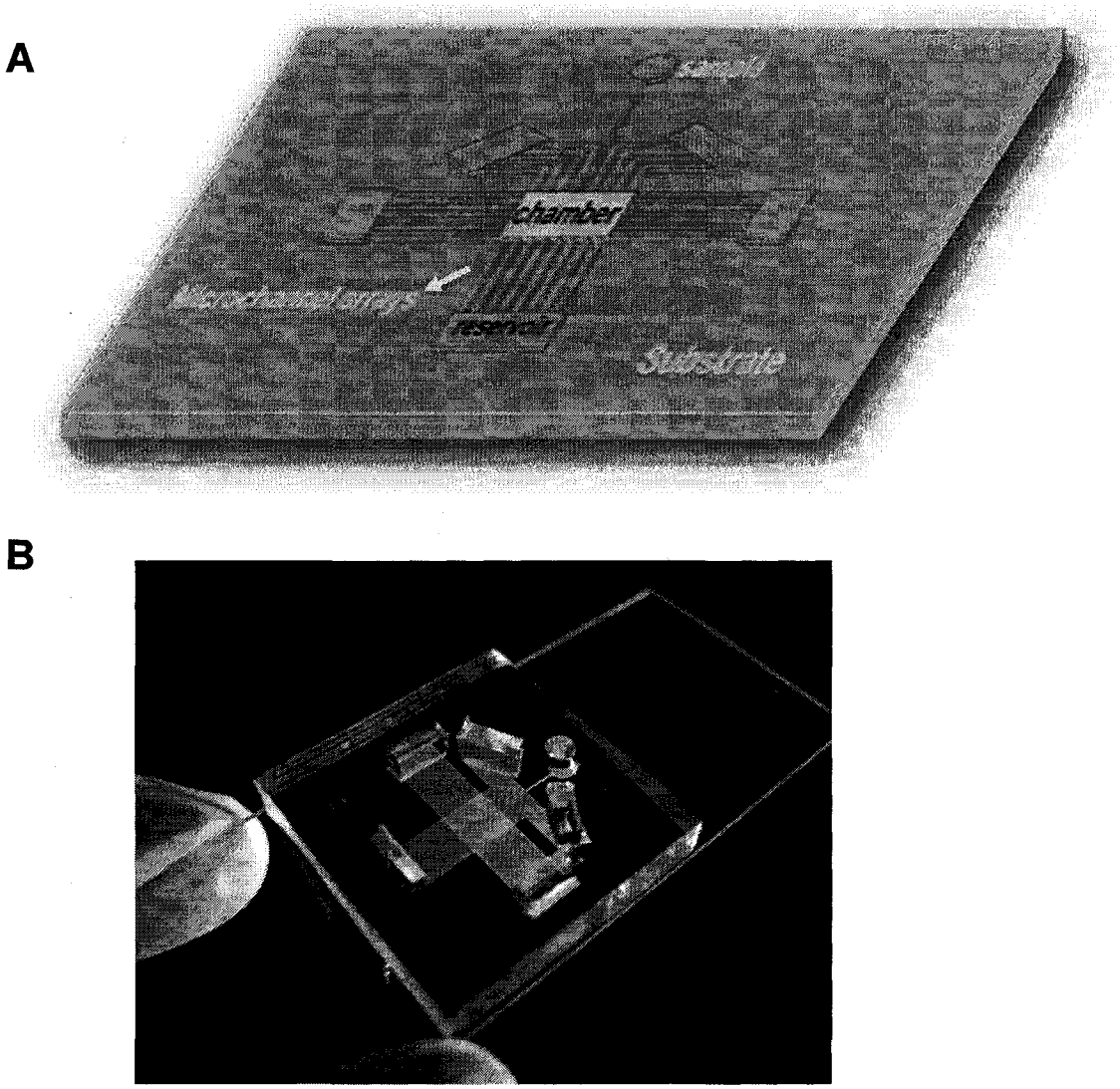

Figure 4-3. 2-D DNA microfractionator based on self-assembled crystalline nanoarrays. (A) Design of the device. It is composed of a 4×4 mm^2 square chamber connected to the reservoirs via 20 parallel microchannels (5 mm×100 μm, 200-μm periodicity) on each side. The photoresist mold was photopatterned on a silicon substrate. (B) Digital photograph of a PDMS chip packed with 0.9-μm silica spheres showing Bragg diffraction of light.

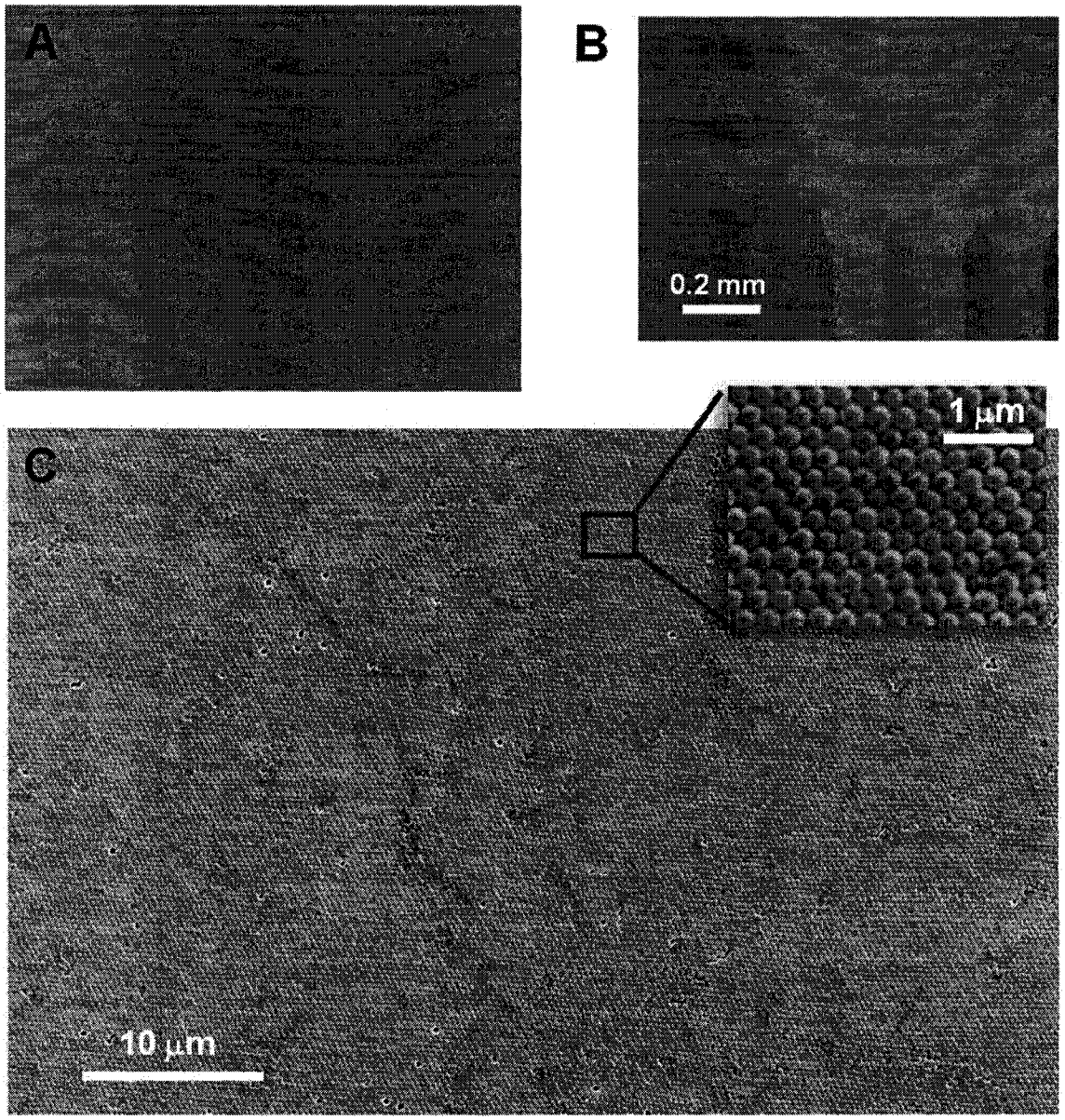

Figure 4-4. Characterization of self-assembled 330-nm silica crystalline nanoarrays. (A) Bright-field micrograph of an as-prepared wet silica nanoarray within a PDMS chip. (B) Optical microscope image of a dried bed obtained in reflection mode shows a red colour due to Bragg reflection from its 3D regular structure. (C) SEM images of large-area well-organized colloidal lattice at different magnifications.

patterned 330-nm silica array observed by optical microscopy exhibits a fairly uniform reddish color across a large area (Figure 4-4B), indicating the long-range lattice ordering. A typical scanning electron microscopy (SEM) image in Figure 4-4C reveals a large single crystal of composed of long-range ordered, close-packed 330-nm spheres, with the (111) plane parallel to the substrate. Cracks were observed in the sample, presumably arising from bed drying and peeling of the PDMS molds for SEM sample preparation. A low density of other defects was also seen, such as point voids and dislocation lines, which may affect the separation performance; but they are randomly distributed and localized so that no accumulative effects like flow channeling will arise.

We have also characterized the diffractive optical properties of the 330-nm colloidal nanoarray, as represented in Figure 4-5. The characteristic stop band observed corresponds to the first-order Bragg diffraction for the lattice dimension. The position of the peak maximum λ_{max} was determined to be 614.8 ± 4.5 nm for 9 devices including both freshly packed chips and those previously subjected to separation experiments. This value is slightly lower than the theoretical value estimated from the Bragg equation, but is consistent with the results reported in the literature for dried colloidal crystals prepared from silica colloids of the same size, presumably reflecting small shrinkage of dried colloids [33]. We obtained λ_{max} = 613.0 ± 2.8 nm for freshly prepared colloidal nanoarrays and λ_{max} = 617.0 ± 5.6 nm for the used ones. The small deviation of λ_{max} implies the structural stability of self-patterned nanoarrays that have been subjected to pulsed electric fields up to 170 V/cm.

The patterning approach presented here offers significantly greater assembly speed than conventional deposition techniques, which usually require tens of hours to

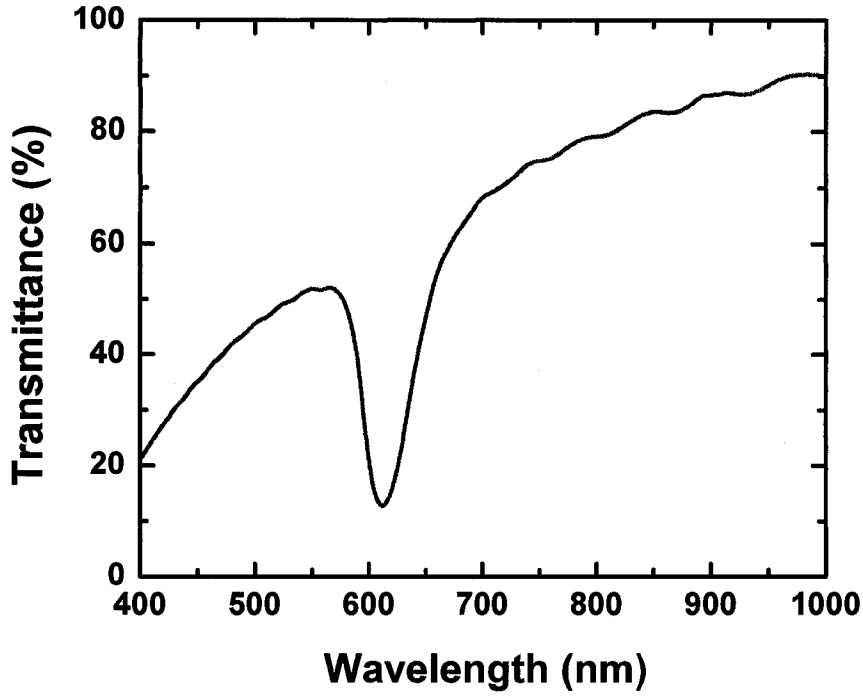

Figure 4-5. A typical normal incidence transmission spectrum obtained from a dried large-area 330-nm silica nanoarray.

days to obtain large colloidal films [12, 30]. It takes normally less than 3 hrs for 900-nm beads or 6 hrs for 330-nm beads (both are 10% w/v) to pack the microchannels and chamber (1.4 cm×1.4 cm total size) under ambient conditions. Compared to the design of a barrier structure with a gap size smaller than the particles to be trapped [12], our approach uses the air–liquid interface as a virtual frit to retain the microspheres, which offers the advantages of greatly simplified device fabrication as well as much larger evaporation area.

4.3.3 Generation of Pulsed Fields

Pulsed electric fields were generated by applying alternating high voltages to individual buffer reservoirs via platinum electrodes, as illustrated in Figure 4-6. The

microchannel arrays connected to the central chamber were designed as current injectors for creating fairly uniform electric fields over the large-area separation bed [23]. Two homebuilt high-voltage amplifiers were used to amplify the square wave signals generated by a synthesized function generator (Wavetek, San Diego, CA). The amplified voltage waveforms are in phase for the two output channels of each amplifier but 180° phase shifted between the two amplifiers (Figure 4-6A). The alternating high voltages were applied to individual buffer reservoirs via Pt electrodes, as arranged in Figure 4-6B, to generate ~135° pulsed fields ($E_1 = \sim 1.4E_2$) across the separation beds. Figure 4-7 demonstrates the visualization of long DNA molecules, which were linearized and undergoing ratcheting motion under obtuse-angle alternating electric fields. By tracking the motion of single DNA molecules, we measured the field angle to be 132.4 ± 4.3° (n = 72) in the central area of the separation chamber. We also monitored the waveforms of applied voltage and the current through the packed chips simultaneously using an oscilloscope. No phase shift between voltage and current were observed. Slightly rounded rising and falling edges of voltage square waves were observed, but the rise and fall times (from 10% to 90% of the full amplitude) were less than 5% of the period over the frequency range tested in this work (0.2–40 Hz).

4.3.4 Reorientation Mechanism

Continuous DNA separation is based on the biased reorientation mechanism, illustrated in Figure 4-8, which has been reported in microfabricated post arrays [23]. Briefly, asymmetric obtuse-angle pulsed fields are used to stretch and drive DNA chains to reorient periodically, with their head/tail repeatedly exchanged to lead the chain.

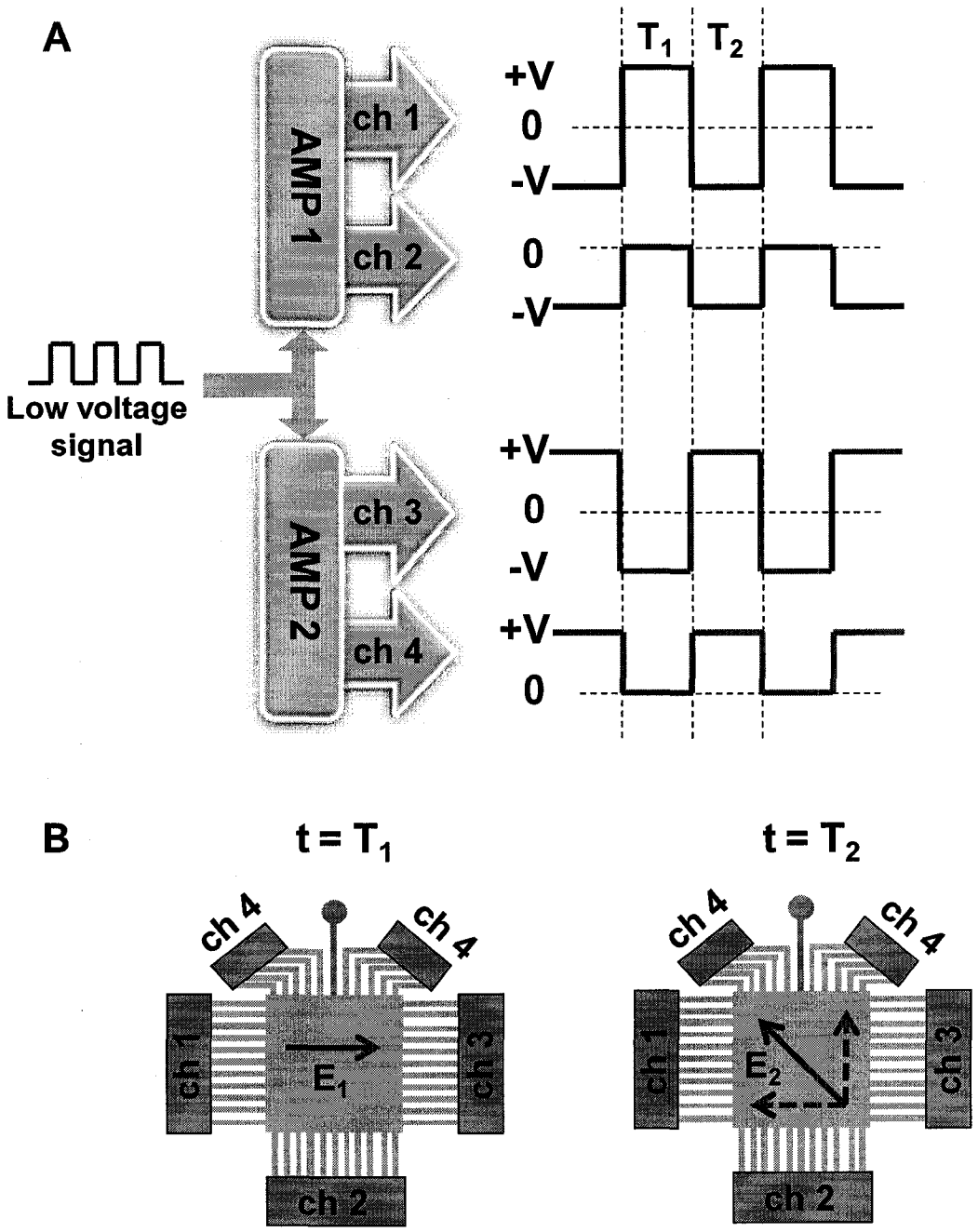

Figure 4-6. Generation of asymmetric obtuse-angle pulsed fields across the separation beds. (A) Amplification of low-voltage square wave signals (AMP: high voltage amplifier; ch: output channel). (B) The output high voltages were applied to individual buffer reservoirs of a 2D microdevice so that an asymmetric pulsed field ($E_1 = \sim 1.4E_2$) with ~135° alternating angle was generated across the separation bed.

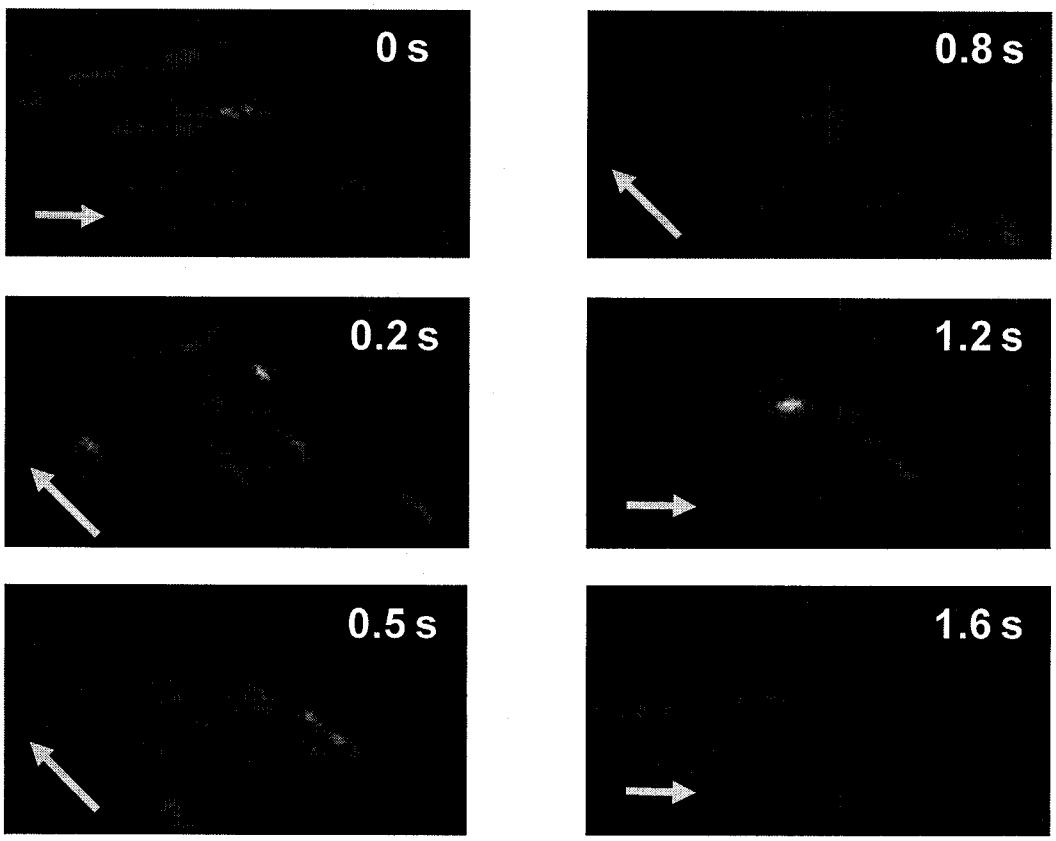

Figure 4-7. Time-elapsed sequence of false-color fluorescence images of the electromigration of single long DNA molecule in a 330-nm silica nanoarray under the asymmetric obtuse-angle pulsed field (E_1 = ~80 V/cm, f = 0.5 Hz). The arrows indicate the field directions.

Because DNA strands backtrack to different positions according to their sizes, the ratchet effect of the asymmetric electric pulses biases their net motion in different directions: the larger chain is deflected more from the average field direction than the small one.

Compared to a sparse array of microfabricated posts [34], the tight confinement in a crystalline array of closed-packed nanoparticles provides much stronger interaction with confined large DNA molecules, which remarkably complicates their electrophoretic dynamics [35]. To understand the deflection behavior observed, we start from a simplified model neglecting detailed molecular dynamics at first (Figure 4-8). Assuming a DNA chain has a uniform fractional extension l, three motion modes can be derived under asymmetric alternating electric fields (taking $E_1 > E_2$). First, when the pulsing frequency f is small, so that the migration distance along either field vector (in opposite direction) is longer than its own length, the DNA chain will proceed with a deflection angle given by (see Appendix for the derivation)

$$\tan\theta = \tan\alpha - \frac{d_2 - l}{d_1 - l}\sec\alpha, \qquad d_1 > d_2 > l \tag{4.1}$$

where α is the angle between the vector of E_1 and the injection direction; $d_1 = c\mu E_1/2f$, and $d_2 = c\mu E_2/2f$, the constant c accounts for the variation of the mobility μ during DNA alignment with the field [34]. In this mode, if f is very small so that $d_2 >> l$, θ becomes a constant θ_c independent of DNA size:

$$\tan\theta_c = \tan\alpha - (E_2/E_1)\sec\alpha \tag{4.2}$$

Second, as f increases, rendering $d_1 > l \geq d_2$ ($c\mu E_1/2l > f \geq c\mu E_2/2l$), the net DNA displacement only occurs along the stronger field E_1, since it cannot reorient completely by E_2. Thus the molecule moves with a maximum defection angle, $\theta_{max} = \alpha$. Third, when

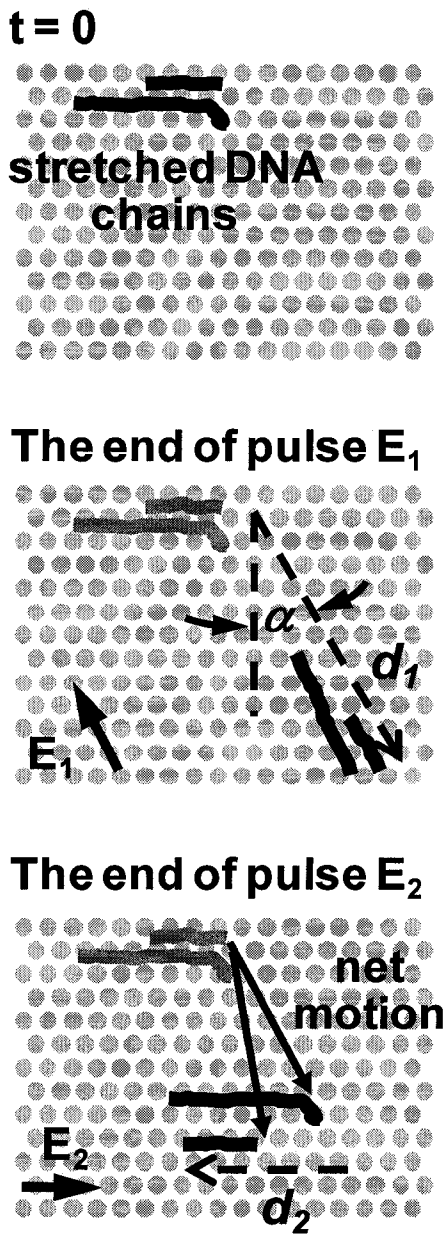

Figure 4-8. Schematic of biased reorientation mechanism under asymmetric obtuse-angle pulsed fields ($E_1 > E_2$). First, stretched DNA chains co-migrate a distance (d_1) against E_1, because of the size-independent mobility. As E_2 is switched on, DNA chains reorient at different spots according to length and back track a distance (d_2), led by their previous trailing ends. As a result, they show net motion with size-dependent direction.

$l \geq d_1 > d_2$ at $f \geq c\mu E_1/2l$, DNA does not have enough time to completely align with either field vector. Therefore, it will be dynamically trapped on a hook, moving back and forth. The discussion above provides a crude approximation, but sets up a framework leading to a more sophisticated understanding of the experimental results. It clearly suggests there will be minimum and maximum plateau regions for θ as a function of f, as depicted in Figure A-2 in Appendix.

4.3.5 Continuous DNA Fractionation

DNA size separations were performed in a continuous flow fashion: a DNA mixture is continuously injected into the packed chamber by a small constant negative voltage (12–20 volts) applied to the sample reservoir and will split into individual flow streams with different deflection angles, θ, which can be collected into downstream channels (Figure 4-9A). A clear separation of four DNA fragments of 2–20 kbp in a 330-nm nanoarray is demonstrated in Figure 4-9B–D. The fluorescence images show smooth, straight DNA streams without abrupt bending, indicating the absence of macroscopic lattice cracks that would cause flow channeling. Slightly smaller deflection angles were observed near the bottom edge than in the middle area of the bed (Figure 4-9C, D). This could be due to the field distortion near the edges and corners of the separation chamber, which may be further reduced by optimizing the chip design [36]. The continuous operation mode offers a high throughput for sample processing. The 3D nanopore arrays presented here further improve the sample capacity via easing the limitation of depth that is found with conventionally nanofabricated 2D structures.

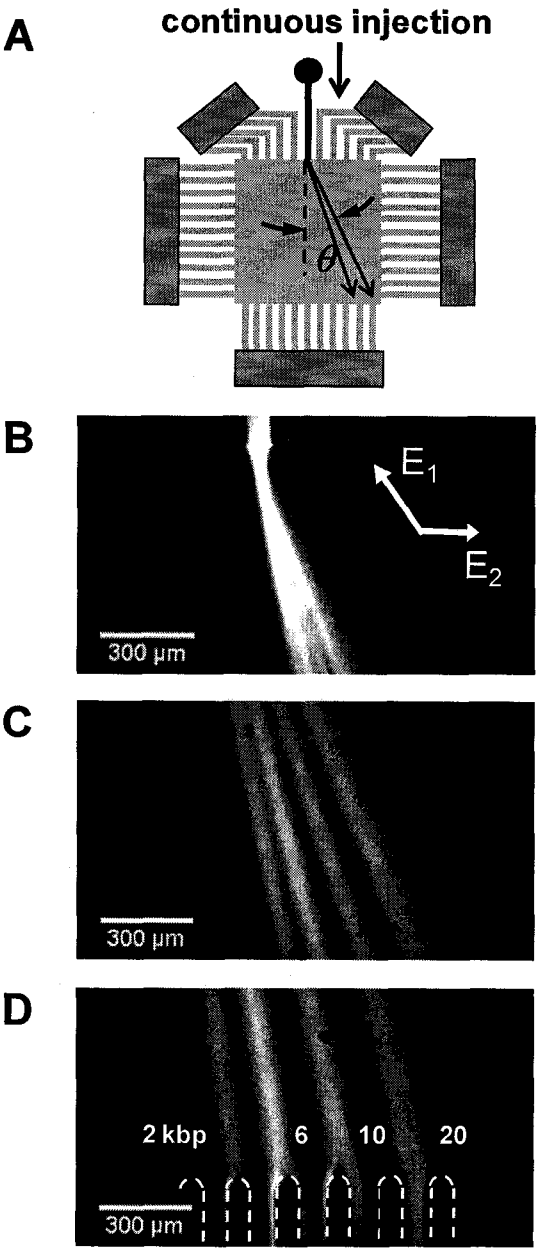

Figure 4-9. High-throughput DNA fractionation under pulsed fields. (A) Continuous separation based on angular deflection of DNA flow streams. θ is defined as the deflection angle between a DNA stream and the vertical injection direction. (B–D) Fluorescence images of sorting four DNA fragments of 2, 6, 10, and 20 kbp in a 330-nm silica nanoarray taken from the top, middle, and bottom of the chamber (E_1 = ~112 V/cm, f = 10 Hz), respectively. The concentration of 6-kbp DNA was spiked for easy identification of streams. The collecting channels in (D) were outlined for clarity.

Angular DNA separation has been shown to be strongly dependent on the pulsing conditions in a device called "DNA prism" [23]. However, there is a lack of clear guidance on how the conditions and separations are correlated. We systematically investigated the influence of molecule size and pulsing conditions on DNA deflection, as presented in Figure 4-10A–D. In the low-frequency regime ($f < 1$ Hz), no significant separation occurs and all DNA streams have a nearly constant angle of ~12°. But Equation 4.2 gives $\theta_c \approx 0°$, since $\alpha \approx 45°$ and $E_1 = \sim 1.4E_2$ in our case. This discrepancy may arise from the field strength-dependent DNA mobility observed in similar arrays [35]. We estimate θ_c should be 16° from Equation 4.1 by assuming the mobility increases linearly with the field strength, i.e. $\mu_1 = 1.4\mu_2$. In fact, if we consider $\mu_1 < 1.4\mu_2$ due to the effect of transition to a plateau in mobility under relatively high electric fields [35], slightly lower θ_c is expected, in reasonable agreement with the experimental results. The influence of the transient dynamics of the DNA chain is insignificant, since the distances involved are much longer than the DNA itself.

Following the initial low f plateau, the deflection angle rises as f increases. Size-based separation occurs in this regime. This is qualitatively expressed by Equation 4.1, from which one can derive that, as d_1 and d_2 gradually approach l, θ will augment and become dependent on DNA sizes (l). DNA fragments were seen reaching the maximum deflection regime at different frequencies–higher frequency for shorter DNA fragments or stronger electric fields except for the 2-kbp chain (Figure 4-10A–C), in accordance with the simplified model. In these two regimes, the electrophoretic dynamics of DNA, such as conformation changes, relaxation, and mobility variation [37], becomes

significant and should influence the onset frequency for separation and the magnitude of the deflection angles.

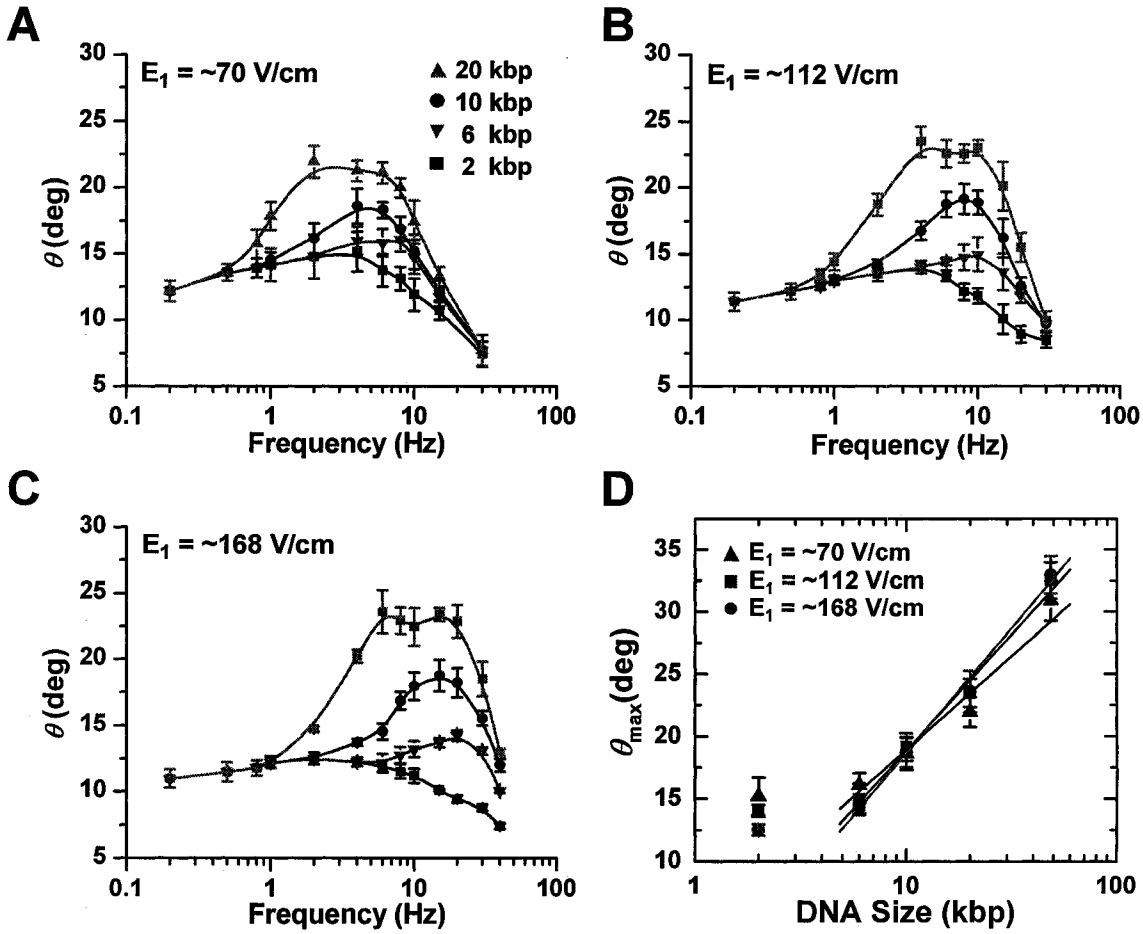

Figure 4-10. Effects of pulsing conditions on DNA deflection. (A–C) Frequency spectra of deflection angle θ for DNA of various molecular sizes under different field strength. Angles were measured from the middle of the separation chamber (as shown in Figure 4-9C) to minimize the effect of field distortion. Lines are drawn to guide the eye. (D) Semilog plot of θ_{max} against DNA molecular weight with least-squares linear fit. Error bars show standard deviations (n = 3).

A striking feature of the deflection behavior is the size dependence of θ_{max}. Figure 4-10D plots θ_{max} against DNA size over a size range up to 50 kbp, which clearly manifests that θ_{max} is a characteristic measure of the size for DNA larger than 6 kbp. This observation cannot be explained by the deterministic model of constant DNA length presented above, as it predicts a maximum angle θ_{max} = ~45°, regardless of DNA molecular weight. The stochastic fluctuation of DNA conformation and length should play a dominant role in the size dependence of θ_{max} [38]. Assume that a DNA chain reaches the maximum deflection at a given frequency, i.e. its extension $l = d_2$. In a cycle with positive fluctuation superimposed to its length at the end of pulse E_2 ($l + \Delta l > d_2$), the chain cannot complete the reorientation by E_2 and still drifts along the stronger field E_1. But a negative fluctuation ($l - \Delta l < d_2$) allows it to backtrack completely away from the sliding point at the end of pulse E_2, causing less deflection in this cycle. Figure 4-11A clearly displays the length fluctuation of a λ-DNA strand caused by dynamic conformation changes and the effects on its episodic motion in the maximum deflection regime (f = 4 Hz, E_1 = ~112 V/cm). The net motion of the molecule in frames 0–0.23s was only driven by the stronger field E_1 due to the previous incomplete reorientation, while hooking and the subsequent hernia development allowed the chain to shift along E_2, reducing the net deflection in this cycle (frames 0.33–0.57s). After many cycles, there should be an average θ_{max} that is smaller than α, the upper limit set by the field E_1. Therefore, θ_{max} reflects the extent of fluctuation of DNA strands.

Our results show that longer DNA has a larger θ_{max}, implying a lower relative fluctuation of longer DNA. The longitudinal fluctuation in the tube model has been proposed to account for the mechanism of pulsed-field gel electrophoresis [38], where the

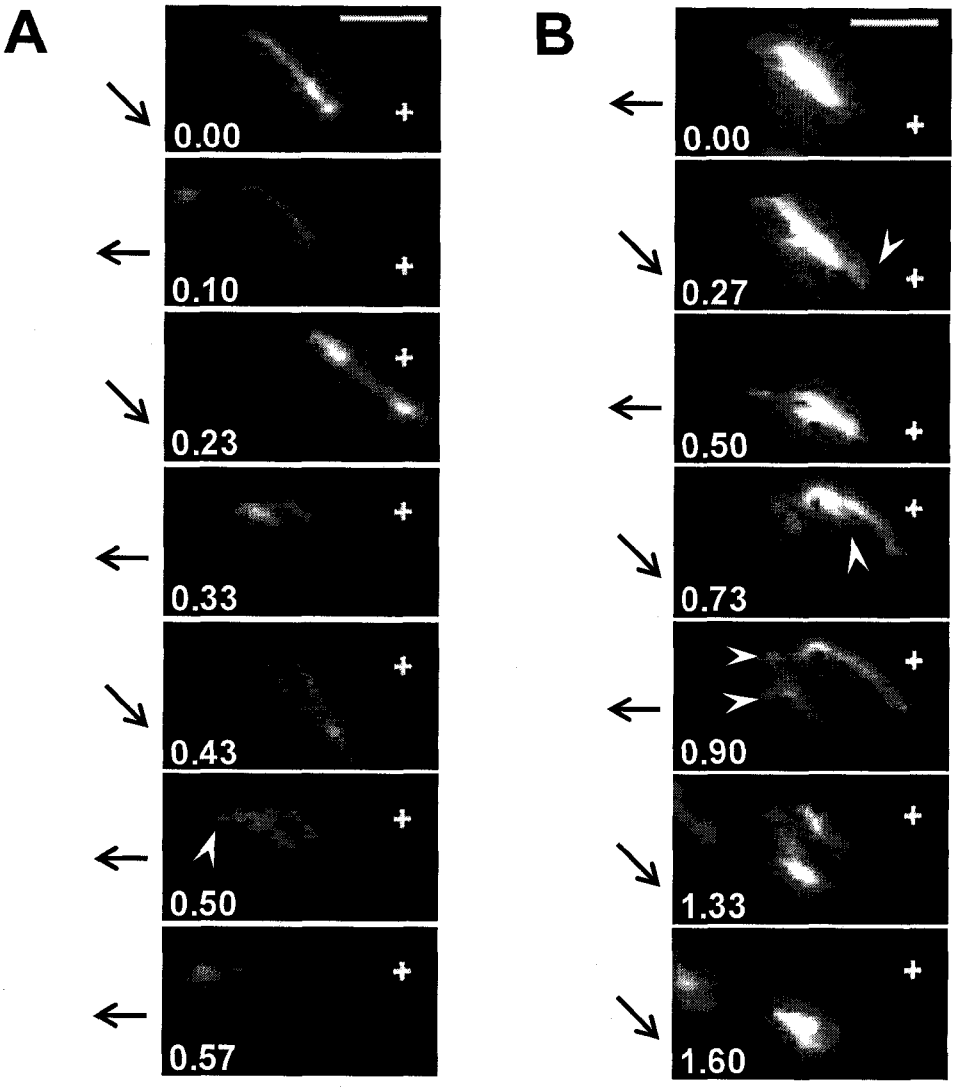

Figure 4-11. Sequences of fluorescence images of single λ-DNA migrating in a 330-nm bead array at frequencies of (A) 4 and (B) 10 Hz at E_1 = ~112 V/cm, respectively. Frames are time-stamped in seconds and superimposed with white cross signs as position references. Black arrows indicate the direction of electric force. White arrowheads point out the formation of hernias. Scale bars are 5 μm.

averaged relative fluctuation scales with molecular size N by $\Delta l / l \sim 1/\sqrt{N}$. This size scaling predicts smaller relative fluctuation for larger DNA, in qualitative agreement with our observations. Realistic DNA motion is more complicated than that described by the tube model, which neglects "tube leakage" [38], i.e. the formation of hernias, as seen in Figure 4-11A. Therefore the precise understanding of the size dependency of θ_{max} requires more quantitative analysis and numerical simulations to capture the transient dynamics of DNA molecules. Such an analysis is also crucial for studying the size selectivity and band dispersion of the continuous separation in crystalline arrays.

After the maximum deflection regime, the deflection angles decrease gradually with increasing f and DNA molecules were observed to drift at slower speeds, even at much higher frequencies. This falling regime is contrary to the dynamic trapping mode pictured by the simplified model. This regime might be mainly attributed to the formation of hernias [35]. As visualized in Figure 4-11B, DNA chains developed many hernias to escape dynamic trapping at a high frequency. The development of random hernias leads to complex conformations so that the molecule is poorly oriented with either field vector during backtracking. In effect, this suppresses the ratchet effect of asymmetric pulsed fields, which could account for the decrease of deflection angles.

We have noticed that 2-kbp DNA exhibits a distinctly different response to pulsing frequency (Figure 4-10A–C) compared to larger fragments, and its θ_{max} deviates qualitatively from the trend of larger DNA (Figure 4-10D). This discrepancy implies a change of separation mechanism with DNA size. The contour length of a 2-kbp dsDNA is ~680 nm, spanning only two spheres of 330 nm diameter. Taking into account the partial extension and fast relaxation of short DNA, it is more likely for 2-kbp DNA to

reptate along a zigzag path without periodic exchange of the leading head [34, 38], in contrast to the characteristic chevron pattern with head switching in the reorientation mechanism. This indicates the effect of lattice dimension on the lower size limit of efficient separation. Figure 4-10D suggests the mechanism transition occurs near 6 kbp in this 330-nm colloidal array.

4.3.6 Separation Performance

Figure 4-10 shows that efficient separation occurs in the regime of rising deflection angles and that size selectivity can be fine tuned by adjusting the pulsing frequency. In this regime, the electrophoretic dynamics of DNA, such as chain relaxation, significantly affects the instant DNA length at the end of each pulse. It was observed that long DNA molecules are highly stretched during reorientation, after which the newly released chains relax back to a more contracted state. DNA relaxation can be characterized by a time constant scaled with the molecular size N as $\tau \sim N^2$ [39, 40]. Therefore, in addition to controlling the time for electromigration, pulsing frequency also affects the separation in terms of the dynamic time scales of DNA relaxation. One can speculate that, at a given frequency, DNA chains having τ longer than the pulse duration remain in an extended state, while the fast relaxation of smaller ones will diminish their size differences. Relaxation thus favours the isolation of long DNA from short. Figure 4-12A images selective separation of the largest 20-kbp fragment from a mixture by tuning f from 2 to 4 Hz at E_1 = ~168 V/cm. Sufficient size selectivity for smaller fragments can be obtained at a higher f of 15 Hz. The resolution R_s can be calculated from the fluorescence intensity profile (Figure 4-12B) using $R_s = \Delta x/2(\sigma_1 + \sigma_2)$, where

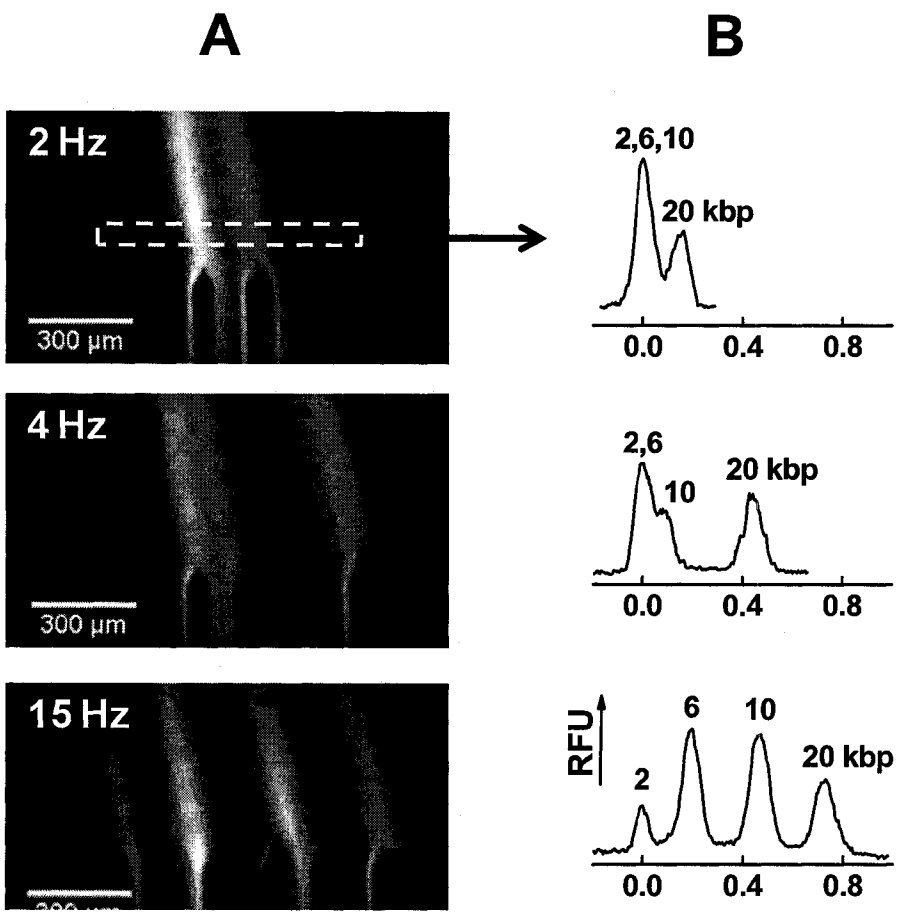

Figure 4-12. Effects of pulsed field on separation performance. (A) Fluorescence images taken at the bottom of the chamber show the separations of 2–20 kbp DNA at different frequencies and E_1 = ~168 V/cm. (B) The intensity profiles were obtained by scanning above the collecting channels, as indicated by the box. The centre of the 2-kbp peak (or co-migration peak) was defined as the origin of the horizontal axis of the separation distance.

Δx is the peak separation, and σ_1 and σ_2 are the standard deviations (s.d.) of the adjacent peaks, all from Gaussian fitting [41]. For the separation obtained at f = 15 Hz, R_s is higher than 2.0 for two adjacent DNA streams. Such improvement comes at the cost of resolution for the largest two fragments, because 20-kbp DNA has reached its maximum deflection.

To evaluate the effect of field strength on separation efficiency, we compare the separations that yield the highest peak capacities $n_{c,\,max}$ between 2 and 20 kbp at different field strengths. The peak capacity n_c defines the number of streams that can be separated at a given R_s for adjacent streams over the space L provided by the separation method: $n_c = L / (4\bar{\sigma} R_s)$, where $\bar{\sigma}$ denotes the mean of the standard deviation (s.d.) of stream widths [41]. From all the pulsing conditions tested in Figure 4-10, we determined $n_{c,\,max} = 4$ at f = 6 Hz for E_1 = ~70 V/cm, $n_{c,\,max} = 7$ at f = 10 Hz for E_1 = ~112 V/cm, and $n_{c,\,max} = 8$ at f = 15 Hz for E_1 = ~168 V/cm, with $R_s = 1$ and $L = \Delta x + 2\bar{\sigma}$. Those separations are plotted in Figure 4-13. It is seen that better separation across the size range of 2 and 20 kbp can be achieved under higher field strength, and the improvement is mainly in the range of 2–10 kbp. This could be attributed to the fact that the extent of DNA electrophoretic stretching is molecular length dependent [42, 43]. High field strength is desired for better stretching of short DNA and the corresponding high frequency favors the separation of short DNA as well, by shortening the relaxation time.

Physical confinement profoundly affects the molecular dynamics of DNA. Lithographically fabricated nanochannels have been used to efficiently stretch DNA chains by the excluded-volume effect [39, 40]. Nanofluidic channels also improve the efficiency of electrophoretic stretching and slow down the relaxation of confined DNA

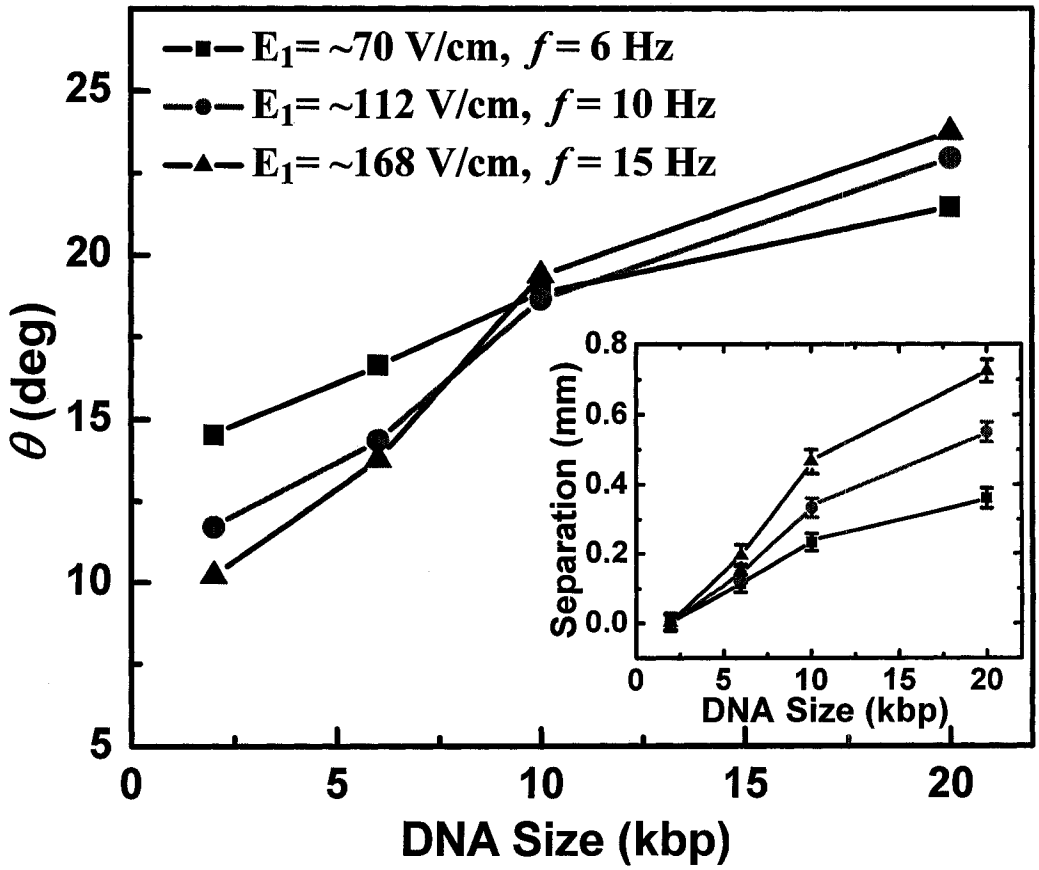

Figure 4-13. Plots of θ and separation distance (inset) obtained in three separations as a function of molecular weight. For each field strength, frequency was chosen to give the highest peak capacity between 2 and 20 kbp. The fluorescence intensity profiles obtained as in Figure 4-12B were fitted with Gaussian function to determine the separation distance between DNA fragments. Error bars are ±s.d. of the peaks.

molecules [43]. Such effects are fundamentally important for improving separation in pulsed-field electrophoresis techniques. Close-packed nanobeads in crystalline arrays define the molecular-sized porous constraint with pores of ~15% the bead size. Figure 4-14 demonstrates the impact of nanopore confinement on the angular separation. With mild pulsing conditions, separation of λ-DNA/Hind III digests only occurs between the largest two fragments using 900-nm beads, while all but 2 and 2.3 kbp are resolved in a

330-nm nanoarray having ~50-nm pores. This result indicates the flexibility of this self-assembly approach in controlling pore size to adjust the separation power for DNA species of interest. Such flexibility is especially desirable for applications such as sequencing short single-stranded DNA [34], which is performed on a length scale still challenging for conventional nanofabrication techniques to access, such as ~10 nm.

4.4 CONCLUSIONS

We have demonstrated a general microfluidic approach for patterning large-scale colloidal nanoarrays into microdevices, which presents two major merits: first, the use of multiple evaporation microchannels avoids the formation of drying-induced cracks during colloidal crystallization; second, the method features simple microfabrication, fast colloidal deposition, and extremely low cost. Using the technique, we fabricated a 2D microsystem for high-throughput separation of 2–50 kbp DNA. The effects of pulsed electric field and pore size on the separation have been systematically studied. Our results present clear guidance for choosing proper field conditions to sort DNA samples of interest. Self-assembled colloidal arrays may provide an ideal system for understanding mechanisms underlying biomolecular separation in porous media, due to the well-ordered, well-defined structure. Being compatible with inexpensive soft lithography processing, this approach may hold the potential of commercialization for mass production of disposable ordered array-based separation devices.

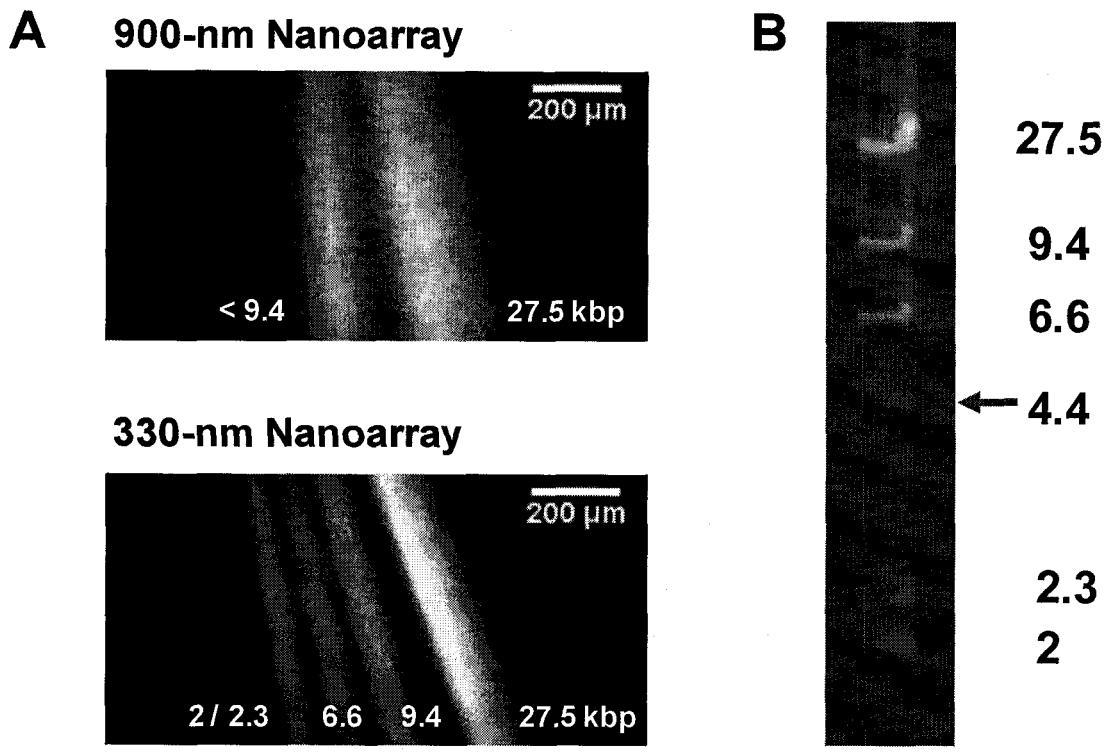

Figure 4-14. Effect of spatial confinement (pore size) on separation resolution. (A) Separation of λ-DNA/Hind III digests in the colloidal nanoarrays composed of 900-nm and 330-nm silica beads (E_1 = ~84 V/cm, f = 5 Hz). λ-DNA/Hind III sample was used without heat pretreatment. (B) Gel electrophoresis of the same DNA mixture in 1% agarose gel. The arrow points out a very faint band of 4.4-kbp fragment, confirming that the majority of this fragment has annealed with 23.1-kbp fragment to form 27.5-kbp fragment. The numbers label the molecular sizes of the separated band of λ-DNA/Hind III digests.

4.5 REFERENCES

1 Whitesides, G. M.; Grzybowski, B. *Science* **2002**, *295*, 2418-2421.

2 Xia, Y. N.; Gates, B.; Yin, Y. D.; Lu, Y. *Adv. Mater.* **2000**, *12*, 693-713.

3 Mezzenga, R.; Ruokolainen, J.; Fredrickson, G. H.; Kramer, E. J.; Moses, D.; Heeger, A. J.; Ikkala, O. *Science* **2003**, *299*, 1872-1874.

4 Blanco, A.; Chomski, E.; Grabtchak, S.; Ibisate, M.; John, S.; Leonard, S. W.; Lopez, C.; Meseguer, F.; Miguez, H.; Mondia, J. P.; Ozin, G. A.; Toader, O.; van Driel, H. M. *Nature* **2000**, *405*, 437-440.

5 Vlasov, Y. A.; Bo, X. Z.; Sturm, J. C.; Norris, D. J. *Nature* **2001**, *414*, 289-293.

6 Ben-Moshe, M.; Alexeev, V. L.; Asher, S. A. *Anal. Chem.* **2006**, *78*, 5149-5157.

7 Zheng, S. P.; Ross, E.; Legg, M. A.; Wirth, M. J. *J. Am. Chem. Soc.* **2006**, *128*, 9016-9017.

8 Zeng, Y.; Harrison, D. J. *Anal. Chem.* **2007**, *79*, 2289-2295.

9 Jin, C. J.; McLachlan, M. A.; McComb, D. W.; De La Rue, R. M.; Johnson, N. P. *Nano Lett.* **2005**, *5*, 2646-2650.

10 Wong, S.; Kitaev, V.; Ozin, G. A. *J. Am. Chem. Soc.* **2003**, *125*, 15589-15598.

11 Burkert, K.; Neumann, T.; Wang, J. J.; Jonas, U.; Knoll, W.; Ottleben, H. *Langmuir* **2007**, *23*, 3478-3484.

12 Mayers, B. T.; Gates, B.; Xia, Y. N. *Adv. Mater.* **2000**, *12*, 1629-1632.

13 Yang, S. M.; Miguez, H.; Ozin, G. A. *Adv. Funct. Mater.* **2002**, *12*, 425-431.

14 Shiu, J. Y.; Kuo, C. W.; Chen, P. L. *J. Am. Chem. Soc.* **2004**, *126*, 8096-8097.

15 Yan, X.; Yao, J. M.; Lu, G. A.; Chen, X.; Zhang, K.; Yang, B. *J. Am. Chem. Soc.* **2004**, *126*, 10510-10511.

16 Hayward, R. C.; Saville, D. A.; Aksay, I. A. *Nature* **2000**, *404*, 56-59.

17 Masuda, Y.; Itoh, T.; Koumoto, K. *Langmuir* **2005**, *21*, 4478-4481.

18 Volkmuth, W. D.; Austin, R. H. *Nature* **1992**, *358*, 600-602.

19 Chou, C. F.; Bakajin, O.; Turner, S. W. P.; Duke, T. A. J.; Chan, S. S.; Cox, E. C.; Craighead, H. G.; Austin, R. H. *Proc. Natl. Acad. Sci. U.S.A.* **1999**, *96*, 13762-13765.

20 Han, J.; Turner, S. W.; Craighead, H. G. *Phys. Rev. Lett.* **1999**, *83*, 1688-1691.

21 Han, J.; Craighead, H. G. *Science* **2000**, *288*, 1026-1029.

22 Bakajin, O.; Duke, T. A. J.; Tegenfeldt, J.; Chou, C. F.; Chan, S. S.; Austin, R. H.; Cox, E. C. *Anal. Chem.* **2001**, *73*, 6053-6056.

23 Huang, L. R.; Tegenfeldt, J. O.; Kraeft, J. J.; Sturm, J. C.; Austin, R. H.; Cox, E. C. *Nat. Biotechnol.* **2002**, *20*, 1048-1051.

24 Kaji, N.; Tezuka, Y.; Takamura, Y.; Ueda, M.; Nishimoto, T.; Nakanishi, H.; Horiike, Y.; Baba, Y. *Anal. Chem.* **2004**, *76*, 15-22.

25 Huang, L. R.; Cox, E. C.; Austin, R. H.; Sturm, J. C. *Science* **2004**, *304*, 987-990.

26 Fu, J. P.; Yoo, J.; Han, J. Y. *Phys. Rev. Lett.* **2006**, *97*, 018103.

27 Fu, J. P.; Schoch, R. B.; Stevens, A. L.; Tannenbaum, S. R.; Han, J. Y. *Nat. Nanotechnol.* **2007**, *2*, 121-128.

28 Dufresne, E. R.; Corwin, E. I.; Greenblatt, N. A.; Ashmore, J.; Wang, D. Y.; Dinsmore, A. D.; Cheng, J. X.; Xie, X. S.; Hutchinson, J. W.; Weitz, D. A. *Phys. Rev. Lett.* **2003**, *91*, 224501.

29 Allain, C.; Limat, L. *Phys. Rev. Lett.* **1995**, *74*, 2981-2984.

30 Ishii, M.; Nakamura, H.; Nakano, H.; Tsukigase, A.; Harada, M. *Langmuir* **2005**, *21*, 5367-5371.

31 Lee, W. P.; Routh, A. F. *Langmuir* **2004**, *20*, 9885-9888.

32 Li, H. L.; Dong, W. T.; Bongard, H. J.; Marlow, F. *J. Phys. Chem. B* **2005**, *109*, 9939-9945.

33 Brozell, A. M.; Muha, M. A.; Parikh, A. N. *Langmuir* **2005**, *21*, 11588-11591.

34 Duke, T. A. J.; Austin, R. H.; Cox, E. C.; Chan, S. S. *Electrophoresis* **1996**, *17*, 1075-1079.

35 Zhang, H.; Wirth, M. J. *Anal. Chem.* **2005**, *77*, 1237-1242.

36 Huang, L. R.; Tegenfeldt, J. O.; Kraeft, J. J.; Sturm, J. C.; Austin, R. H.; Cox, E. C. *Tech. Dig. Int. Elect. Dev. Mtg.* **2002**, 363-366.

37 Viovy, J. L. *Rev. Mod. Phys.* **2000**, *72*, 813-872.

38 Viovy, J. L. *Electrophoresis* **1989**, *10*, 429-441.

39 Reisner, W.; Morton, K. J.; Riehn, R.; Wang, Y. M.; Yu, Z. N.; Rosen, M.; Sturm, J. C.; Chou, S. Y.; Frey, E.; Austin, R. H. *Phys. Rev. Lett.* **2005**, *94*, 196101.

40 Tegenfeldt, J. O.; Prinz, C.; Cao, H.; Chou, S.; Reisner, W. W.; Riehn, R.; Wang, Y. M.; Cox, E. C.; Sturm, J. C.; Silberzan, P.; Austin, R. H. *Proc. Natl. Acad. Sci. U.S.A.* **2004**, *101*, 10979-10983.

41 Giddings, J. C. *Unified Separation Science*; Wiley: New York, 1991.

42 Marko, J. F.; Siggia, E. D. *Macromolecules* **1995**, *28*, 8759-8770.

43 Bakajin, O. B.; Duke, T. A. J.; Chou, C. F.; Chan, S. S.; Austin, R. H.; Cox, E. C. *Phys. Rev. Lett.* **1998**, *80*, 2737-2740.

Chapter 5

Confinement Effects on Electromigration of Long DNA Molecules in an Ordered Cavity Array*

5.1 INTRODUCTION

Electrophoresis is a major technique for separation of DNA and other polyelectrolytes, in which separation relies on the interactions between polymer molecules and the sieving matrices [1]. The confinement effects imposed by sieving structures play an important role in achieving size-dependent electrophoretic separation of charged polyelectrolytes and have been well studied in DNA gel electrophoresis. Unfortunately, separation of large DNA molecules longer than 40 kilobase pair (kbp) is a long-standing challenge in gel electrophoresis because of the loss of dependence of mobility on molecular size when long DNA chains reptate within the gel fibers. During the past decade, efforts have shifted to exploring new artificial sieving structures, which could provide novel constrained environments to modify the dynamics of trapped macromolecules [2-14]. Probing such confinement has led to several interesting mechanisms for size fractionation of large DNA molecules, including entropic trapping [3, 4], entropic recoil [5], Brownian diffusion ratchets [6], and laminar flow bifurcation [7]. Herein, we report the experimental evaluation of confinement effects on the

* A version of this chapter has been published. Zeng, Y.; Harrison, D. J. *Electrophoresis*, **2006**, *27*, 3747–3752.

electromigration of long DNA molecules within a microporous array, composed of well-ordered cavities interconnected by nanopores. The cavity array was fabricated by replicating the structure of a colloidal crystal of beads in a polymer matrix. The electrophoresis of confined DNA molecules demonstrates an unusual mobility as a function of molecular weight and electric field, as a result of the combination of the unique geometry and conductivity of this sieving material. To our knowledge, this observation is distinct from that discovered in both gels and microfabricated sieves.

Artificial sieving structures are normally made through micro- and nano-fabrication techniques that can offer good control of size and geometry [2-8]. The use of regular and well characterized topologies makes it possible to clearly understand the molecular transport of confined polymer molecules [3, 6, 7]. The assembly of colloidal particle arrays provides a promising alternative to micro- and nanofabrication, in terms of readily scaling to pore sizes of tens of nanometers, and for fabrication of unique geometries, which are still challenging for current techniques [10-15]. A highly ordered microporous material, for instance, has been fabricated by replicating the structure of a self-assembled colloidal monolayer [15]. Macromolecular diffusion in this assembly of cavities interconnected by nanopores was studied by visually monitoring Brownian motion of individual DNA molecules. The effect of these novel structures on the electric field driven migration of large DNA molecules has not been reported.

5.2 MATERIALS AND METHODS

5.2.1 Reagents and Samples

All reagents and samples were prepared with deionized water (18.2 MΩ) obtained

from an Ultrapure water system (Millipore, Milford, MA). Acrylamide monomer, bis-acrylamide crosslinker, ammonium persulfate, and N,N,N',N'-tetramethylethylenediamine (TEMED) were all received from Bio-Rad. 10× Tris-borate-EDTA buffer (TBE), 2-mercaptoethanol, glucose, glucose oxidase, and catalase were obtained from Sigma (St. Louis, MO). 10% aqueous suspension of 1-μm diameter, negatively charged polystyrene beads was used here (3 % size deviation, IDC, Portland, Oregon). The original suspension was diluted to 0.15% and then ultrasonicated for 10 min prior to use. Calf thymus DNA (13 kbp) and bacteriophage λ-DNA (48.5 kbp) were obtained from Sigma (St. Louis, MO). Intercalating fluorescent dye YOYO-1 (Molecular Probes, Eugene, OR) was used to stain DNA samples at the dye-to-base pair ratio of ~1:5 in 0.5× TBE buffer (44.5 mM Tris-borate, 1 mM EDTA, pH 8.0) containing 4% 2-mercaptoethanol, ~2.3 mg/mL glucose, ~0.1 mg/mL glucose oxidase, ~0.018 mg/mL catalase (all from Sigma) to reduce the photobleaching and photocleavage. Stained DNA solution was diluted to the final concentration of 0.01–0.05 ng/μL. YOYO-1 intercalating dye is a potential mutagen, and 2-mercaptoethanol is toxic; gloves should be worn when the solutions are handled.

5.2.2 Colloidal Self-Assembly

A vertical deposition approach was adopted to fabricate a strip of colloidal array on a glass substrate [16], as illustrated in Figure 5-1. Briefly, a glass slide was cleaned in hot Piranha solution (3:1 mixture of sulfuric acid and 30% hydrogen peroxide) for 15 min, rinsed with copious water, and followed by drying in nitrogen gas flow. The cleaned substrate was immersed vertically in a glass vial containing 0.15% aqueous

suspension of negatively charged polystyrene beads of 1 μm in diameter. The vial was put on a leveled optical table and protected from dust by partially covering with a large glass dish. The assembly was left under ambient conditions to allow slow solvent evaporation for colloidal deposition on the surface of the substrate. Upon growing to the desired size, the colloidal film was taken out of the vial and subjected to drying in air for one hour.

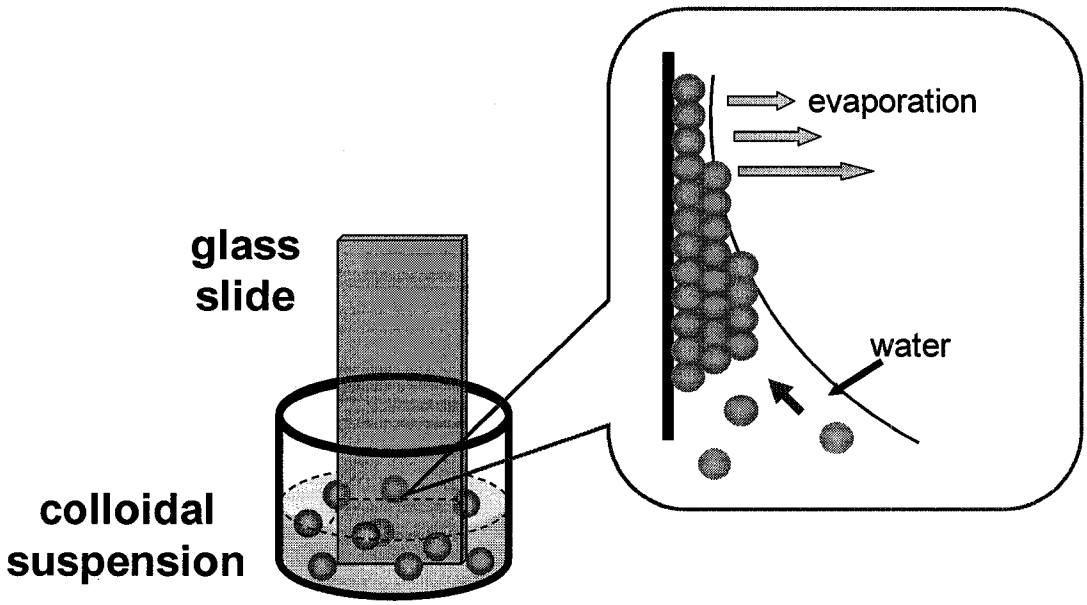

Figure 5-1. Schematic diagram of vertical deposition method utilizing evaporation-induced colloidal self-assembly driven by capillary forces. As sketched in the expanded view, water evaporation induces water flux towards the thin liquid film, carrying the suspended particles to the contact line, drawn as a dashed line on the glass slide, where they are assembled into a closed-packed array by the lateral capillary force between them. As the entire bath surface recedes, a large-area crystalline lattice of fine particles is grown along the substrate.

5.2.3 Colloidal Templating

The fabrication of ordered porous hydrogel using a colloidal crystal as the template is schematically sketched in Figure 5-2. The dried crystalline lattice was infiltrated with a 30% aqueous acrylamide monomer solution containing 6% bis-acrylamide crosslinker, 1% ammonium persulfate, and small amount of the photoinitiator TEMED by capillary force. After the completion of polymerization, the crystalline array of closed-packed beads was immobilized in a slab of dense polyacrylamide gel, which was then peeled off the glass substrate and soaked in toluene overnight to dissolve PS particles away. Left behind is a dense hydrogel embedded with a cavity array composed of close-packed voids interconnected to each other by circular pores of ~ 200 nm in diameter [15], as sketched in the bottom of Figure 5-2. The gel slabs were then rinsed with methanol and water a few times and stored in water for use.

5.2.4 DNA Electrophoresis and Fluorescence Imaging

Prior to electrophoresis experiments, the gel slab was equilibrated in 0.5× TBE running buffer (pH = 8.0) containing 4% 2-mercaptoethanol, ~2.3 mg/mL glucose, ~0.1 mg/mL glucose oxidase, and ~0.018 mg/mL catalase to reduce the photobleaching and photocleavage during laser-induced fluorescence imaging. The slab was cut open at both ends of the cavity array to provide fluid access and fit into a glass electrophoresis cell, as sketched in Figure 5-3. The electrophoresis cell was partially covered with a cover plate to reduce water evaporation and filled with the running buffer. The gel was pre-run for 10 min at ~10 V/cm electric field and DNA samples were added to the anodic side of the cell.

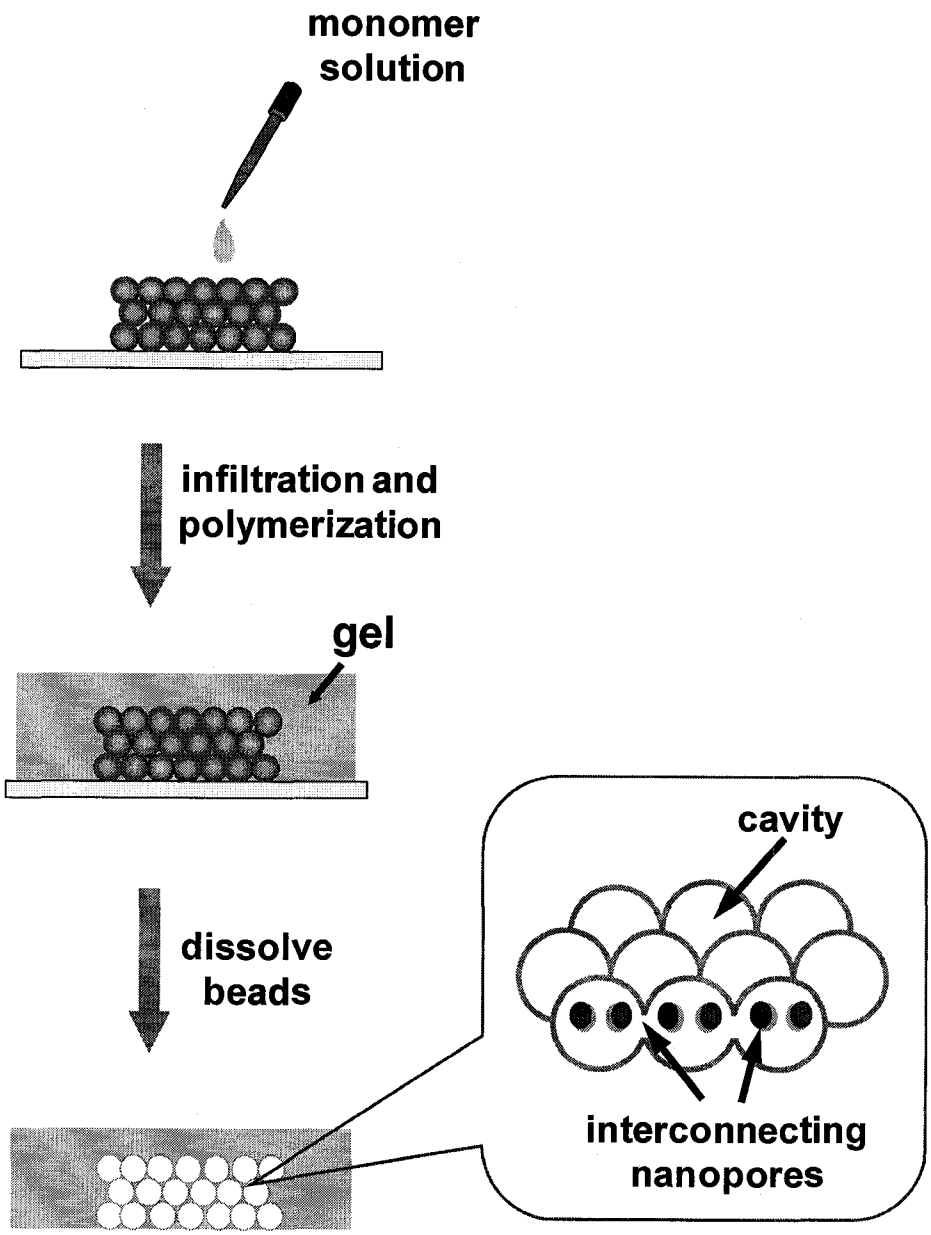

Figure 5-2. Schematic diagram of fabrication of a hexagonally ordered three-dimensional cavity array embedded in a dense hydrogel slab by the approach of colloidal templating.

Epifluorescence videomicroscopy was used to probe single DNA molecules stained by YOYO-1 (Molecular Probe), as shown in Figure 5-3. Samples were excited with an expanded 488-nm argon ion laser beam, and the fluorescent emission was collected with a homemade inverted microscope equipped with a 505DRLP dichroic mirror, 515-nm long-pass filter, and a 40× planachromat objective (0.6 N.A., LDN, Carl Zeiss) and a high-sensitivity CCD (AVA Astrovid, Stellacam). Captured videos were recorded to VHS tapes and digitized to computer format at 30 frames per second. Digitized videos were then analyzed using ImageJ (NIH, Bethesda, MD, http://rsb.info.nih.gov/ij/).

5.3 RESULTS AND DISCUSSION

5.3.1 Convective Colloidal Self-Assembly

In the vertical deposition method utilizing evaporation-induced colloidal self-assembly, the quality of colloidal crystals is largely affected by the deposition conditions, including colloidal volume fraction, evaporation temperature, relative humidity, solvent, and particle diameter [16-19]. It has been reported that the evaporation temperature during vertical deposition is a significant parameter in controlling the crystalline quality. An elevated evaporation temperature augments the solvent evaporation rate which leads to the hydrodynamic influx pressure at the drying front. It also increases the kinetic energy for the particles exploring possible energetically favourable lattice sites. All these factors contribute to the better crystalline quality in terms of larger domain size and less lattice defects [18]. However, this process requires precise control of the temperature of the colloidal suspension and it has proved difficult to achieve reproducible production of

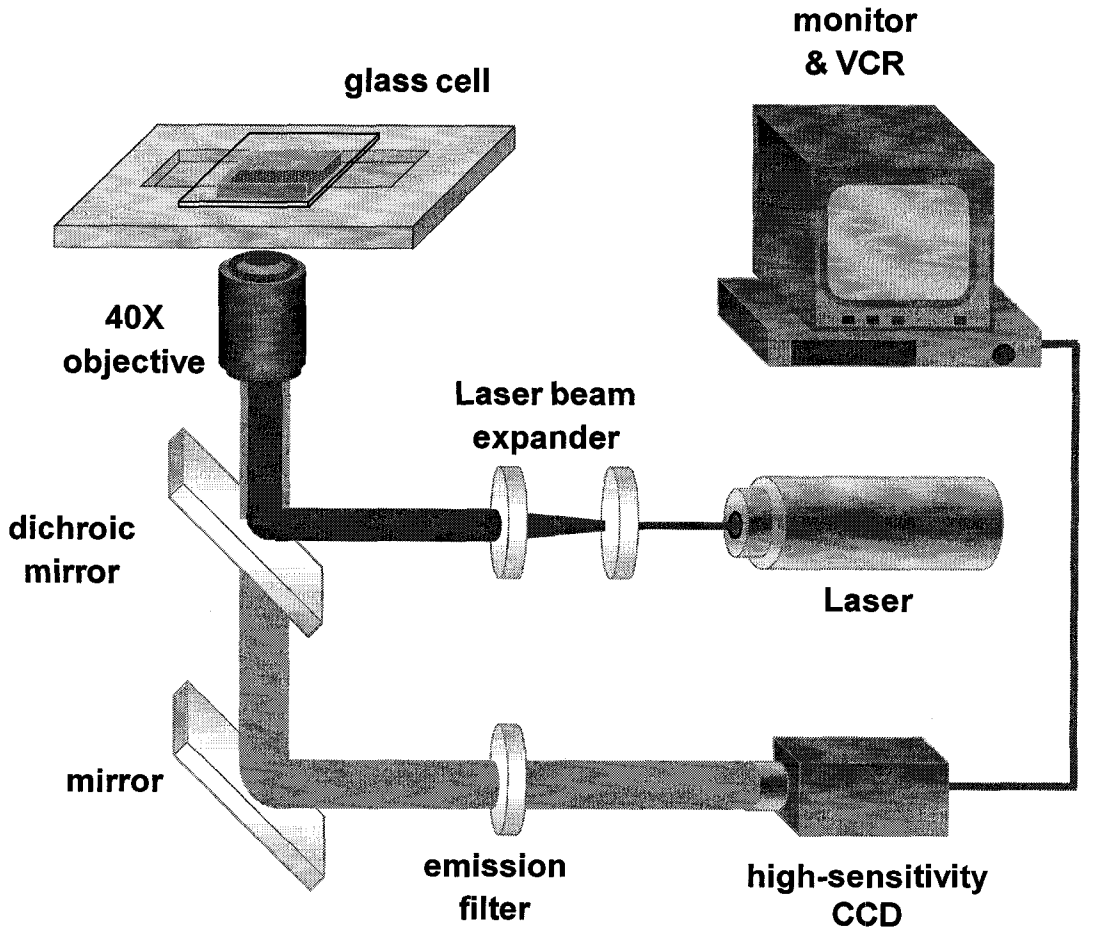

Figure 5-3. Schematic diagram of the setup for electrophoresis and epifluorescence videomicroscopy detection. Gel was fit in a glass cell filled with 0.5× TBE buffer and protected with a cover plate to reduce water evaporation. Electric fields were applied across the gel via two platinum electrodes immersed into the buffer at both ends of the electrophoresis cell.

high-quality colloidal crystal films [17]. Therefore, we performed colloidal growth at ambient conditions and found fairly good crystalline quality could be obtained by choosing appropriate solvent and colloidal volume fraction. In our experiments, an aqueous suspension was found to yield better film uniformity and reproducibility, compared to ethanol or the water/ethanol mixtures that have been reported for depositing large colloidal particles [18, 20]. In addition, the deposition process using water was reliable at low concentration, for instance 0.15% used in this case, at which an ethanol/water suspension of colloids only produced incontinuous thin films and irregular colloidal stripes.

We grew multilayer colloidal bands of 2–3 mm in width as the colloidal templates. Under the conditions used here, 3–5 layers of well ordered colloids were deposited, as shown in Figure 5-4. The periodic arrays of particles illuminated with white light exhibit iridescent colours due to Bragg scattering, which is dependent on the lattice dimensions, structures, and orientations. Therefore, even at low magnification, such scattering allows us to visually distinguish domains of different orientation or structure and the lattice defects in the film, such as major cracks. Figure 5-4A shows an optical microphotograph of a three-layer colloidal sample. Each layer of the sample presents a uniform color pattern, implying a large-area single crystal domain of well-ordered microspheres. A typical SEM image shown in Figure 5-4B further confirms the long range ordering of monodispersed colloidal microspheres, hexagonally close packed in a single domain. Lattice defects are also seen in Figure 5-4, including point voids, dislocation lines, and vertical cracks. The defect density was estimated to be less than 10%, and the domain size was generally 50–100 μm.

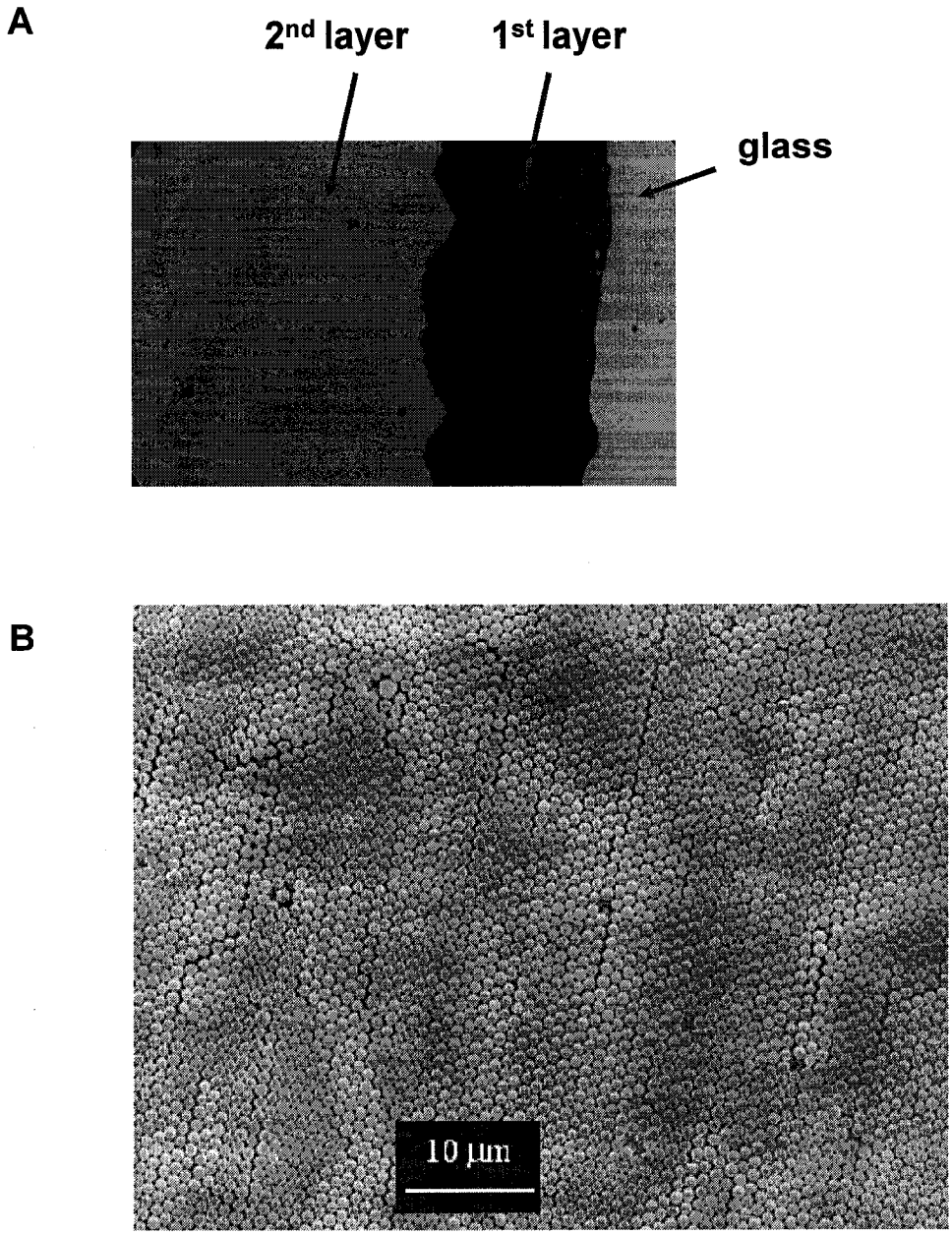

Figure 5-4. Characterization of self-assembled colloidal crystals deposited from monodispersed PS microspheres of 1 μm in diameter. (A) Optical microscope image at low magnification (10× objective). (B) SEM image of a sample coated with thin gold film.

5.3.2 Conformational Dynamics of Single DNA Electrophoresis

We performed here molecular electrophoresis in colloid-templated gel matrices, as schematically illustrated in Figure 5-5. The size of cavities in this material is comparable to that of λ-DNA molecules in buffer, but the connecting pores are much smaller [15, 21]. Molecules must deform to pass through constrictive pores, losing their configurational freedom locally. Thus, molecules tend to stay in open cavities, where the configurational entropy is maximum and the pores serve as size dependent entropic barriers [3, 15].

In the absence of electric field, although coiling into a single cavity still occurs, λ-DNA chains predominantly occupied 2–3 adjacent cavities when undergoing Brownian diffusion in the cavity array [15]. We find that the application of an electric field to these templated gels compresses individual λ-DNA molecules to a single cavity between consecutive jumps. At low electric fields, as shown in Figure 5-6 at E = 10 V/cm, most λ-DNA molecules jump sluggishly from one cavity to another one with elongation

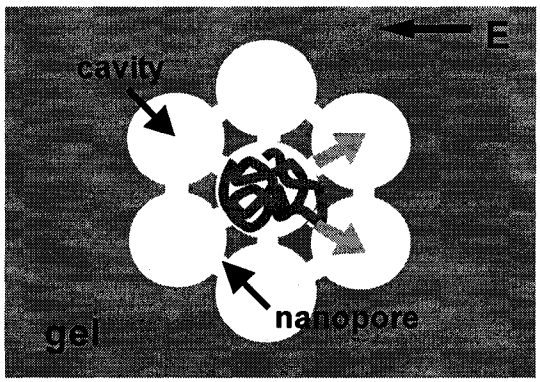

Figure 5-5. Schematic illustration of a linear DNA chain confined in a molecular-sized cavity array.

through two (t = 0.13 and 2.20 s) or three cavities (t = 6.20 and 6.53 s), similar to the confined diffusion observed by Nykypanchuk et al. [15]. Thus, at these fields the entropic effect is dominant, maintaining a relaxed conformation, in contrast to the full elongation seen in reptation mode in gel electrophoresis, which corresponds to ~22 μm in length or about 20 cavities for this system.

Under intermediate field, λ-DNA molecules hop discretely, but faster. The chain is readily stretched by the electric force, so that hooking at pores occurs frequently, as

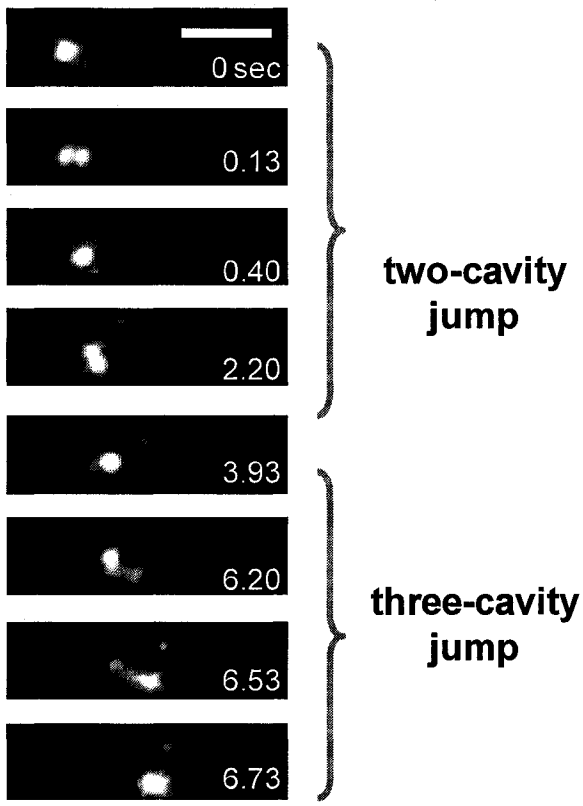

Figure 5-6. Time sequences of fluorescence images of confined λ-DNA molecules (48.5 kbp) electromigrating under an electric field of 10 V/cm. Frames are time-stamped in seconds. The scale bar represents 5 μm.

illustrated in Figure 5-7 at E = 25 V/cm. At t = 1.16 s, a DNA chain is in a two-cavity configuration. Both end segments of the molecule are seen probing different paths, forming a hook at t = 1.70 s. The molecule then slips off the hook following one end. Hooking is typical in gels [22], magnetic array [11], and even in an ordered colloidal array [13], and is expected to become more significant as the electric field increases.

The persistence length of double-stranded DNA is ~50 nm, much smaller than the size of interconnecting pores. Hence hernias, where internal segments of the chain protrude to lead the motion, would be expected to form readily in these templated pores under high electric field. Surprisingly, in our material the opposite trend was observed at relatively high electric fields (50 V/cm in this case). The characteristic behavior, illustrated in Figure 5-8, is for λ-DNA chains to stretch and slip across a fluctuating

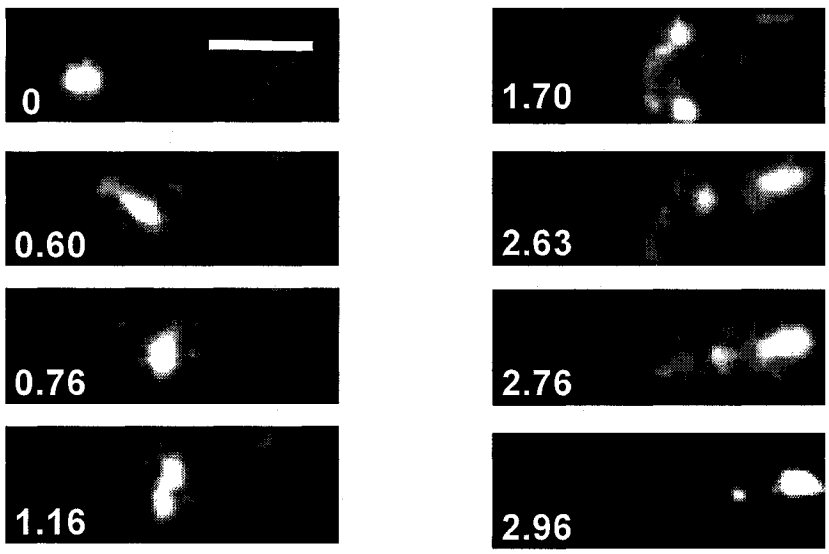

Figure 5-7. Time sequences of fluorescence images of confined λ-DNA molecules (48.5 kbp) electromigrating at E = 25 V/cm. Frames are time-stamped in seconds. The scale bar represents 5 μm.

number of cavities quickly (frames 0 to 0.43 s) and then become trapped in a single cavity for a brief period (frames 0.43 to 3.50 s) without ever reaching full elongation, in contrast to conventional gel electrophoresis. We also see that when the leading head of a molecule is briefly trapped, the tailing part recoils very fast at high electric field, with a reduced tendency to form hooks or hernias. Thus, full reptation rarely occurs at high field in these templated gels, apparently due to confinement in the cavities. This is desirable for DNA size fractionation, because of the size-independent mobility in the reptation mode.

It was observed that the lattice defects in the colloidal template, such as point voids and cracks seen in Figure 5-4, generated disconnected cavities in the replicated

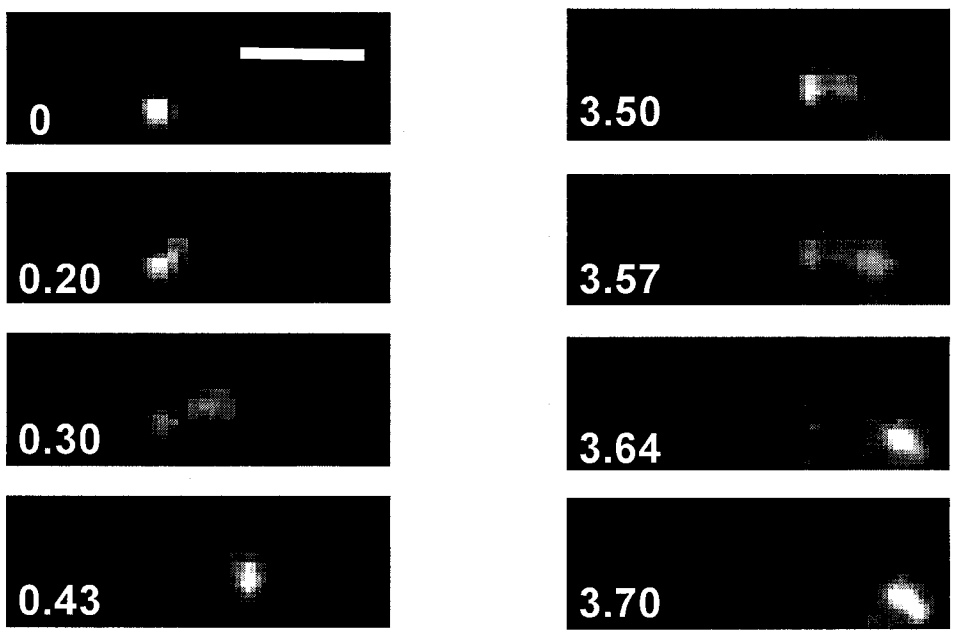

Figure 5-8. Time sequences of fluorescence images of confined λ-DNA molecules (48.5 kbp) electromigrating at E = 50 V/cm. Frames are time-stamped in seconds. The scale bar represents 5 μm.

array. These defects will either block DNA molecules or deflect them from the regular migrating tracks in defect-free regions. The vertical deposition inherently suffers from cracks formed during drying. Template-directed colloidal assembly may offer a promising alternative for tighter control of defect density [23, 24], yielding a practical media for biomolecular separation.

5.3.3 Electrophoretic Mobility Studies

A mobility study was performed to complement the observation of single molecular electromigration. Average mobilities were determined by sampling many individual molecules ($n > 30$) at various constant electric fields. Because the defects in the cavity lattice might affect the motion of DNA molecules, any molecule that approached defects was not analyzed. Only those that migrated more than 20 μm distance along the direction of electric fields were selected to calculate the electrophoretic mobility of each molecule. Long DNA chains exhibit unexpected electrophoretic dynamics within the cavity array, as illustrated by the dependence of mobility on molecular size and electric field shown in Figure 5-9. A maximum in mobility occurs as the field increases, with the peak position dependent on molecular size. Larger λ-DNA molecules of 48.5 kbp move more slowly than smaller calf thymus DNA (13 kbp) at low field strength, but faster at high field. In contrast, the mobility of large DNA strands exhibits an increasing response to field strength up to a plateau value in other separation matrices [3, 13]. Han et al. initially reported size-dependent mobility for long DNA molecules migrating in an entropic array, which was subsequently exploited for separation of DNA, once certain fabrication challenges were overcome [3, 4]. The

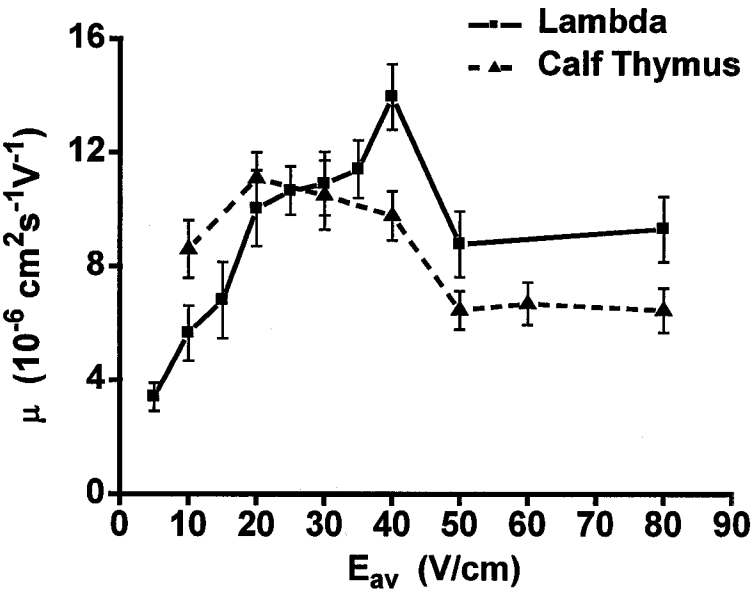

Figure 5-9. Average mobility as a function of electric field for λ-DNA (48.5 kbp) and calf thymus DNA (13 kbp). Error bars show 95% confidence intervals.

mobility differences we observe in Figure 5-9 are favourably comparable with those in ref 3, relative to the confidence limits we observe, so we can comfortably predict good separations will be obtained if the defects in the beds can be reduced.

5.3.4 Geometric Model

In order to understand the non-monotonic mobility dependence on field, we propose a simple model, shown in Figure 5-10, based on the geometry of the confinement and our observations of molecular migration. The radius of gyration of a Gaussian polymer chain is given by

$$R_g = (lL/6)^{1/2} \qquad (5.1)$$

where l is the Kuhn length and L the contour length [1]. R_g of calf thymus DNA and λ–DNA molecules are estimated to be ~0.63 and ~0.34 μm, respectively, while the cavity radius is ~0.5 μm. Under an electric field, the DNA undergoes limited compression, and appears to be accommodated within a single cavity, consistent with Reccius et al's study of DNA compression in nano-channels [25]. Our microscope does not have ideal resolution, but the size of the two types of DNA under an electric field was consistent with the estimated values of R_g, within ~30 %. In all experiments, the electric field was not aligned with any crystal axis that passed straight through a line of nanopores by certain angle, as shown in Figure 5-10A. This is consistent with the zigzag trajectory observed for molecules moving under the electric field. The hydrogel is ion conductive. As a result, the electric field penetrates through the cavity boundary, directing DNA strands against the wall of the pocket region in the cavity located between two inter-cavity pores, as diagrammed in Figure 5-10A and B. Electric field compression is unlikely to squeeze the entire DNA coil into the very small volume of this pocket, because of the semiflexibile nature of the dsDNA chain (persistence length ~50 nm), electrostatic repulsion and the excluded-volume effect [26, 26]. Instead, we hypothesize that the pocket region acts to create a form of "hooking" effect, in which DNA coils facing the nanopores between cavities, and those portions upfield of the pores will transit the pores, limited by entropic trapping factors, while the segments downfield of the pores have to travel uphill to exit the cavity. Such hooking was observed for single λ-DNA molecules electromigrating under the field strength of 50 V/cm. The pocket region thus becomes an extended trapping zone, much like the individual polymer strands that create hooking effects in conventional gels, in which one end of the DNA must move uphill

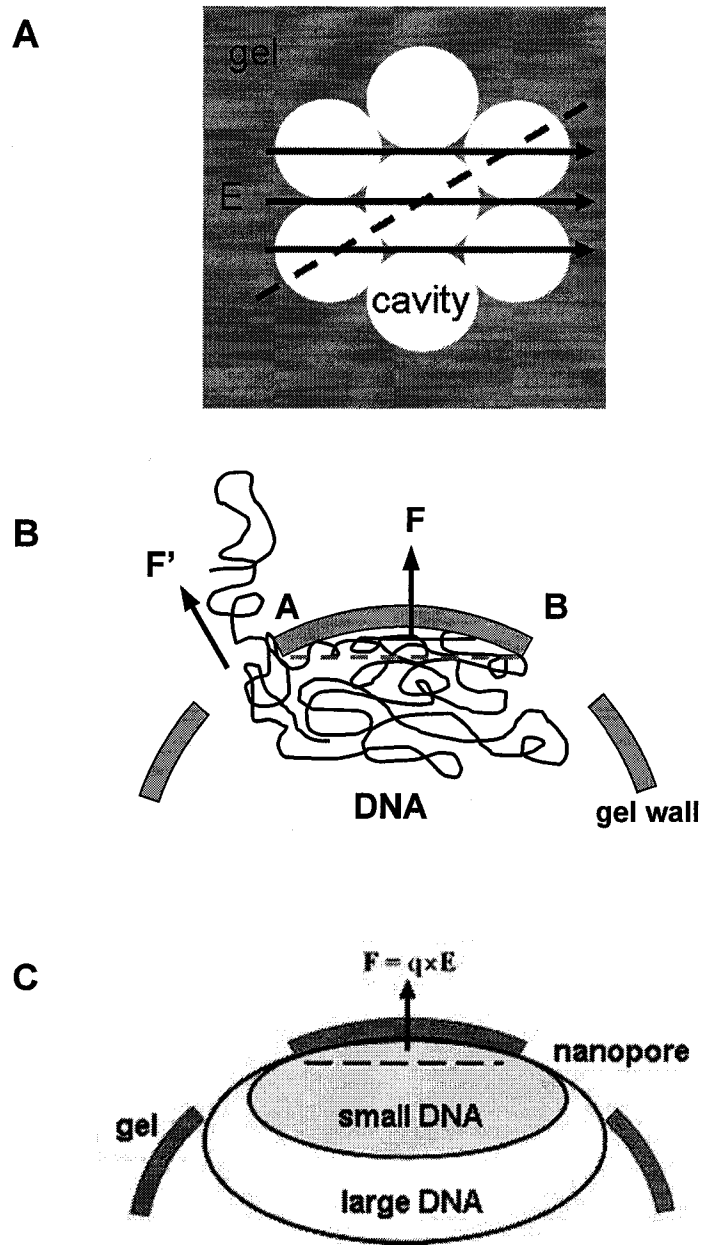

Figure 5-10. Geometric model. (A) Schematic illustration of cavity array with electric field lines penetrating the conductive hydrogel wall. The dashed line indicates a lattice axis. (B, C) Model showing applied electric forces, geometry of cavity and positions of two trapped DNA molecules of different sizes, drawn roughly to scale. The electric force F compresses the molecule against gel wall, while F' tends to pull it out. The dashed lines show the volume from which the portion of trapped molecules escapes against the electric force F through nanopores.

to be released from the trapping site. The smaller the fraction of a molecule localized in the pocket region, i.e. the larger the molecule, the less contribution the trapping effect would make to the overall impediments to motion. These unique characteristics result from the curved geometry of the cavities, and from the conductivity of the cavity array matrix.

Experimentally, under low electric fields, DNA in the cavity array adopts the partially extended structure seen in the absence of an electric field, identified as an entropic trapping effect by Nykypanchuk et al [15]. Smaller molecules move faster than large ones, just as they do in post [8, 11], silica colloids [10], and gel-based separation matrices [19], consistent with a greater ability to diffuse through the nanopores [15]. The higher the field strength is, the more easily the molecular coils can deform and then proceed. Longer chains are known to be delayed by entropic trapping more than smaller ones [15, 27], causing the mobility maximum of longer chains to shift to high field for this mechanism. Our results show that the mobility is reduced at high fields, indicating that the retarding force due to electric trapping begins to dominate. There are two possible factors contributing to the reversed order of the mobility of large and small DNA strands at high electric field. First, larger molecules have a lower proportion of their whole in the electric trapping volume, as illustrated in Figure 5-10C. Therefore, larger molecules experience more net driving force compared to smaller ones. Second, larger molecules have more monomers in proximity to the nanopores, which may increase the escape probability [3, 4].

This qualitative model suggests that the confinement of large DNA in the cavity array is affected by both entropic and electric trapping effects on migration of large

DNA, a unique characteristic which may provide opportunities for novel separation method. In addition to cavity and nanopore sizes, the angle between the lattice axis and the applied electric field is expected to play an important role in altering the electric trapping effect. As the electric field vector and the crystal axes of the pores align, the electric trapping is expected to be reduced due to the shrinking trapping volume. Therefore, in the experiments, although the applied field was not uniformly aligned with the cavities as illustrated in Figure 5-10, the electric trapping effect was present. Future numerical simulation of this model should provide more insight into the effect of the orientation of the electric field on the ability to optimize the separation selectivity.

5.4 CONCLUSIONS

To conclude, we have demonstrated modification of the molecular behavior of DNA by integrating an entropic effect with electric trapping in a synthetic nanopore network. This approach may lead to new mechanisms for manipulation and size fractionation of large biomolecules. It may provide insights for design and optimization of on-chip molecular sieving structure for rapid separation of long DNA molecules as well. Referring to the widely accessible size of colloidal particles, it should be feasible to scale this concept to ten-nanometer regime, which is required for probing protein molecular dynamics in porous media.

5.5 REFERENCES

1. Viovy, J.-L. *Rev. Mod. Phys.* **2000**, *72*, 813–872.

2. Volkmuth, W. D.; Austin, R. H. *Nature* **1992**, *358*, 600–602.

3. Han, J.; Turner, S. W.; Craighead, H. C. *Phys. Rev. Lett.* **1999**, *83*, 1688–1691.

4. Han, J.; Craighead, H. C. *Science* **2000**, *288*, 1026–1029.

5. Cabodi, M.; Turner, S. W. P.; Craighead, H. G. *Anal. Chem.* **2002**, *74*, 5169–5174.

6. Chou, C. F.; Bakajin, O.; Turner, S. W. P.; Duke, T. A. J.; Chan, S. S.; Cox, E. C.; Craighead, H. G.; Austin, R. H. *Proc. Natl. Acad. Sci. U.S.A.* **1999**, *96*, 13762–13765.

7. Huang, L. R.; Cox, E. C.; Austin, R. H.; Sturm, J. C. *Science* **2004**, *304*, 987–990.

8. Kaji, N.; Tezuka, Y.; Takamura, Y.; Ueda, M.; Nishimoto, T.; Nakanishi, H.; Horiike, Y.; Baba, Y. *Anal. Chem.* **2004**, *76*, 15–22.

9. Huang, L. R.; Tegenfeldt, J. O.; Kraeft, J. J.; Sturm, J. C.; Austin, R. H.; Cox, E. C. *Nat. Biotechnol.* **2002**, *20*, 1048–1051.

10. Meistermann, L.; Tinland, B. *Phys. Rev. E* **2000**, *62*, 4014–4017.

11. Doyle, P. S.; Bibette, J.; Bancaud, A.; Viovy, J.-L. *Science* **2002**, *295*, 2237.

12. Minc, N.; Futterer, C.; Dorfman, K. D.; Bancaud, A.; et al. *Anal. Chem.* **2004**, *76*, 3770–3776.

13. Zhang, H.; Wirth, J.M. *Anal. Chem.* **2005**, *77*, 1237–1242.

14. Liu, L., Li, P. S., Asher, S. A., *Nature* **1999**, *397*, 141–144.

15. Nykypanchuk, D.; Strey, H. H.; Hoagland, D. A. *Science* **2002**, *297*, 987–990.

16. Jiang, P.; Bertone, J. F.; Hwang, K. S.; Colvin, V. L. *Chem. Mater.* **1999**, *11*, 2132–2140.

17. Wong, S.; Kitaev, V.; Ozin, Geoffrey A. *J. Am. Chem. Soc.* **2003**, *125*, 15589–15598.

18. Kuai, S.-L.; Hu, X.-F.; Hache', A.; Truong, V.-V. *J. Cryst. Growth* **2004**, *267*, 317–324.

19. McLachlan, M. A.; Johnson, N. P.; De La Rue, R. M.; McComb, D. W. *J. Mater. Chem.* **2004**, *14*, 144–150.

20. Vlasov, Y. A.; Bo, X.; Sturm, J. C.; Norris, D. J. *Nature* **2001**, *414*, 289–293.

21. Smith, D. E.; Perkins, T. T.; Chu, S. *Macromolecules* **1996**, *29*, 1372–1373.

22. Gurrieri, S.; Smith, S. B.; Wells, K. S.; Johnson, I. D.; Bustamante, C. *Nucleic Acids Res.* **1996**, *24*, 4759–4767.

23. van Blaaderen, A., Ruel, R., Wiltzius, P., *Nature* **1997**, *385*, 321–324.

24. Jin, C.; McLachlan, M. A.; McComb, D. W.; De La Rue, R. M.; et al., *Nano Lett.* **2005**, *5*, 2646–2650.

25. Reccius, C. H.; Mannion, J. T.; Cross, J. D.; Craighead, H. C. *Phys. Rev. Lett.* **2005**, *95*, 268101.

26. Cacciuto, A.; Luijten, E. *Nano Lett.* **2006**, *6*, 901–905.

27. Rousseau, J.; Drouin, G.; Slater G. W. *Phys. Rev. Lett.* **1997**, *79*, 1945–1948.

Chapter 6

Conclusions and Future Work

6.1 SUMMARY OF THE THESIS

Self assembly, a process of spontaneous organization of microscopic building blocks into macroscopic functional ensembles, has been well recognized in nature and inspires people to explore efficient approaches to the fabrication of artificial devices with complex nano-features. Motivated by the desire to seek a simple and inexpensive alternative to conventional nanofabrication techniques for making artificial molecular sieves, this doctoral dissertation has concentrated on exploring new colloidal self-assembly methodologies to fabricate crystalline nanoarray-based microsystems, and on their applications to biomolecular analysis.

The practical applications of self-assembly approaches lie in the ability to harness self-assembling to meet various demands. Conventional colloidal self-assembly approaches lack control of crack formation and are difficult to adapt to microfluidic systems. We have demonstrated that a microfluidic self-assembly technique established in this work allows control of the drying process during colloidal growth within prefabricated microdevices, thus preventing the formation of macroscopic lattice cracks. In addition, these techniques feature simple and fast manufacturing, low consumption of colloidal solution, and good compatibility with microfabrication and microfluidic operation.

Using the new techniques developed, we have realized two types of crystalline nanoarray-based microsystems: a single-channel device for one-dimensional constant-field separation and a two-dimensional complex device for continuous DNA fractionation using asymmetric pulsed fields. Fast and reproducible separation of a wide scope of biomolecules, ranging from small protein molecules to long DNA strands, has been achieved using crystalline nanoarrays of variously sized colloids. Separation performance was found to be comparable to lithographically fabricated sieves and microsystems using gel/polymer matrices. The results presented here demonstrate a major advantage of this self-assembly methodology in terms of the flexibility to precisely vary pore sizes to adjust the separation performance for a given type of biomolecules, particularly on a scale of 10 nm. Studies on the separation processes involved and the effects of a number of experimental conditions yield guidelines for achieving the optimum separation of targets with colloidal nanosieves. To our knowledge, this was the first demonstration of biomolecular separation microsystems based on the use of self-assembled ordered colloidal arrays to define the nanofluidic sieve structures.

Finally, we studied the electrophoresis of single long DNA molecules confined in a well-ordered micro-cavity array fabricated by a colloidal templating technique. We identified an unusual size-dependency of DNA mobility, which was proposed to result from the interplay between entropic and electric effects on DNA transport within ordered cavity arrays. This finding has implications for the application of this novel structure to size separation of long DNA molecules; and the role of geometric effects of crystal lattice in relation to the applied field.

6.2 FUTURE WORK

In this section, we will briefly discuss a few thoughts gained during the course of my doctoral studies, regarding future perspectives of this work. In Chapters 2 to 4, self-patterned colloidal beds were used as prepared, as their stability was satisfactory for the proof-of-concept studies. It was found that the electric field strength that the colloidal beds can withstand was below 200 V/cm. Enhancing the mechanical strength of self-assembled colloidal beds will allow the use of higher electric fields, which can increase the analysis speed in the one-dimensional separation systems presented in Chapter 3, and enhance DNA stretching to improve size resolution for pulsed field fractionation (Chapter 4). Therefore, approaches to further strengthen the beds after packing will be the next technical consideration to improve the established procedures.

In Chapter 4, starting from a crude model of DNA motion, we qualitatively explained the observed behaviour of angular DNA deflection via discretely discussing various aspects of DNA conformational dynamics, involving chain stretching, hydrodynamic relaxation and fluctuation, and the formation of hooking and hernias, etc. To accurately capture the deflection behaviour of DNA chains subjected to confinement within close-packed colloidal arrays and various pulsed fields, it is necessary to establish a more comprehensive model with those important factors included, or alternatively, to perform numerical simulations of DNA migration. Specifically designed experiments are needed to provide necessary technical details for creating a model or performing simulations. For instance, we suggest using a high-speed camera to observe DNA electrophoresis under pulsed fields of a variety of frequencies and strengths. This experiment will offer accurate information of the conformational dynamics of migrating

DNA chains to facilitate our modelling and simulations.

We expect that the orientation of the colloidal lattice relative to the direction of electric field should play a role in the separation process using obtuse-angle alternating fields (Chapter 4) or ordered cavity arrays (Chapter 5). The approaches presented in this work were focused on solving the issue associated with crack formation, and unfortunately, do not possess the ability to deliberately manipulate the lattice of colloidal crystals. Therefore, it is difficult to design experiments, based on current self-assembly procedures, to study the effects of the lattice orientation on the separation performance. More sophisticated techniques need to be developed for this purpose. Using prepatterned substrates as the template for colloidal deposition might provide an opportunity, since it has been demonstrated that this methodology offers the capability to direct the crystallization of colloidal crystals. Such an approach might permit tailoring of the lattice structure, orientation and quality of the deposited crystals [1, 2].

We have demonstrated that, by scaling down the pore size, the separation resolution in colloidal sieves can be greatly improved to separate smaller biomolecules. Therefore, it is of interest to test if colloidal sieves can be used for DNA sequencing. In addition to bioseparations, self-assembled colloidal crystals should find a wide range of applications to bioanalysis. For instance, the network defined within a colloidal lattice can be seen as an array of nanochannels, and thus it could be used for the sample preconcentration, based on a mechanism involving electrophoresis of the second kind that has been demonstrated using a lithographically fabricated nanochannel array [3]. The porous structure of colloidal matrices also provide an ideal support, with extremely high size-to-area ratio, for proteomic applications, such as protein digestion, affinity

purification and enrichment, and protein microarrays [4].

To summarize, this thesis represents an initial effort of utilizing colloidal self assembly to develop functional nanostructures for integrated bioanalytical microsystems. The advantages of colloidal self assembly demonstrated in this work convince us that this methodology will attract more interest from both academia communities and industries. Compared to nanolithography, the population of pattern geometries possible through colloidal self assembly remains limited; but significant expansion has been witnessed since it was introduced as a nanomachining tool [5]. The rapidly increasing diversity of colloidal structures makes it possible to find more applications in the fields of lab-on-a-chip and nanotechnology.

6.3 REFERENCES

1 Jin, C. J.; McLachlan, M. A.; McComb, D. W.; De La Rue, R. M.; Johnson, N. P. *Nano Lett* **2005**, *5*, 2646-2650.

2 van Blaaderen, A.; Ruel, R.; Wiltzius, P. *Nature* **1997**, *385*, 321-324.

3 Wang, Y. C.; Stevens, A. L.; Han, J. *Anal. Chem.* **2005**, *77*, 4293-4299.

4 Zheng, S.; Zhang, H.; Ross, E.; Le, T. V.; Wirth, M. J. *Anal. Chem.* **2007**, *79*, 3867-3872.

5 Yang, S. M.; Jang, S. G.; Choi, D. G.; Kim, S.; Yu, H. K. *Small* **2006**, *2*, 458-475.

Appendix

Calculation of DNA deflection angle θ

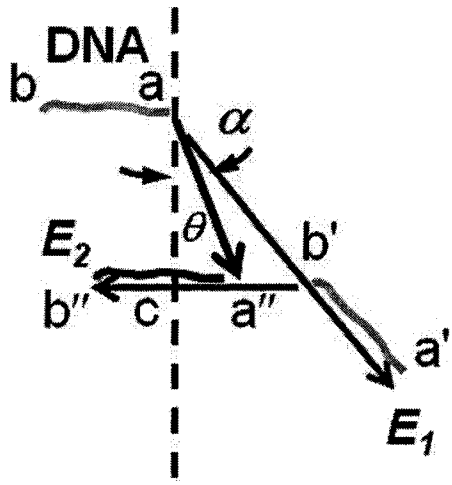

Figure A-1. Trigonometric calculation of DNA deflection angle θ based on DNA motion depicted in Figure 4-8. The molecular length of a DNA chain is assumed to be constant during reorientation and migration under the alternating fields E_1 and E_2.

In the model presented in Chapter 4, a DNA chain is assumed to maintain a uniform fractional extension l during electromigration, thus the deflection angle θ can be calculated by trigonometry. When the pulsing frequency f is small, the migration distance of a DNA chain along either field vector (in opposite direction) is longer than its own length. As drawn in Figure A-1, the end positions of the DNA chain can be marked as ab at the beginning of Pulse E_1, $a'b'$ at the end of Pulse E_1, and $b''a''$ at the end of Pulse E_2, respectively. Since $aa' = d_1$ and $a'b' = l$, then the length of ab' is

$$ab' = aa' - a'b' = d_1 - l \qquad \text{(A.1)}$$

The length of $a''b'$ is calculated using $b'b'' = d_2$ and $a''b'' = l$ as

$$a''b' = b'b'' - a''b'' = d_2 - l \tag{A.2}$$

Position c is defined as the intersection of the normal to ab with $a''b''$, extended from the head a. Because $cb' = ab'\sin\alpha$, we have

$$ca'' = cb' - a''b' = ab'\sin\alpha - (d_2 - l)$$

$$= (d_1 - l)\sin\alpha - (d_2 - l) \tag{A.3}$$

Then we can calculate the angle of the net motion aa'' (i.e. the deflection angle θ) as

$$\tan\theta = \frac{ca''}{ac} = \frac{(d_1 - l)\sin\alpha - (d_2 - l)}{ab'\cos\alpha}$$

$$= \frac{(d_1 - l)\sin\alpha - (d_2 - l)}{(d_1 - l)\cos\alpha}$$

$$= \tan\alpha - \frac{(d_2 - l)}{(d_1 - l)}\sec\alpha \tag{A.4}$$

Equation A.4 (i.e. Equation 4-1) applies only when $d_2 \geq l$. DNA motion under extreme conditions (i.e. $d_2 < l$) has been discussed in Sec 4.3.4. Because travel distance d_1 and d_2 are inversely proportional to the pulsing frequency ($d_1 = c\mu E_1/2f$ and $d_2 = c\mu E_2/2f$), a curve of DNA deflection angle θ as a function of frequency, drawn in Figure A-2, can be predicted in light of the constant DNA length model (see Sec 4.3.4 for the discussion in details). It clearly suggests the curve of DNA deflection angle θ can be divided into four regimes in response to the increase of pulsing frequency f: 1) low-frequency plateau when $d_1 > d_2 >> l$; 2) arising regime when d_1 and d_2 are approaching l; 3) maximum deflection plateau at high-frequencies ($d_1 > l \geq d_2$); and 4) dynamic trapping regime when $l \geq d_2$.

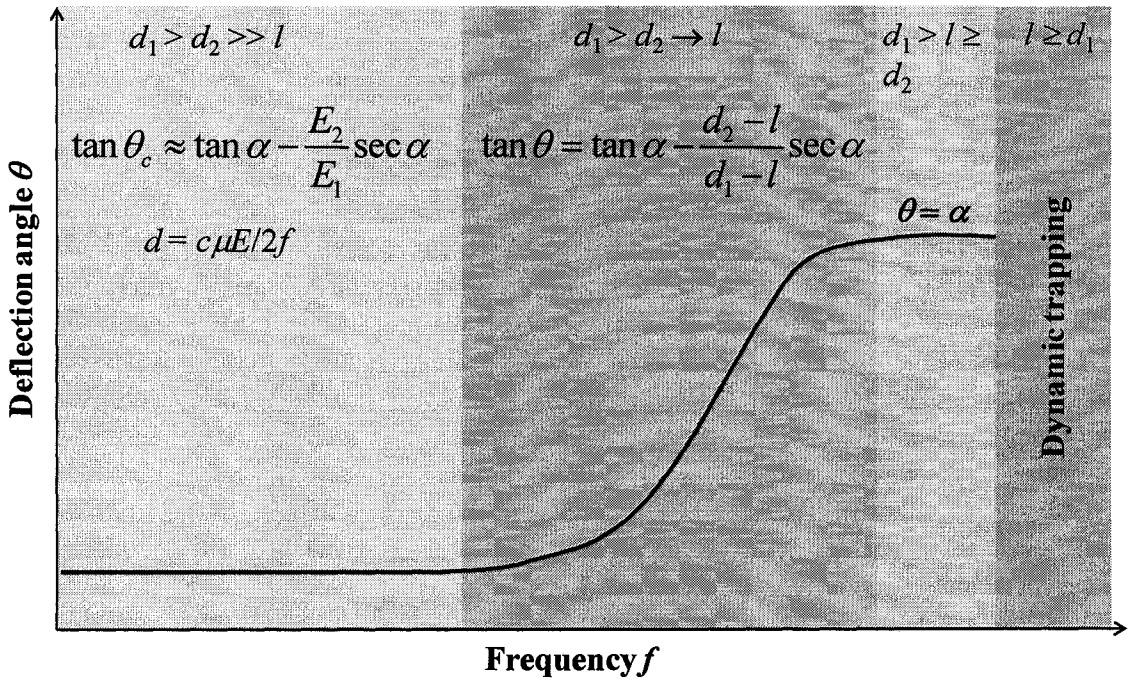

Figure A-2. Plot of DNA deflection angle θ as a function of pulsing frequency predicted from the constant DNA length model (Sec 4.3.4).

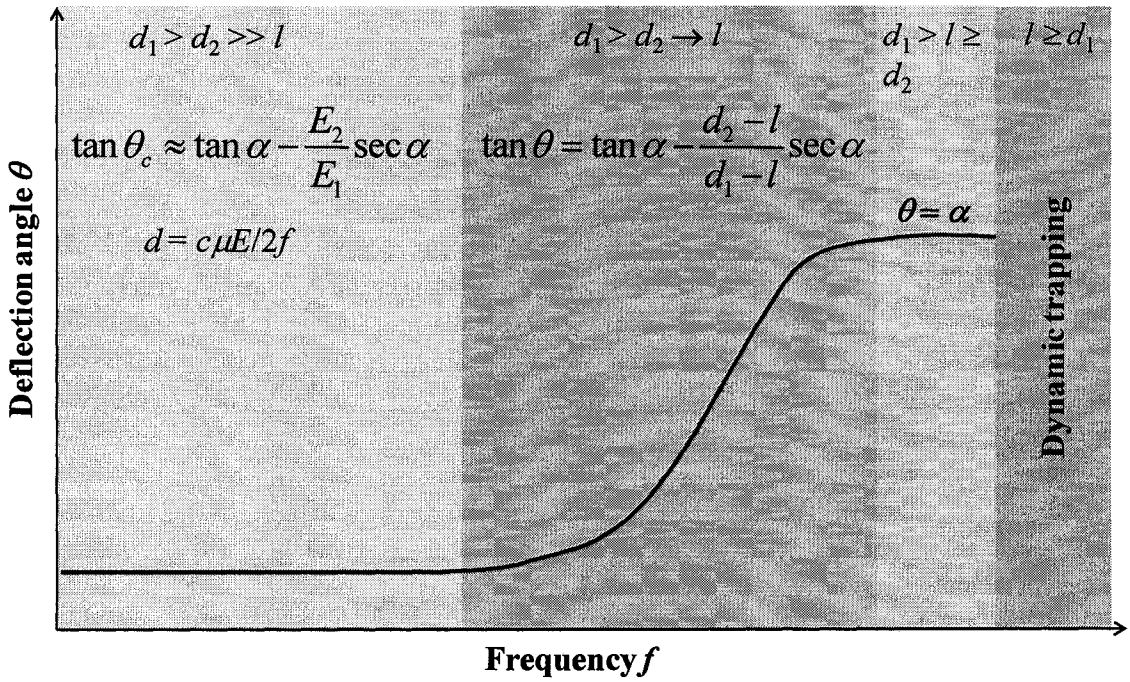

Figure A-2. Plot of DNA deflection angle θ as a function of pulsing frequency predicted from the constant DNA length model (Sec 4.3.4).